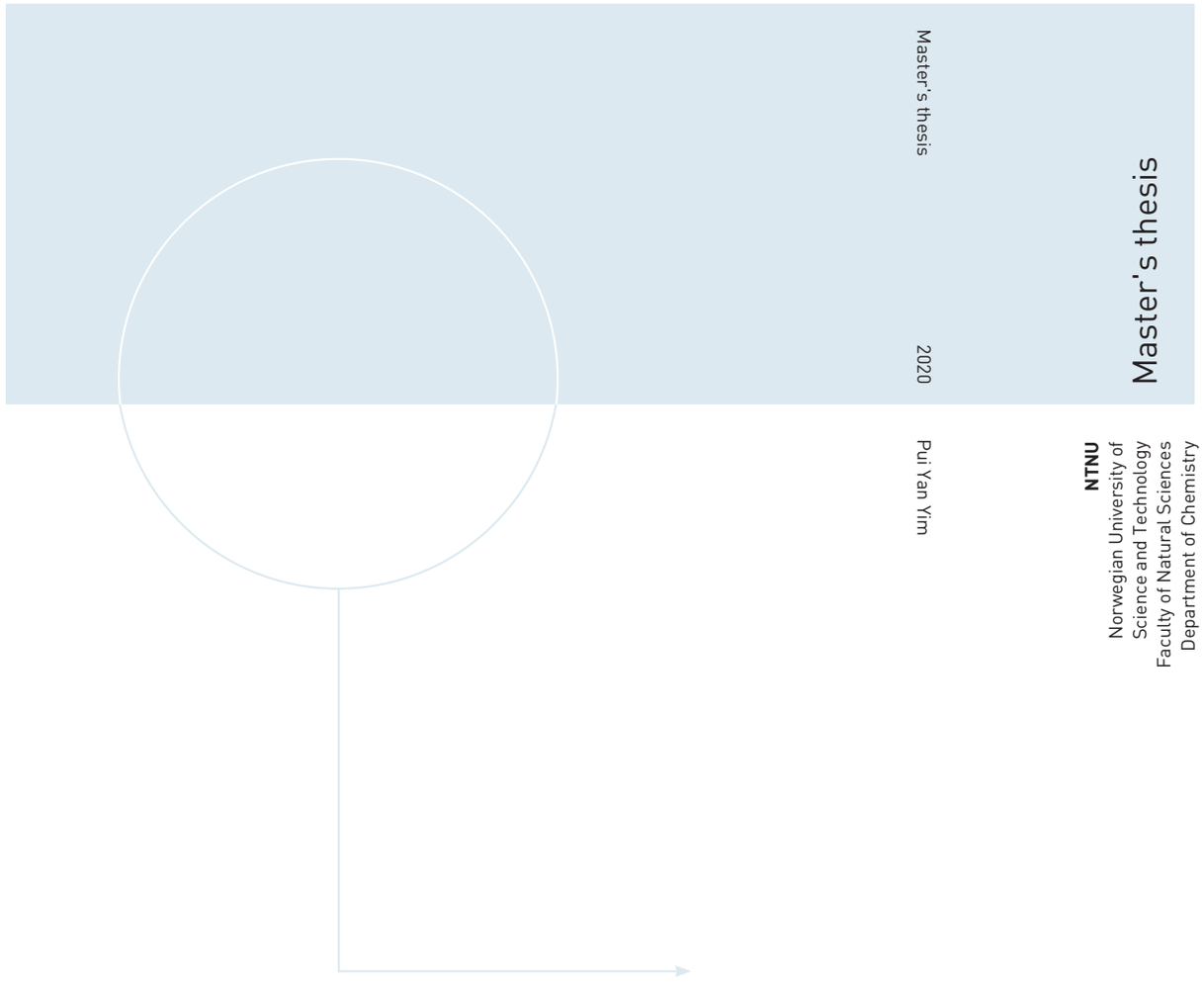

Pui Yan Yim

Introducing Cobalt into Silica Aerogel

May 2020

NTNU
Norwegian University of
Science and Technology

NTNU
Norwegian University of
Science and Technology

NTNU
Norwegian University of
Science and Technology

Introducing Cobalt into Silica Aerogel

Pui Yan Yim

Master's Thesis in MSCHEM
Submission date: May 2020
Supervisor: Karina Mathisen
Co-supervisor: Karsten Granlund Kirste

Norwegian University of Science and Technology
Department of Chemistry

ACKNOWLEDGEMENTS

This master project was performed in the Department of Chemistry at the Norwegian University of Science and Technology (NTNU). I would like to give a huge thank to my supervisor Dr. Karina Mathisen giving me an opportunity to work in the Structural chemistry group. I have learned a lot from this experience as a chemist throughout these two years. This opportunity helps me to discover my passion in research. I am grateful for your support and guidance, not only academically but also socially. You are always nice and care about my well-being. I would also like to thank my co-supervisor PhD candidate Karsten Granlund Kirste for making the time for me when I needed. You are always patient with me and encourage me when I was frustrated about my work. This project could not be completed without both of your generous support and your expertise.

Furthermore, I would like to thank PhD candidates Guro Sørli and Daniel Ali for your assistance in the catalytic testing and ICP-MS. You also make the laboratory a happy place to work in. Thanks also goes to postdoc Muhammad Mohsin Azim for give valuable advice that will be useful for my future career. Thanks are also given to Kristin Høydalsvik Wells and Silje Marie Dale for assistance with XRD, Anuvansh Sharma with BET and Syverin Lierhagen with ICP-MS.

Finally, I also want to thank everyone in the group for making these two years joyful and unforgettable. As an international student who do not speak the native language, I would not be able to survive without all your support and help. Thanks for making my stay in Norway so much fun and giving me useful advice about preparing for the Norwegian winter. I have learned a lot from each of you. This group will be the first thing to remember when I think about Norway in the future. Thank you for being my friends and family in Norway.

ABSTRACT

This thesis is the continuation of a master project done by Sondre Håbrekke.[1] Cobalt was tried to introduce into the matrix of silica aerogel in single site via sol-gel method. Cobalt silica aerogel was prepared by using sodium silicate, following by ambient pressure drying (ADP). Introduction of cobalt was done by adding the cobalt cation into the sol prior to gelation. Surface hydrophobization and solvent exchange were performed simultaneously using the instantaneous solvent exchange/surface modification (ISE/SM) process. Silica aerogel was prepared under different conditions (ie gelation pH and surface modification temperature) and using different parameters (ie. types of precursors, silylation agents and exchange solvents) to investigate the possibility to incorporated cobalt in single site.

Different characterization techniques were performed to study how the introduction of cobalt affects the structure of silica aerogel. X-ray diffraction (XRD) was used to identify unwanted crystalline phases in the gel. Nitrogen adsorption/desorption isotherm was used to estimate the total surface area and pore size, where inductively coupled plasma mass spectrometry (ICP-MS) was used to measure the uptake of cobalt into the gel. X-ray absorption spectroscopy (XAS) analysis was performed to obtain information about the oxidation state and the local environment of the cobalt cation. Extended X-ray absorption fine structure (EXAFS) spectra showed only the first shell that attributed to Co-O scattering pairs at ~2 Å. The absence of the second shell contribution attributed to Co---Co confirmed that the cobalt was successfully introduced into silica aerogel in single site. Amorphous structure, the surface area of the gel and local environment of cobalt species in the gel remain almost the same after annealing, indicating the material is thermally stable up to 450°C.

ABBREVIATION

Absorption Energy	E_0
Amplitude Reduction Factor	AFAC
Ambient Pressure Drying method	APD
Brunauer, Emmett, Teller	BET
Barrett- Joyner- Halenda	BJH
coordination number	N
Debye- Waller factor	$2\sigma^2$
Diffuse Reflectance Infrared Fourier Transform Spectroscopy	DRIFTS
Distance	R
Ethanol	EtOH
Extended X-ray Absorption Fine Structure	EXAFS
Fermi Energy	E_F
Fischer-Tropsch synthesis	F-T Synthesis
Gas Chromatography–Mass Spectrometry	GC-MS
Gerade	g
Hexamethyldisilazane	HMDZ
Hexamethyldisiloxane	HMDSO
Inductive Coupled Plasma Mass Spectrometry	ICP-MS
Instantaneous solvent exchange/surface modification	ISE/SM
Mass Flow Controller	MFC
Mass- to- charge ratio	m/z ratio
Methanol to hydrocarbon	MTH
Nitrogen Oxide	NO_x
Point of Zero Charge	PZC
Room Temperature	r.t
Round Bottom Flask	RBF
Selective Catalytic Reduction with Hydrocarbons	HC-SCR
Single Site Heterogenous Catalysts	SSHC
Tetraethoxysilane	TEOS
Trimethylsilyl chloride	TCMS

Tetramethyl orthosilicate	TMOS
X-ray Absorption Near Edge Structure	XANES
X-ray Absorption Spectroscopy	XAS
X-ray Diffraction	XRD
Weight Percentage	wt %
Ugerade	u

CONTENTS

1 INTRODUCTION

1.1 Background

Due to the rapid population and economic growth, the demand for oil and other energy sources has been increasing significantly. According to the prediction by Hubbert, the crude oil and natural gas liquid (NGL) production will reach its peak and deplete within the next 10 years.[2] Therefore, some research groups have developed alternative technologies to produce fuel from other sources and cobalt is found to be an active catalyst component to improve the efficiency of fuel production. Cobalt based catalysts are used in Fischer-Tropsch (F-T) synthesis for converting coal and natural gas to ultraclean hydrocarbon fuels that contain no sulphur or nitrogen and aromatics. Cobalt and its compounds also used to selectively oxidise methane to synthesis gas provide a broad prospect for production of petrochemical products for alternative energy.[3-6] Although cobalt has remarkable future potentials in processes of environmental catalysis due to its selectivity and activity, it is expensive and less abundant that other transition metal, ie iron and nickel.

In order to reduce the cost of catalysts, porous supports have attracted steady attention of researchers. The structure of these supports has greatly influenced the reducibility, the cobalt dispersion, the activity and selectivity of catalysts. For example, cobalt supported catalysts have higher activity for CO conversion, and they are CO_2 tolerant. It is believed that the interactions between support and the metal have stabilized the cobalt phase against particle sintering and so increase the stability of the catalyst. [3, 7, 8]

Mesoporous silica aerogel has been studied extensively as a candidate of support material in catalysis due to its high surface area, open porous structure and thermal stability.[9] Silica aerogel with large surface area is an ideal support for single site heterogeneous catalyst (SSHC).[10] In heterogenous catalysis, dispersion of catalytically active metals affects the efficiency of a catalyst. Highly dispersed active phases in SSHC can increase the number of active site for catalysis and so increase catalytic activity of the catalyst.[11]

Thermal induced deactivation is a common challenge in heterogeneous catalysis. The pore structure of the support can collapse at high temperature during catalytic reaction, leading to the loss of surface area. Hydrophobized silica aerogel is thermally stable that can retain its high surface area. It is crucial for maintaining catalytic performance.[12] All these unique properties make silica aerogel a promising material for catalysis.

1.2 Scope of This Work

This project is the continuation of a previous work done by Sondre Håbrekke.[1] The goal of this project is to incorporate cobalt into the matrix of silica aerogels in single site. This single site cobalt silica aerogel is synthesised by a newly developed method using inexpensive silica precursors, sodium silicate, and the ambient pressure drying (ADP).[13] According to previous attempts, incorporation of cobalt in single site was not successful by using hexamethyldisilazane (HMDZ) and hexamethyldisiloxane (HMDSO) as the silylation agents to modify the gel surface.[1] It is because HMDZ produced ammonia and hydroxide ions as by products during surface modification and raised the pH of the sol, leading the formation of cobalt hydroxide and cobalt amine complexes. These complexes were then oxidized to form cobalt oxide (CoOx) during heat treatment. Therefore, in this work, the cobalt silica aerogel is synthesised under acidic condition, using different cobalt precursors and silylation agents in order to prevent shrinkage of pores, expulsion of cobalt out of silica gel matrix and formation of cobalt oxide.

2 THEORY

2.1 Silica Aerogel

Silica aerogel was first invented in 1931 by Kistler. [14] It is an ultralight amorphous material that has more than 95% of its volume made up of air. This material is produced by replacing the liquid components in the pore of the silica gel with gas while largely maintaining its typical structure of the pores and the network. [15, 16] This nanostructured materials with many unique properties, for example high surface area (400-1200 m^2g^{-1}) , low density (~0.003-0.5 gcm^{-3}), high porosity (80-99.8%), low thermal conductivity (0.005-0.1WmK^{-1}), low index of refraction (~1.05) and ultra-low dielectric constant (k=1.0-2.0).[17, 18] Owing to these unique properties, silica aerogels have been widely used in several technological applications, such as being used as thermal insulation materials for window system[19], dielectric materials[20], absorbents for environmental cleanup [21, 22] and supporting materials in catalysis.[17, 23, 24]

Silica aerogel possess mostly mesopores (2-50nm in diameter) with relatively few micropores (< 2nm in diameter) and macropores (>50nm in diameter).[15, 16, 18] Micropores are formed when 2-6nm sized silica particles, referred as primary particles, pack together irregularly and aggregate into larger particle. These larger particles, also known as secondary particles, then interlink together like pearls in a necklace structure and make up the mesopores. [17] Figure 2.1 illustrate the 3D network of silica aerogel.

During the last two decades, significant attention has been given to the synthesis of silica aerogel. More studies have been done on modifying synthesis parameters. [25-30] Structure of the aerogel can be manipulated by the preparation conditions. For example, aerogels with narrow and uniform pores are produced if tetramethyl orthosilicate (TMOS) is used as a silica precursor whereas aerogels with higher degree of monolithcity are produced if waterglass is used.[31] Other parameters, including pH, gelation time, temperature, surface modification agents, exchange solvents and dry processes can also affect the pore networks of aerogel.[32]

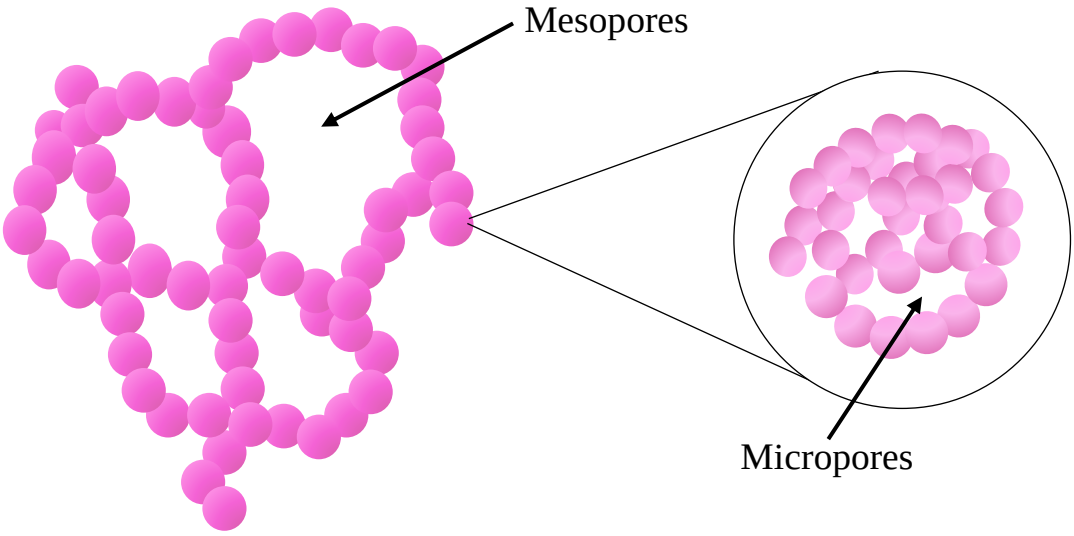

Figure. 2.1. The 3D networks of silica aerogel, consisting primary particles (in the circle) and secondary particles.

2.1.1 Preparation of Silica Aerogel

The production of silica aerogel consists of two processes: Sol-gel chemistry and drying. Sol-gel chemistry is widely used for the preparation of silica aerogel. During the procedure, the colloidal solution (sol) gradually transforms into a solid form (gel). The 3D network of silica gel is formed in three steps: hydrolysis, condensation and polycondensation. Silicon alkoxides are the most common precursors for preparing silica aerogel gels because it prevents the formation of salt by-products and allow better control of the final product..[17] The solid silica network is formed as the result of hydrolysis and subsequent condensation reactions of silicon alkoxides that initiated by acid or base catalyst, forming siloxane bridge (Si−O−Si).[23] The hydrolysis and condensation reactions of TEOS is show in Figure 2.2.

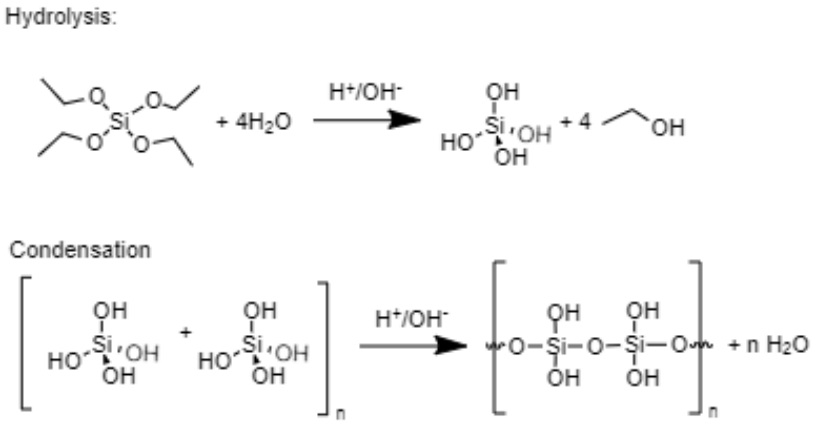

Figure. 2.2. Hydrolysis and condensation reaction of TEOS catalysed by acid or base

However, silicon alkoxide precursors like tetraethoxysilane (TEOS) are expensive and hazardous materials which are not favorable for large scale commercialization. Therefore, sodium silicate is used as an alternative. Sodium silicate, also known as waterglass, is a polar compound that dissolves in water. The electrostatic effects between ions prevent spontaneous gelation by forming larger silica polycondensates, therefore, sodium silicate is easy to handle.[33] Besides, it is a less expensive industrial silica source due to its wide abundance and has no flammability hazard like silicon alkoxides (TEOS or TMOD) do.[18]

In the case of waterglass, no actual hydrolysis takes place. Instead, a simple acid-base reaction is used to activate molecular silicates precursor. This can be done by addition of acid to silicate solution or ion exchange with a column filled with strong acidic cation resin. Na^+ ions in the solution are replaced by proton H^+ and forming a silicic acid (H_2SiO_3) solution.[32] (Equation 1) The pH of sodium silicates is about 11.5, where the pH of silicic acid formed after ion exchange is about 2.5-3. At pH below 4, waterglass mainly exists in a protonated form silicic acid, H_2SiO_3, and its hydrated form orthosilicic acid, $Si(OH)_4$, by reacting with water (Equation 2) [33, 34]

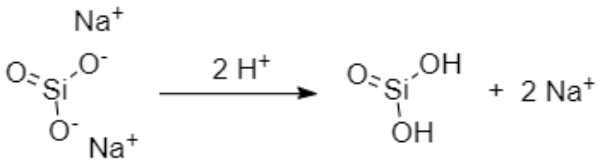

(1)

$$Na_2SiO_3 + H^+ + H_2O \rightarrow Si(OH)_4 + Na^+ \quad (2)$$

When small equivalent of Brønsted base, OH^-, is added to increase the pH value of the silicic acid, the partial neutralization leads to gelation by initiating condensation reaction between silica species, forming −Si−O−Si− bond and water.[33] The condensation reaction is shown in Equation 3.[35] During polymerization, the 3D network molecular structure of silica gel is formed (Figure 2.3).

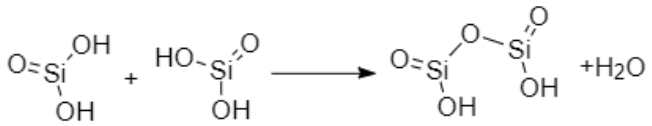

(3)

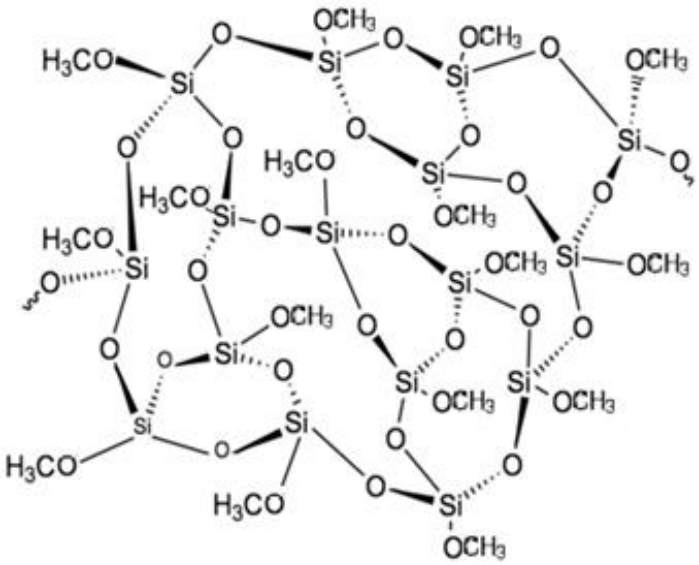

Figure. 2.3. 3D network of silica aerogel with molecular structure

pH of the sol can affect the gelation time, optical transmission, porosity and density of resulting gel. [36] When a base, is added to the sol, it reacts with a fraction of the silanol groups on the silica particle surface and leaves a charged site on the surface. The condensation kinetics depends strongly on the pH as the condensation process is governed by the electrostatic interactions of the charged molecular species and clusters. At high pH (pH>10), sodium silicate is the major species in the sol, condensation rate is slow. Due to electrostatic repulsion force between negative charge of the $Si{-}O^-$ groups that prevent colloidal silica particles coming together, the waterglass solution does not gel. At pH 5-8, surface charge density decreases as the number of $Si{-}O^-$ groups decreases, minimizing repulsion forces between silica particles. It allows particles to agglomerate and form a gel. Rate of condensation reaction is the fastest at moderate pH values. At pH <4, waterglass mainly exists in its protonated form. Silica particles carry a positive surface charge resulting in columbic interparticle repulsion. The strong competing effect of H^+ prevents particles from fusing together and causes more time to form a gel. [33, 36, 37]

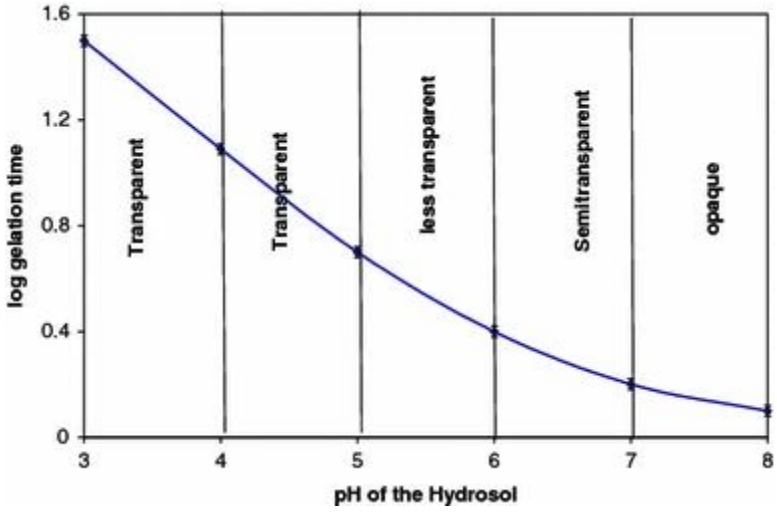

Figure. 2.4 Change in the gelation time (log) with the pH of the sol. Reprinted with permission from Rao et al. [36] Copyright 2008 Springer Nature

The structure of the resulting gel also depends on the pH. At pH 4, probability of the combination of silica particles is low due to the coulombic repulsion, results in gels with small particles and high packing fraction. Since the packing fraction of particles is high, free

movement of exchanging ions is limited in the following silylation and solvent exchanges steps. Poorly surface hydrophobized surface leads to shrinkage of gel during drying and obtain high-density aerogel. The density of aerogel decreases, and the percentage of porosity increases with increasing pH. At higher pH >6, bigger clusters formed due to the reduction of surface charge on particles. These clusters are loosely arranged resulting in a porous network. This structure allows more silylation and leads to less volume shrinkage, low density and more porous aerogel. The drying process will be discussed in detail in Section 2.1.2.[38]

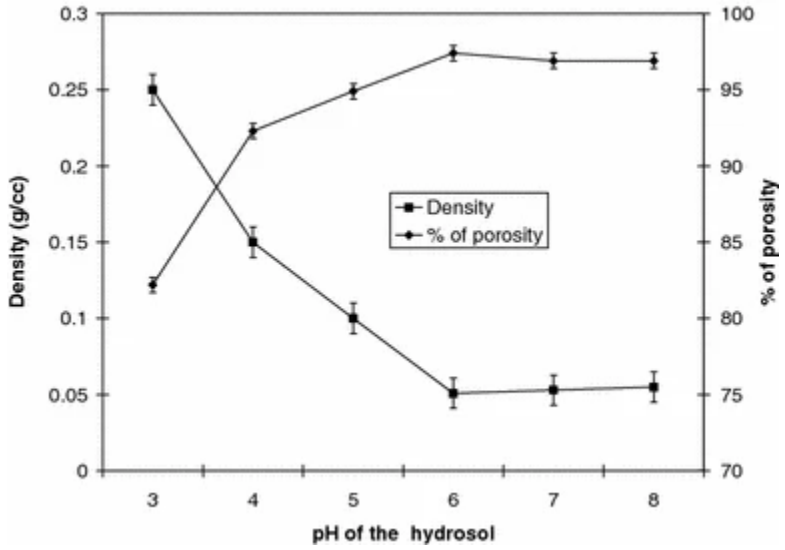

Figure. 2.5 Change in the density and percentage of porosity of the aerogels with the variation of the pH of the sol. Reprinted with permission from Rao et al.[36] Copyright 2008 Springer Nature

A fresh gel formed after gelation is extremely fragile that cannot withstand external pressure without causing structural damage. Therefore, the gel usually maintain in its pore liquid for several hours to strengthen the gel network structure.[39] During this period, structures of the gel continue to change after gel point. This phenomenon is called aging and involves several processes including polymerization, syneresis and coarsening.[40] Polymerization is a process forming Si−O−Si bond by the condensation reaction between silanol (SiOH) groups (Equation 4).

$$\equiv Si–OH + HO–Si\equiv \rightarrow \equiv Si–O–Si\equiv \quad (4)$$

The condensation rate depends on temperature and pH of the solution. By increasing the connectivity of the silica network, the gel structure is strengthened and stiffened. Reversible hydrolysis reaction also happens during aging, which is shown in Equation 5.[26, 40]

$$\equiv Si–OR + H_2O \rightleftharpoons HO– Si\equiv + ROH \quad (5)$$

Syneresis is the shrinkage of pore leading to the expulsion of pore liquid. As condensation reaction proceed, more bridging bonds Si–O–Si are formed.[41] These Si–O–Si bonds take up less space than two Si–OH bonds, leading to spontaneous contraction of pores. (Figure 2.6) More shrinkage of the pores as the result of cross-linking of the gel network with an increase in aging time. Syneresis contraction rate increases with the temperature and concentration of silica in the sol.[42]

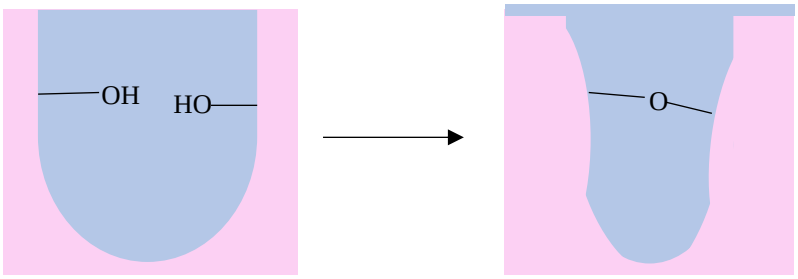

Figure. 2.6. Shrinkage of pore (pink) results from condensation reaction of two silanol groups causing pore water (blue) to expulse from pores

Coarsening or Ostwald ripening is a process of dissolution and reprecipitation of smaller particles which are driven by differences in solubility between surfaces. Small particles are more soluble and precipitate in the region of negative curvature, the crevices and necks, between weakly interlinked silica particles. (Figure 2.7) The growth of necks between particles and small pores will be filled in, resulting in an increase in average pore size and pore volume and a decrease in specific surface area.[41] It also contributes to the strength and stiffness of the network. Factors, such as temperature, pH, concentration and types of solvent, affect the solubility of silica particles influences the coarsening rate. The solubility of particles increases

with pH value of solvents and coarsening is enhanced. Therefore, the strengthened gel network may resist the compression by capillary forces during drying.[26, 40, 42]

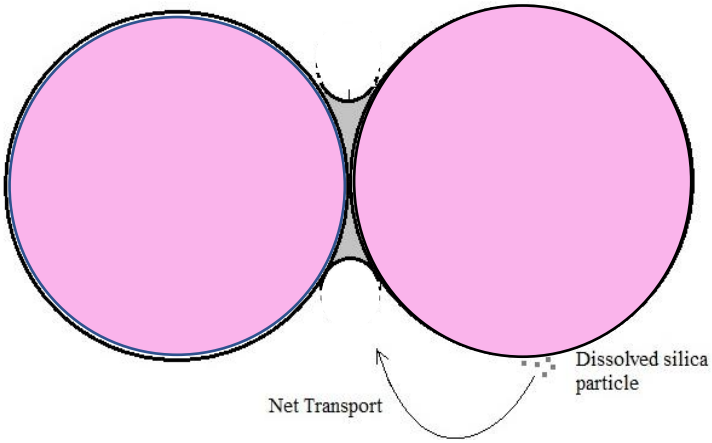

Figure.2.7. Particles tend to dissolve form particle surface with positive curvatures (pink) and precipitates on the neck with negative curvatures (grey). [26]

Continued polymerization and coarsening strengthen the gel network and minimize shrinkage during drying. Thus, volume shrinkage is reduced with an increase in aging time and leads to low-density aerogels. However, a slight increase in gel density is observed for long aging time (> 4hours) due to syneresis, condensation and evaporation of pore fluid.[43]

2.1.2 Ambient Pressure Drying

The drying step is critical in production of silica aerogel. The purpose of this process is to remove the liquid in the gel while retaining the 3D silica network. However, evaporation of pore liquid usually leads to irreversible shrinkage of the gel structure. As liquid in pores begin to evaporate, compressive forces start to build up in pores and eventually the pores contract. [35] The gel shrinks due to the development of capillary force exerted on the silica network, which can be represented by Equation 6.[18]

$$P_c = \frac{-\gamma_{lv}}{(r_p - \delta)} \quad (6)$$

where P_c is the capillary force of the pore solvent

γ_{lv} is surface tension of the pore liquid

r_p is the pore radius

δ is the thickness of the surface adsorbed layer

The shrinkage of gel causes surface silanol groups to come closer to each other and react, resulting in new O-Si-O bonds. Pore structures in gel collapse because of the inherent flexibility of the silica polymer chain.[17] The building up of surface tension can be avoid by using the supercritical drying method, which is first developed by Kistler.[14] Liquid in pores is transformed to 'supercritical' fluid and surface tension ceases because molecules can effuse through pores like a gas.[35, 44] However, supercritical drying method is costly and dangerous because high temperature and pressure conditions are required to approach the critical point of the solvent.

Ambient Pressure Drying method (APD) is an alternative approach for the synthesis of silica aerogel, which is more cost-efficient and less dangerous. Ambient drying is only possible if the internal surface of the silica gel is hydrophobized by silylation agents. This process is called surface modification. Hydrophobization of the inner surface of gel can prevents condensation reactions between adjacent silica cluster on the walls of shrunken pore during drying. It also avoids deterioration of the structure with time due to the absorption of water from humid air and degrade the unique properties of silica aerogels. [33, 35, 45, 46]

APD is a time-consuming process that involves several separated steps of washing, solvent exchange and surface modification. Instantaneous solvent exchange/surface modification (ISE/SM) process was developed by Hwang et al. to combine those multiple steps into a one-step process. In this method, hydrophobization and the replacement of pore water take place simultaneously. [47, 48] Surface modification is done by immersing the wet gel into a solvent containing alcohol, linear saturated hydrocarbon and silylation agent. Hydrophobicity of the

gel surface is achieved by replacing the surface silanol groups with an organosilane group. (Figure 2.8)

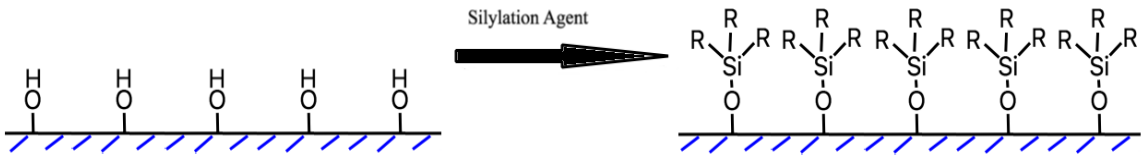

Figure.2.8. Surface modification of the gel surface

After modification, the surface of the gel can be rendered hydrophobic and hence exchange water with organic solvent, such as n-hexane/ n-heptane. (Figure 2.9) Percentage of shrinkage and density of the final gel depends on the nature of exchange solvent used. The evaporation of solvent with low surface tension can reduce capillary force during and so minimize shrinkage. [31, 45] Although the capillary force cannot be avoided and the shrinkage of gel structure still occurs, this shrinkage is reversible. It is due to the organosilane groups on the modified gel surface hinder the formation of siloxane bond (Si–O–Si) during drying.[12] This re-expansion of the dry gel is known as the spring back effect.

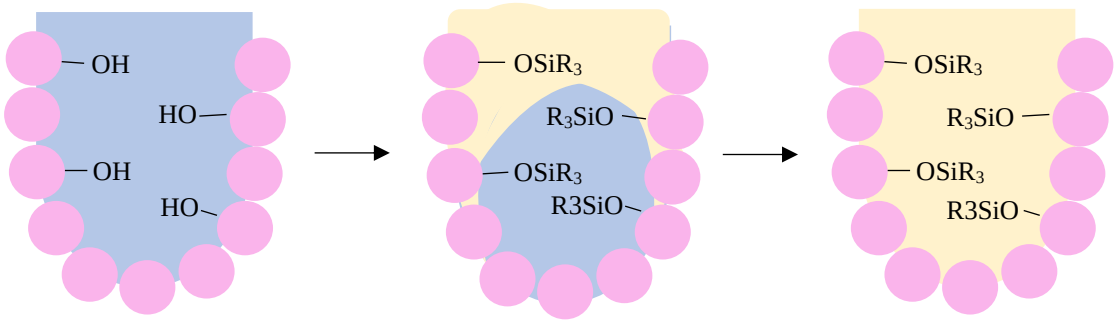

Figure.2.9. Illustration of surface modification and pore water (blue) is replaced by organic solvent (yellow) during solvent exchange. Pore water is expelled from the pore because the surface is hydrophobized.

2.2 Silica Aerogel as Support Material

The remarkable properties of silica aerogels, such as low density, high surface area and open porosity and good thermal stability, make it an attractive candidate as a catalyst support. Efficiency of a catalyst greatly depends on the dispersion of active material on the surface. Larger surface area provides higher dispersion of the active material and so favours the accessibility to active sites for catalysis. [49] The open porous networks of silica aerogel are interconnected and allow rapid mass transport of reactants and products while preventing sintering due to increase in particle mobility at high temperature. Sintering is the process of thermal induced deactivation of catalysts resulting from the migration of particle and forming clusters. The dispersion of active material is then reduced and so affect the catalytic performance. Silica aerogel also provides good reactant and product selectivity base on the pore size of the aerogel. [4, 50] Surface modified aerogel is thermally stable that can resist the loss of surface area due to pore collapse.[51] The presence of organosilane groups on the modified surface prevent the formation of Si–O–Si bond that leads to irreversible shrinkage when pore solvent evaporates. All these unique properties play a significant role in determining the overall catalytic performance.

2.2.1 Incorporation of Cobalt into the gel matrix

Introduction of cobalt into silica aerogel has been studied extensively. [4, 24, 52-55] There are many ways to introduce cobalt into the gel matrix. One of the methods is the incipient wet impregnation. It can be done by impregnating silica gel in a solution containing metal precursors with the volume corresponding to the total pore volume of the support. The catalyst is then dried and calcined to remove the volatile compounds in the solution. The active metals then deposit on the support surface.[56] This method depends on the solubility of metal precursor in solution and its interaction strength with support material. If the interaction is low, the impregnated species could redistribute and agglomerate into metal oxides, resulting in the loss of dispersion and catalytic activity. [57, 58]

The efficiency of a catalyst depends on the distribution of the active phase. Single site heterogenous catalysts (SSHC) give a better dispersion of active phase because the metal is

well separated throughout the structure. Single site is referred to the active site that is spatially isolated from one another. Each site has the same local chemical environment, as well as having the same energy of interaction between the active sites and reactants. [10] SSHCs have been extensively used in industrial chemical process, such as cracking of hydrocarbons, isomerisation, alkylation and polymerization.[59] It combines the merits of both homogenous and heterogenous process, regarding to facilitate the separation of product from reactants and provide precise control over activity, selectivity and stability of the catalyst.[11] Therefore, it offer processing advantages in larger scale and industrial operations.

According to the synthesis route reported by Kristiansen et al. [13], active metal in single site is successfully synthesis by incorporating metal cations into waterglass based silica aerogel during sol-gel process, which is also used in this work. The incorporation is done by dissolving cobalt precursors in the sol prior to gelation. Cobalt cations react with the siloxy group ($-SiO^-$), bound and stabilize in the gel matrix. [58] Adding cobalt precursor into the sol prior to gelation can ensure cobalt is evenly distributed throughout the gel matrix and is incorporated in single site, meaning there is no $-Co-O-Co$ species in the gel network. Several factors can affect the possibility of cobalt being incorporate into silica aerogel in single site. For example, the number of siloxy group ($-SiO^-$) on the growing silica particles decreases as pH decreases. Therefore, the uptake of cobalt into the acid catalysed silica aerogel is lower than the base catalysed gel. However, high pH of the sol leads to the formation of cobalt hydroxide instead of reacting with the siloxy group ($-SiO^-$) and fail to incorporate cobalt into silica aerogel. Therefore, pH of the sol is crucial for successful incorporation of cobalt. The coordination of introduced is expected to distribute between tetrahedral and octahedral. [60]An illustration of the framework of a single site cobalt- silica aerogel is given in Figure 2.10.

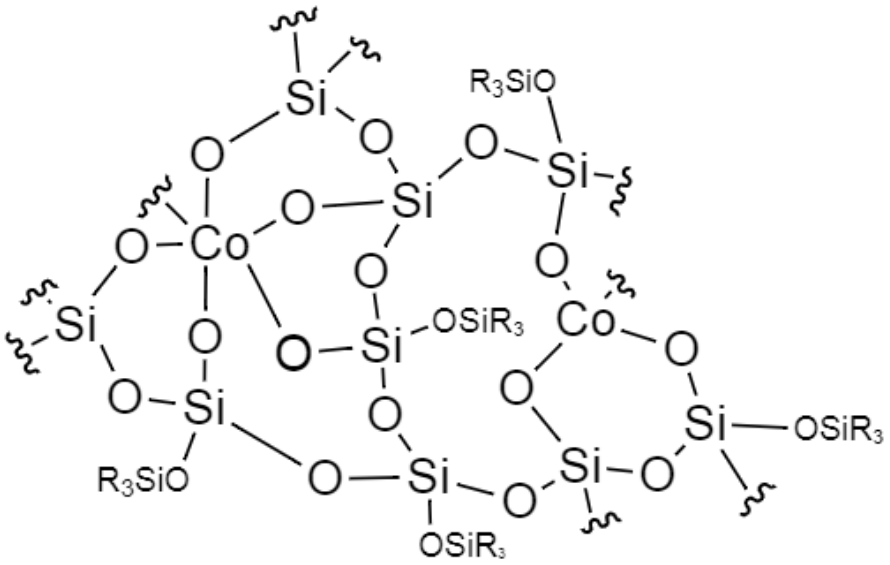

Figure.2.10. Structure of single site cobalt silica aerogel

2.3 Characterisation techniques

2.3.1 Powder X-ray Diffraction

X-ray Diffraction is a non-destructive technique to provide chemical compositions and crystallographic structures of material. The diffraction phenomenon for each individual crystallite in the powder sample can be determined by powder XRD.[61] However, amorphous material and highly dispersed atomic species cannot be characterised by XRD. In this project, powder XRD is used to exclude the presence of crystalline phase in the sample since silica aerogels are amorphous materials.

When a monochromatic x-ray beam focused to the sample, x-ray photons are elastically scattered by the atoms in the lattice with spacing distance *d* between crystal planes. The beam of certain wavelength projects on the crystal plane at an angle θ and the scattered beam is collected at 2θ. The scattered waves that are in phase will have constructive interference and will show as a signal in the diffractogram while the scattered waves that are out of phase will have destructive interference and do not show as a signal in the diffractogram. [62]

To fulfil the Bragg's law, constructive interference occurs when spacing distance between crystal planes is equal to an integer number of wavelengths. The equation is given below.

$$n\lambda = 2d \sin \theta \qquad (7)$$

where n is an integer

θ is the angle between incident beam and determined crystal

d is the spacing distance

The diffractogram obtained provides fingerprint information about the crystalline phase in the material.[63] The intensity of the peaks are related to the type of atom in the crystallographic lattice in which waves are constructively added according to the d spacing. Shape and position of the peaks are also related to the structure, crystalline size, heterogeneity and micro-deformations.[62]

A diffractogram of plain silica aerogel was shown in Figure 2.11. The board reflection signal in the XRD diffractogram attributed to the amorphous structure of the gel.

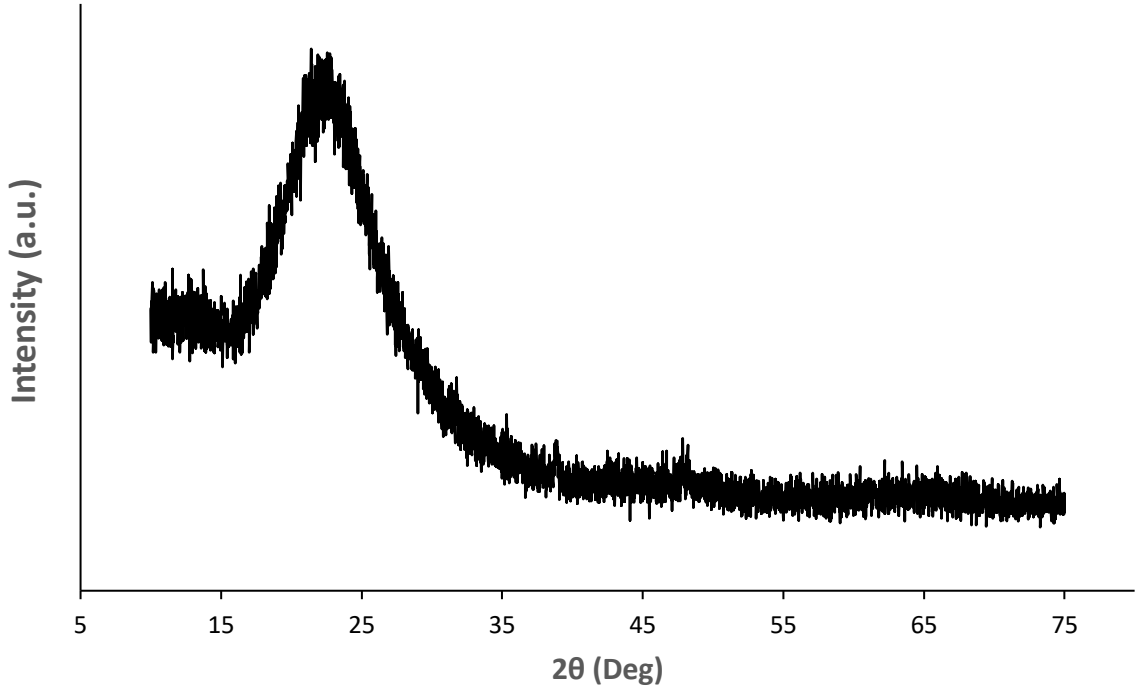

Figure 2.11. X-ray diffraction pattern of plain silica aerogel

2.3.2 Nitrogen Adsorption and Desorption Isotherms

Specific surface area of the porous material can be determined by the adsorption isotherm techniqe. The condensation of gas on the surface depends on the physisorption that involves weak intermolecular force, Van der Waals force, between the surface (adsorbent) and the gas (adsorbate). This technique can also be used to determine the pore sizes by the phenomenon of capillary condensation. The adsorption equilibria can be represented by isothermal plot which shows the quantity of gas adsorbed on the surface at a specific temperature. Nitrogen gas is commonly use as a probe gas for this analysis. In Figure 2.12, the isothermal plot shows the quantity of adsorbed gas in a function of relative pressuer, P/P_s, where P_s is the saturated vapour pressure of the gas at the measured temperature. For nitrogen, the measured temeperature is 77K. [63]

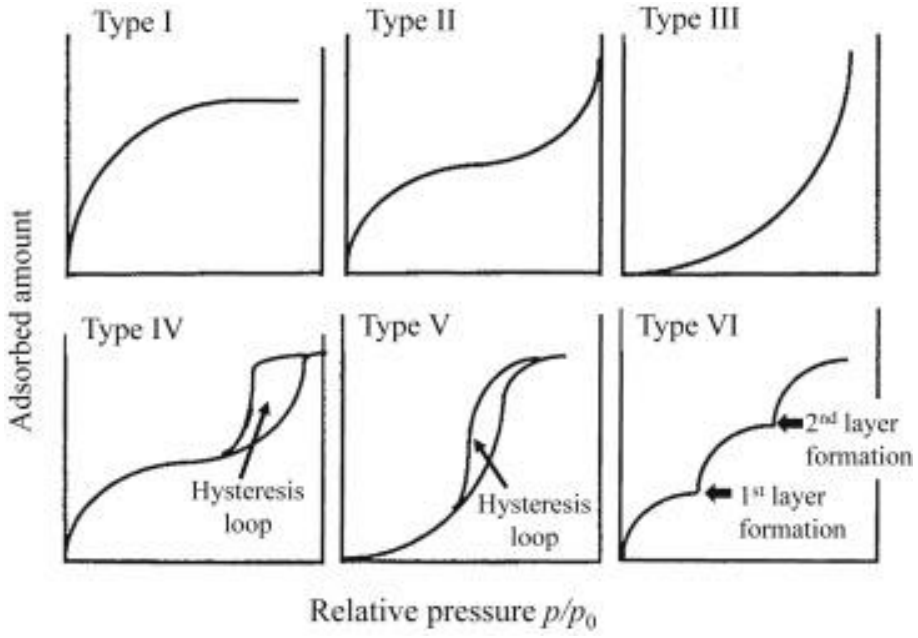

Figure 2.12. Six adsorption isotherms of the IUPAC classification. Reprinted with permission from Nishi et al.[64] Copyright 2016 Elsevier

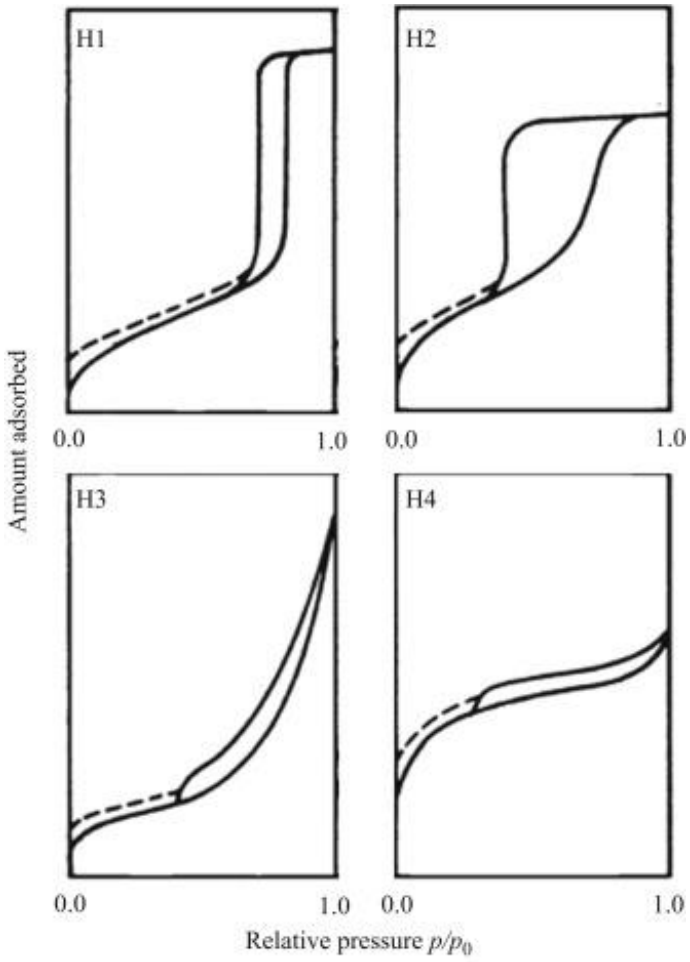

Figure 2.13. Four hysteresis loops of the IUPAC classification. Reprinted with permission from Nishi et al.[64] Copyright 2016 Elsevier

The forms of the isotherms correspond to the average radius of pores and the intensity of the Van der Waals force between gas molecuels and the surface. Type I isotherm is given by solid with micropores (pore size < 2nm) that have relatively small external surface area. Type II isotherm is associated with non-porous or macropores (pore size >50nm) materials which representing a unrestricted monolayer- multilayer adsorption. Type IV isotherm is observerd for solid with mesopores (2-50nm). It has an adsorption hysteresis which is associated to the capilliary condensation in the mesopore structure. A phase transition occurs due to the condensation of gas phase in the pores. Type VI isotherm characterizes stepwise multilayer adsorption on a surface with no apparent porosity. [63, 65]

The shapes of hysteresis loops are found to be associated to structure of pores. (Figure 2.13) H1 type hysteresis loop corresponds to porous material that consist agglomerates and hence to have narrow the pore size distribution. H2 type hysteresis loop associates with porous material which has non-uniform pore shape and size due to the network effect that blocking the pores. Therefore, the pore size distribution of this time is not well defined. H3 type and H4 type hysteresis loops are observed with aggregate of plate-like particles and form slit-shaped pores. H3 hysteresis loop associates with solids consisting of non-uniform pore sizes whereas H4 hysteresis loop is associated with uniform pore size.[63, 65] For a silica aerogel, a type IV isotherm that indicating the presence of high amount of mesopores is expected. [66]

Determining the specific surface area

Brunauer, Emmett, Teller (BET) method is applied to determine the specific area of the porous material. This method is based on the Langmuir theory which assumes that all site have the same energy and the surface is homogenous. Each active site only accepts one adsorbed molecules and these molecules are small enough to completely cover the surface of solid. The intermolecular forces between adsorbed molecules are considered to be negligible. Adsorption energy of the second and subsequent layers are constant. [63] The linear expression of BET equation is expressed below:

$$\frac{P}{V(P_0-P)} = \frac{1}{V_m+C} + \frac{C-1}{V_m C}\frac{P}{P_0} \qquad (8)$$

where P is the equilibrium pressure

P_0 is the saturated vapour pressure

V is the chemisorbed volume

V_m is the volume of a monolayer (cm^3/g)

C is the BET constant characteristic of the heat of adsorption

A straight line $\frac{P}{V(P_0-P)}$ as a function of $\frac{P}{P_0}$ is used to obtain V_m from the slope and the intercept. The BET surface is then can be calculated using the following :

$$S_{BET} = \frac{NAV_m 10^{-20}}{mV_M} \quad (9)$$

where N is Avogado's constant

A is the area occupied by an adsorbate molecule; for N_2: A=0.162 Å

V_M is the molar volume (22414cm^3/mol)

V_m is the volume of a monolayer (cm^3/g)

m is the mass of the solid analysed

Determining the pore volume or pore size distribution

Barrett- Joyner- Halenda (BJH) method is based on the capilliary condensation phenomenon. The average pore size can be calculating from the Kelvin's equation that relating the adsorbate condensation pressure P_c to the radius of the pore r_p (Equation 10). The pore distribution can be shown by plotting the curve dV/dr_p versus r_p. [63]

$$ln\frac{P_C}{P_0} = \frac{-f\gamma V\cos\theta}{RTr_k} \quad (10)$$

where P_c is the condensation pressure

f is the form factor

γ is the molar volume (22414cm^3/mol)

V is the molar volume of liquid

θ is the angle of contact

R is the gas constant

T is the temperature

r_k is the radius of the meniscus formed within the pore

2.3.3 Inductive Coupled Plasma Mass Spectrometry

Inductively coupled plasma mass spectrometry (ICP-MS) is one of the most important technique for elemental analysis. It has a technique with high accuracy and precision due to its low detection limits for most elements. Liquid samples must be used for analysis, therefore, sample preparation is needed for solid samples. Liquid samples are ionized by inductively coupled plasma and produces positively charged ions. Once the ions are produced, they are directed into the mass spectrometer. Mass spectrometer is a device that separates ions according to their mass-to-charge ratios (m/z). Ions finally reach the detector that convert the beam into an electrical signal that can then be read and stored by a computer. [67, 68] ICP-MS can be used for both qualitative and quantitative analysis. Different elements and isotopes can be identified base on its m/z ratio where the concentration of elements can be determined by drawing a calibration curve with standard solutions.

3 X-RAY ABSORPTION SPECTROSCOPY

X-ray absorption spectroscopy (XAS) is a powerful technique to study the structural and electronic properties by acquiring information about the local environments, oxidation states and coordination number of a target element in a material. XAS is an element-specific technique that sensitive to the local geometric and electronic structure of an absorber. It is also one of the few structural probes available for systems without highly disordered and noncrystalline materials, therefore it can be used for analysing amorphous materials, such as silica aerogel.[69]

XAS measurements is performed at a synchrotron which can provide an intense and energy tunable source of x-ray. When electrons are accelerated with a speed close to the speed of light and their path is bent by a powerful magnet, a high energy electromagnetic radiation is emitted. The radiation travels from the synchrotron to the beamline. The beam can be focused by the x-ray mirror onto the monochromator to tune x-ray energy to the energy where a core electron can be excited, then focusing on the sample.[70] When the x-ray photon bombards the sample, energy is absorbed by the atoms in the sample, causing excitation or ejection of an electron from the core. The atom that absorb x-ray energy is so-called an absorber. For the absorption of energy to occur, the binding energy of this core election must be less than the energy of the incident x-ray. Due to the requirement of the specific x-ray energy for excitation, it makes XAS an element-specific technique. After the beam passed through the sample and is detected.[71]

The absorption coefficient (μ) is measured as a function of photon energy either in transmission or in fluorescence. When the beam passes through the sample, it interacts with the atoms in the samples causing absorption of energy. The absorption coefficient can be calculated from Beer-Lambert's Law: [71]

$$\mu(E)x = \ln\frac{I}{I_0} \tag{11}$$

where x is the thickness of the sample

I_0 is the intensity of the incident beam

I is the intensity of the transmitted beam

An XAS spectrum consists of two main regions: X-ray Absorption Near Edge Structure (XANES) and Extended X-ray Absorption Fine Structure (EXAFS). XANES is the region that the energy range contains the pre-edge, the absorption edge and the features within 50 eV below and 100-150 eV above the edge. For EXAFS, the energy range is from 150eV to 1000eV above the edge. A full normalized XAS spectrum of Co_3O_4 is shown in Figure 2.14.

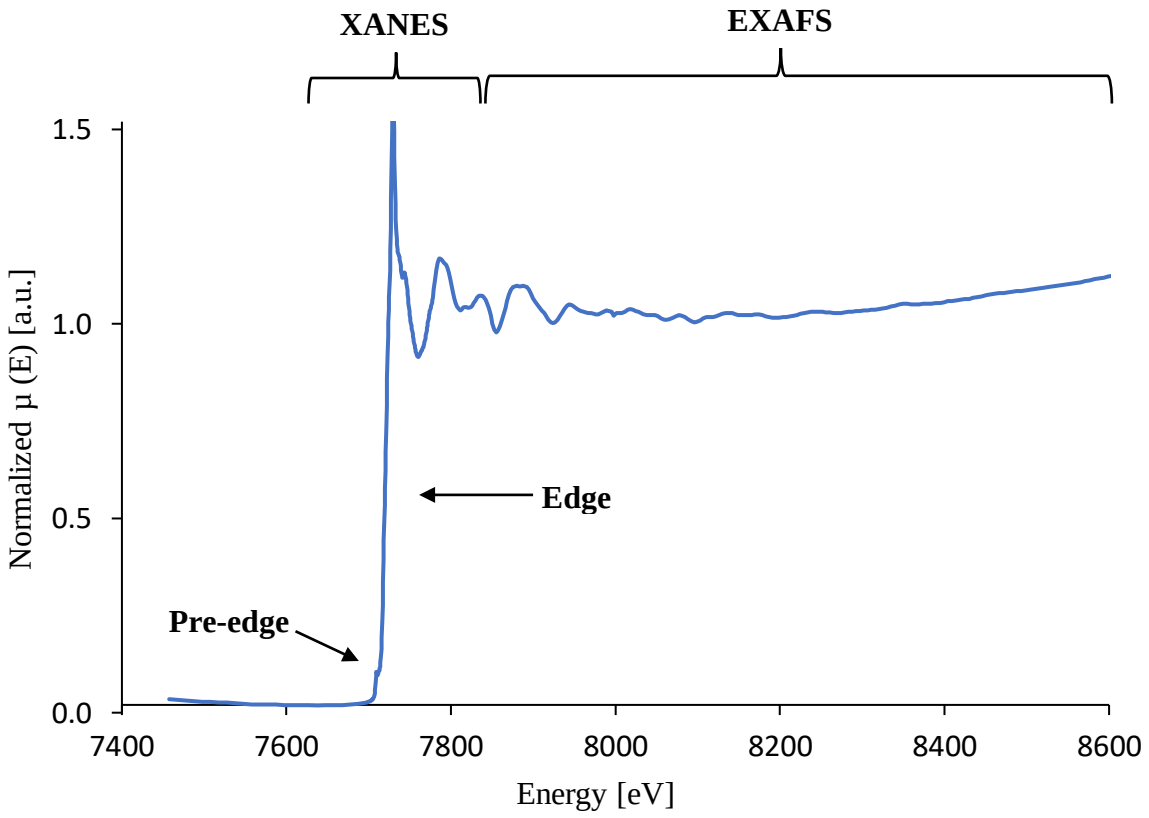

Figure 2.14. A normalized XAS spectrum of Co_3O_4 including the XANES and EXAFS regions.

3.1 XANES

The features of the XAS spectrum near or on the edge are known as XANES. (Figure 2.15) The absorption peaks in this region is attributed to the situations when the photon energy matches the energy required to excite the core electron into an empty valence level, or completely eject the electron into the continuum, resulting in ionization of atoms.[71]

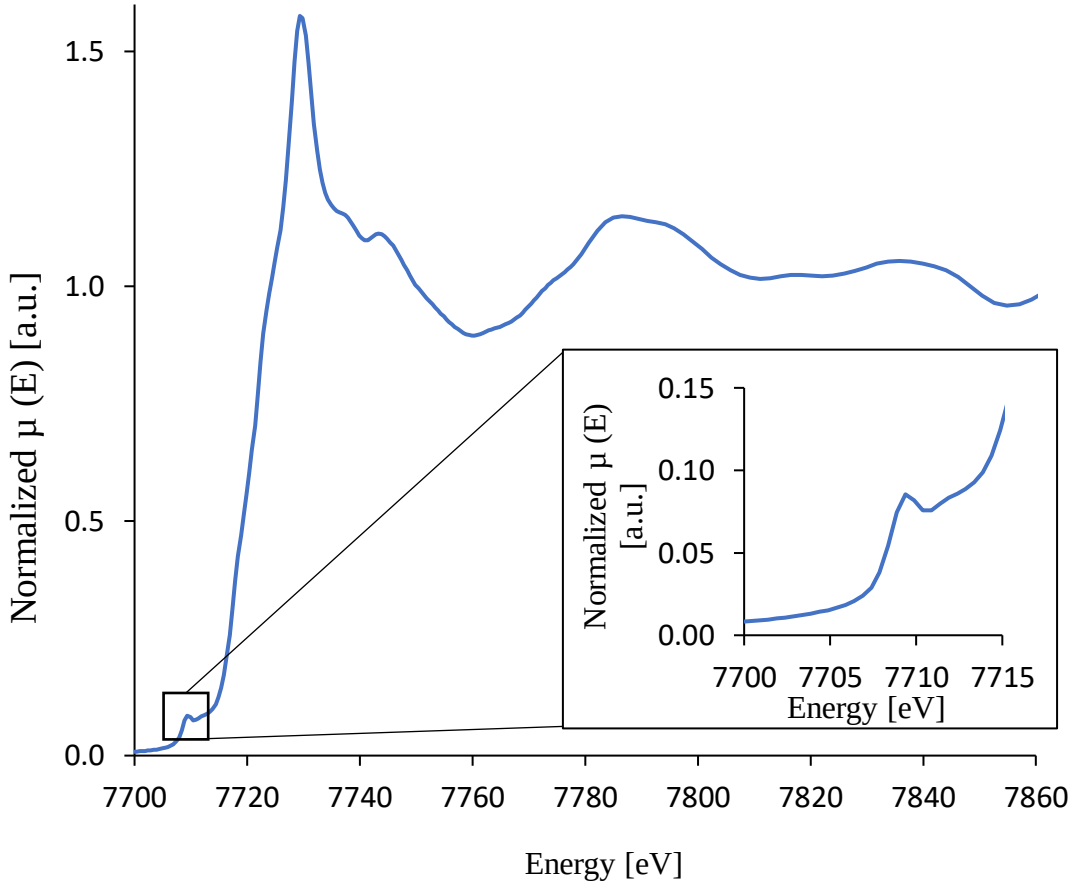

Figure 2.15. A XANES region of the normalized XAS spectrum of Co_3O_4 showing pre-edge (in the box) and then absorption edge.

The pre-edge that locates before the edge is attributed to the transition of the core electron to a higher energy level. (Figure 2.15) These peaks give information about oxidation state and site symmetry of the target element. The energy position and intensity of the pre-edge depend on the number of unoccupied states in d-orbital and the local symmetry around the absorber.[72]

When an electron is excited, only some high energy excited states is available for transition and the selection rule determines if the electronic transition is allowed or forbidden. The Laporte selection rule applies to molecules that containing a centre of inversion. It states that the transition between two gerade (g) states or two ungerade (u) states are forbidden. Only transitions between a g state and u states are allowed. Gerade (g) and ugerade (u) is referred to the even and uneven symmetries respectively with respect to the centre of inversion. In other words, transitions are forbidden if the ground state and excited state have the same symmetry with respect to the centre of inversion, for examples transitions s⟶s, p⟶p, d⟶d, f⟶f and s⟶d are forbidden where transitions s⟶p, p⟶d and d⟶f are allowed.[73]

A comparison of the intensity of the pre-edge can be used to estimate the site symmetry of target element. In octahedral complexes, transition, such as s⟶d, is forbidden by the selection rule. However, the s⟶d transition still happens in the first-row transition metal because of the symmetry distortion through the mixing of 4p orbitals with unoccupied 3d orbitals. This mixing can be seen in the XAS spectrum as a pre-edge with weak intensity.[74] On the other hand, due to the absence of inversion centre in tetrahedral complexes, none of the electronic transmission violate the Laporte rule. Therefore, the electronic transition in tetrahedral complexes is more intense than the transition in octahedral complexes.[73] Number of unoccupied 3d states can also affect the intensity of the pre-edge. The probability of s⟶d transition is higher in atoms with less filled d-orbitals than atoms with more occupied d-orbitals. Hence, different oxidation state of atoms can be observed by comparing the intensity of pre-edge. For example, Co^{3+} species that has 4 unoccupied d orbitals gives a higher intensity pre-edge compare to Co^{2+} species that has 3 unoccupied d orbitals.[1]

When photon energy continues to increase, it reaches an energy level that equal to the electron binding energy, causing the ejection of an electron from the core level to the continuum. This leads to a sharp rise in absorption coefficient that can be seen in the XANES spectrum. (Figure 2.15) This energy level is called the absorption energy, E_0. Each edge occurs corresponding to the excitation of core electrons, K-edge for the 1st electrons, L for the second shell electrons, etc. The position of the absorption energy is sensitive to the oxidation state of the target element. For atoms with higher oxidation state, the removal electrons cause an increase in effective nuclear charge felt by the valence electrons. The valence electrons are pulled closer towards

the nuclear and the attraction force between electrons and nuclear increases. Therefore, more energy is required to remove the electrons from the core level, shifting the position of the absorption edge to a higher value. However, this shift can also govern by the local environment of the atom, including the covalent character of the bond, nature of the ligands, the electronegativity of the anion and coordination numbers.[75]

3.2 EXAFS

Beyond the absorption edge, it is where the electron excited into the continuum and interact with neighbouring atoms, producing EXAFS. When x-ray ejects an electron from an atom, that electron, so-called photoelectron, radiates out as photoelectron wave in all direction. The wave scatters off by neighbouring (B) atoms and returns to the original absorbing atom (A). (Figure 2.16) The backscattering causes the wave to interfere constructively and destructively. The presence of these backscattering from the neighbouring atom will then change the absorption coefficient, resulting in the fine structure oscillations in μ(E) above the edge. These interferences can be affected by the local environment around the absorber, such as distance from the absorber, types of neighbouring atoms and wavelength of the waves, but also affected by static and thermal disorder.[76]

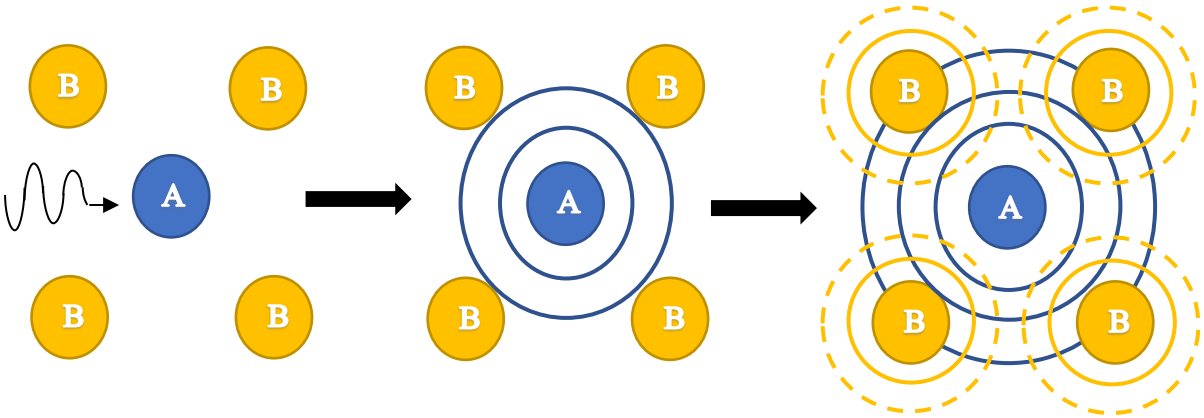

Figure 2.16. Illustration showing the target atom absorbs (blue) incoming x-ray beam and produce photoelectron waves (blue waves). The waves are backscattered (orange dotted line) by neighbouring atoms (orange).

The structural information can be extracted from the oscillations by normalizing the isolated

EXAFS region, giving the EXAFS fins-structure function χ(E) as following: [71]

$$\chi(\mathrm{E}) = \frac{\mu(E)-\mu_0(E)}{\Delta\mu_0(E)} \quad (12)$$

where $\chi(E)$ is normalized EXASF region of the XAS spectrum

$\mu(E)$ is the absorption coefficient as a function of photon energy

$\mu_0(E)$ is the absorption of an isolated atom

$\Delta\mu_0(E)$ is the measured absorption jump at the absorption edge

Due to the wave behaviour of the photoelectron, the x-ray energy is then converted to the wave number of the photoelectron (k) that has the dimensions of $Å^{-1}$. It can be calculated as [71]

$$\mathrm{k} = \sqrt{\frac{2m(E-E_0)}{\hbar^2}} \quad (13)$$

where m is the electron mass

$(E-E_0)$ is the kinetic energy of the electron

ħ is the reduced Planck constant

Since the oscillations of EXAFS decay quickly as k increases. χ(E) is often multiplied by a power of k ie k^3 to get a plot with more uniform amplitude.[72] Heavier neighbouring atoms and higher coordination number gives greater amplitude of the oscillation. Therefore, atomic number of the neighbouring atoms and coordination number of the absorber can be estimated. χ(E) of Co_3O_4 is given in Figure 2.17.

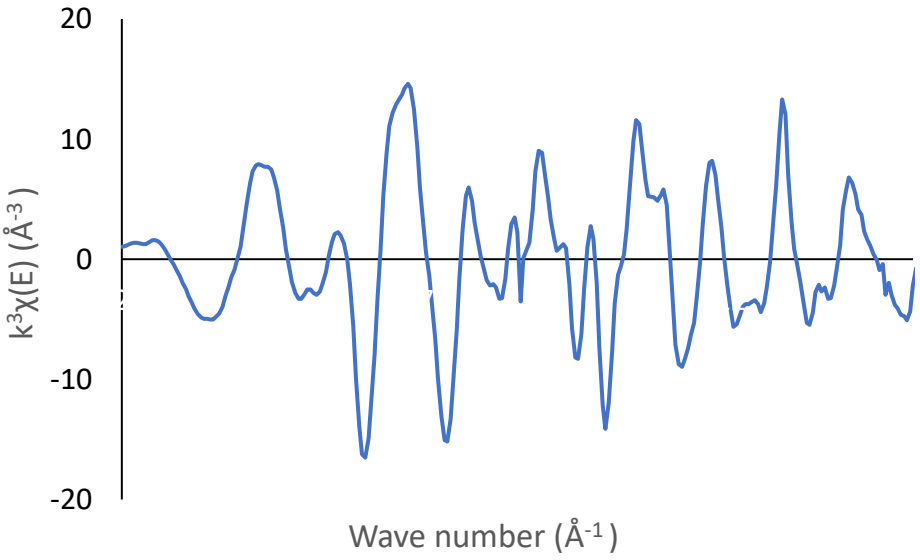

Figure 2.17. Experimental measured EXAFS χ(E) of Co_3O_4 obtained after isolated from XAS spectrum.

Information of the structure nature of sample can be extracted by using the EXAFS equation. (Equation 14) The EXAFS equation is sum of sinusoidal wave that result from backscattering of photoelectron.[72] In this step, structural parameters can be extracted from the equation by trying to fit the theorical χ(k) to the experimental measured χ(k).

$$k^n\chi(\mathrm{k}) = k^{n-1}\sum_{j=1}^{shell}\frac{N_j}{kR_j^2}F_j(k)S_j(k)e^{-2k^2\sigma_j^2\frac{2r_j}{e^{\lambda(k)}}}\sin[2kr_j+\phi_{\mathrm{j}}(k)] \qquad (14)$$

where $k^n\chi(k)$ is the k^n - weighted χ(k)

N_j is the coordination of the j_{th} shell

$S_i(k)$ is the electron mass

k is the wave number

r_j is the distance between the absorbing atom and the j_{th} shell

$F_j(k)$ is the backscattering amplitude factor of the j_{th} shell

σ_j^2 is the Debye Waller factor for the j_{th} shell

$\lambda(k)$ is the inelastic electron mean free path

$\phi_{ij}(k)$ is the phase shift

For the EXAFS analysis, a good fit of the theoretical curve to the experimental curve is required to extract reliable structure information. Amplitude of EXAFS can tell the distance between absorber atom and neighbouring atoms (R), coordination number (N) of the absorber atom. The longer the distance, the weaker the EXAFS will be. For a given backscattering at distance R, the amplitude increases linearly with the N. Identity of neighbouring atoms can also be told from the amplitude and phase-shift, because of their dependence on atomic number. Scattering amplitude of lighter atoms decay as k increases. EXAFS data can also be used to get information about disorder in neighbouring atoms by calculating the Debye-Waller factor which is a measure of the variance of distance R due to static and thermal disorder. [77]

The final step to complete the data extraction on EXAFS is to Fourier transform (FT) the χ(k) function into R-space, χ(R). (Figure 2.18) The spectrum shows the contribution of each shell as a function of radial distribution. FT is a useful tool to isolate the shell for determine the type of neighbouring atoms.

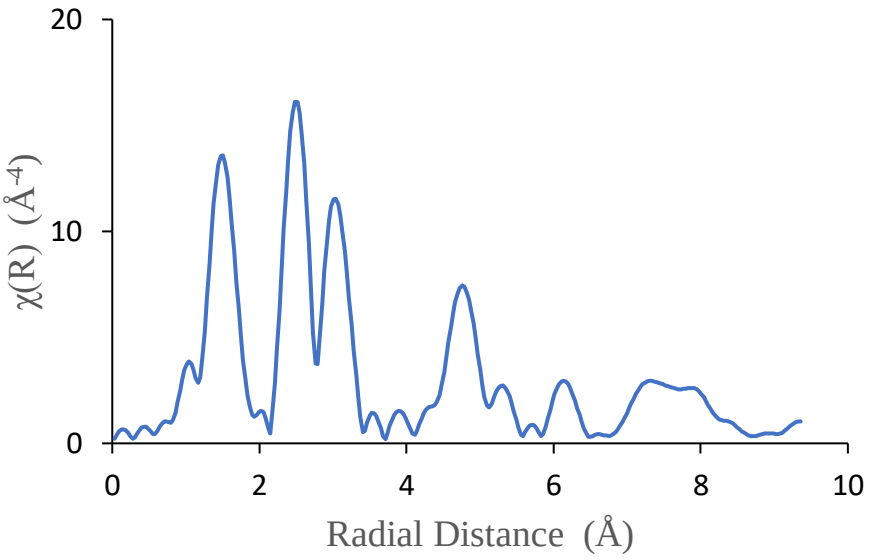

Figure 2.18. EXAFS χ(R) of Co_3O_4 obtained by Fourier transforming the χ(k) of Co_3O_4

4 EXPERIMENTAL

4.1 Preparation of Silica Aerogel

The silica gel was produced via sol- gel method under inert gas, by flushing N_2 into the apparatus. Sodium silicate (Na_2SiO_3, 27.2%, Merck KGaA) was used as starting material. Cobalt was introduced into the sol prior to gelation. The experimental procedure is illustrated as a flow chart in Figure 4.1. Different parameter studies were performed, such as testing different cobalt precursors and surface modification agents, varying pH, temperature and molar ratio of cobalt added to the silica gel during synthesis.

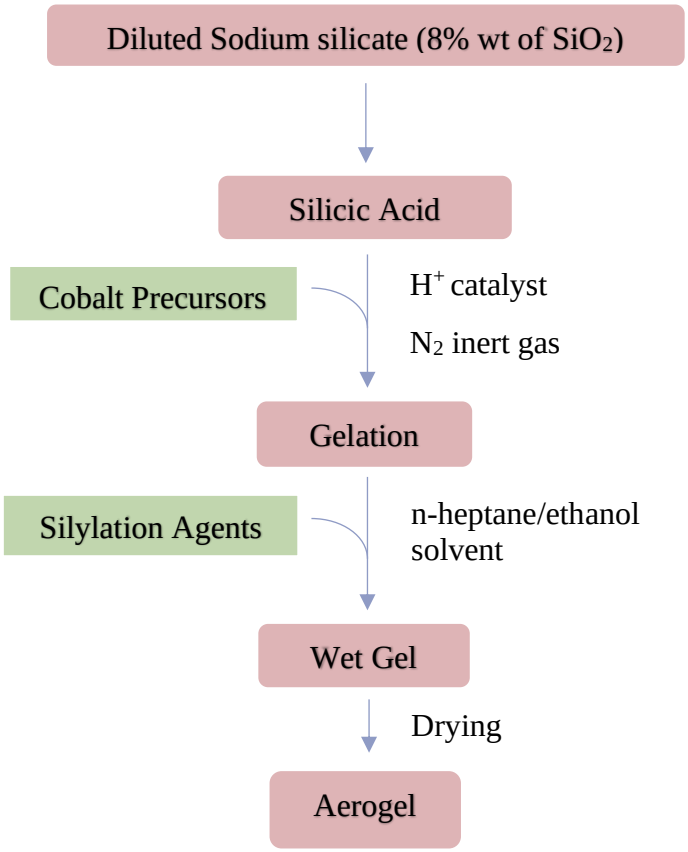

Figure. 4.1 General experimental procedure

i. Sol-gel Process

Stock sodium silicate solution, as known as waterglass solution, was diluted with distilled water to obtain a solution with 8%wt of silica. The diluted solution was pass through a column filled with Amberlite with a 1:1 volume proportion for ion exchange. pH of the collected solution was about 2.6, which indicating the formation of silicic acid. The sol was then transferred to a round bottom flask (RBF) that was flushed with nitrogen gas. The set-up of apparatus is shown in Figure. 4.2. Cobalt precursors were added in the sol while stirring vigorously. After all cobalt salt were dissolved, ammonium hydroxide (NH_4OH, 1.0M, Sigma-Aldrich) was added to the sol while stirring to elevate the target pH for gelation. After gelation occurred, the gel was aged under inert gas at ambient temperature for 24h.

Figure. 4.2 An illustration of the set up for sol-gel process.

ii. Surface modification via SD method

After aging, the wet gel was surface modified via instantaneous solvent exchange/surface modification (ISE/SM) method by soaking it in a solution containing a mixture of alcohol, linear saturated hydrocarbon and surface silylation agent for 24 hours.[31] In this work, HMDSO and TMCS was used as the silylation agent. This step was performed under inert gas, N_2, at certain temperature. In this work, 4 different temperatures, room temperature (r.t), 50°C, 55°C and 60°C, was chosen for surface modification. The set up used for surface modification is shown in Figure 4.3. The RBF was connected to a condenser and was heated in an oil bath. A thermometer was used to monitor the temperature of the oil bath. After surface modification was completed, the gel was removed from the solution and was transferred to a petri dish for drying.

Figure. 4.3 Set up for surface modification process.

iii. Drying

Sample was dried in static air under ambient pressure in an oven with the following heating procedures: starting from 25ºC, heat at 65 ºC for 18h, 85 ºC for 3hr and 120 ºC for 2h, all steps with the heating rate at 5 ºC/min. [13]

iv. Heat Treatment

Two different heat treatment, annealing and calcining, was applied to all sample for testing thermal stability of samples. Sample was annealed at 450 ºC for 30 minutes with the heating rate at 5 ºC/min and was calcined at 700 ºC for 3 h with the heating rate at 10 ºC/min. [13]

4.2 Parameter Studies

In this work, all cobalt silica aerogels were synthesised by sol-gel process using sodium silicate as a silicon precursor. The wet gels produced were surface modified via SD method, aged for 1 day and were dried by APD. Different parameter studies were performed in order to investigate the possibility of incorporation of cobalt into the gel matrix. (Section 4.2.1- 4.2.4) The overview of all parameters studied was shown in Appendix A.

4.2.1 Varying Cobalt Precursors and Silylation Agents

The effects of different cobalt precursors and silylation agents were studied by preparing ten gels as described in section 4.1. The selection of cobalt precursors was based on its solubility in water because the diluted waterglass contains about 92% of water. In this study, four different types of precursor were used:

1. cobalt (II) nitrate hexahydrate, $Co(NO_3)_2 \cdot 6H_2O$;
2. cobalt sulphate, $CoSO_4$;
3. cobalt chloride hexahydrate, $CoCl_2 \cdot 6H_2O$;
4. hexamine cobalt (III) chloride, $[Co(NH_3)6]Cl_3$

For each the cobalt silica wet gel, except the gel using hexamine cobalt (III) chloride as the cobalt precursor, three different solution of silylation agents were applied for the surface modification.

a. Trimethylsilyl chloride (TMCS);
b. Hexamethyldisiloxane (HMDSO);
c. Mixture of TMCS/ HMDSO.

All chemicals were bought from Sigma-Aldrich. The overview of the parameters for this section is shown in Figure 4.4.

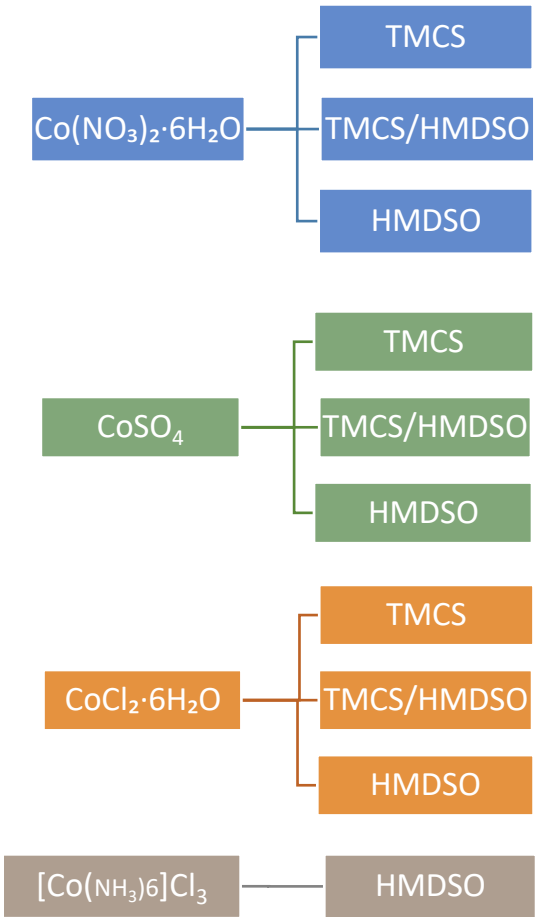

Figure. 4.4 Overview of the synthesis parameters of Co- Silica gel by varying type of cobalt precursors and silylation agents

All ten gels were prepared with constant molar ration of Si: H_2O =40 and Si: Co =0.1. The gels were also prepared at pH 4 in room temperature (r.t). During surface modification, all gels were immersed in organic solvent containing silylation agents, n-heptane (C_7H_{16}: HMDSO= 6.25) and ethanol (EtOH: Si= 21) as done in previous works [1, 13, 39]. All samples were surface modified at room temperature. The preparation conditions of the gels for this section is given in Table 4.1.

Table 4.1 Synthesis parameter including type and molar ratio added of cobalt precursor and reagent used

Sample Name	**Cobalt Precursor**	**Molar ratio Si: H_2O: TMCS: HMDSO**			
		Si	H_2O	TMCS	HMDSO
N(II)-T	$Co(NO_3)_2 \cdot 6H_2O$	1	40	14	
N(II)-T/H				7	3.5
N(II)-H					7
S(II)-T	$CoSO_4$			14	
S(II)-T/H				7	3.5
S(II)-H					7
C(II)-T	$CoCl_2 \cdot 6H_2O$			14	
C(II)-T/H				7	3.5
C(II)-H					7
A(III)-H	$[Co(NH_3)_6]Cl_3$				7

4.2.2 Varying Gelation pH Values

In this section, four gels were prepared at different pH ranging from 4 to 7 for gelation. VWRpHenomenal® pH 1100L was used to monitor the pH of the sol while adding NH_4OH. $Co(NO_3)_2 \cdot 6H_2O$ was used in the preparation for all samples with constant molar ratio H_2O: Si = 40 and Co: Si = 0.1. HMDSO was used as the silylation agent and, all gels were immersed in n-heptane/ethanol solvent with constant molar ration C_7H_{16}: HMDSO= 6.25 and EtOH: Si = 21 at room temperature. The overview of the parameters for this section is shown in Figure 4.5 and the preparation conditions, including molar ratio of reagents used and gelation pH, is given in Table 4.2.

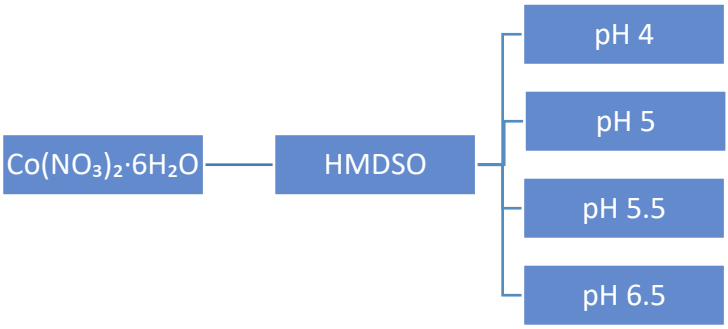

Fig. 4.5 Overview of the synthesis parameters of Co- Silica gel by varying pH for gelation

Table 4.2 Synthesis parameters including type and molar ratio of cobalt precursor and reagent used, and pH for gelation

Sample Name	**Cobalt Precursor**	**Molar ratio Si: H_2O: HMDSO: EtOH: Co**	**pH**
N(II)-H_pH4	$Co(NO_3)_2 \cdot 6H_2O$	1: 40: 14: 21: 0.1	4
N(II)-H_pH5			5
N(II)-H_pH5.5			5.5
N(II)-H_pH6.5			6.5

4.2.3 Varying Exchange Solvents and Temperature

The effects on the pore structure and the possibility of cobalt introduction into the gel were studied under different conditions by varying temperature (50-60 °C) and organic solvent mixture (n-heptane/ethanol and n-hexane/ethanol) used for ISE/SM. In this section, two cobalt precursors, $Co(NO_3)_2 \cdot 6H_2O$ and $CoSO_4$, were used for the preparation of cobalt silica aerogels with constant molar ratio H_2O: Si = 40 and Co: Si = 0.1. Gelation was happened at pH 4. HMSDO was used as the silylation agent for all sixteen samples. The overview of the parameters for this section is shown in Figure 4.6 and the preparation conditions is given in Table 4.3.

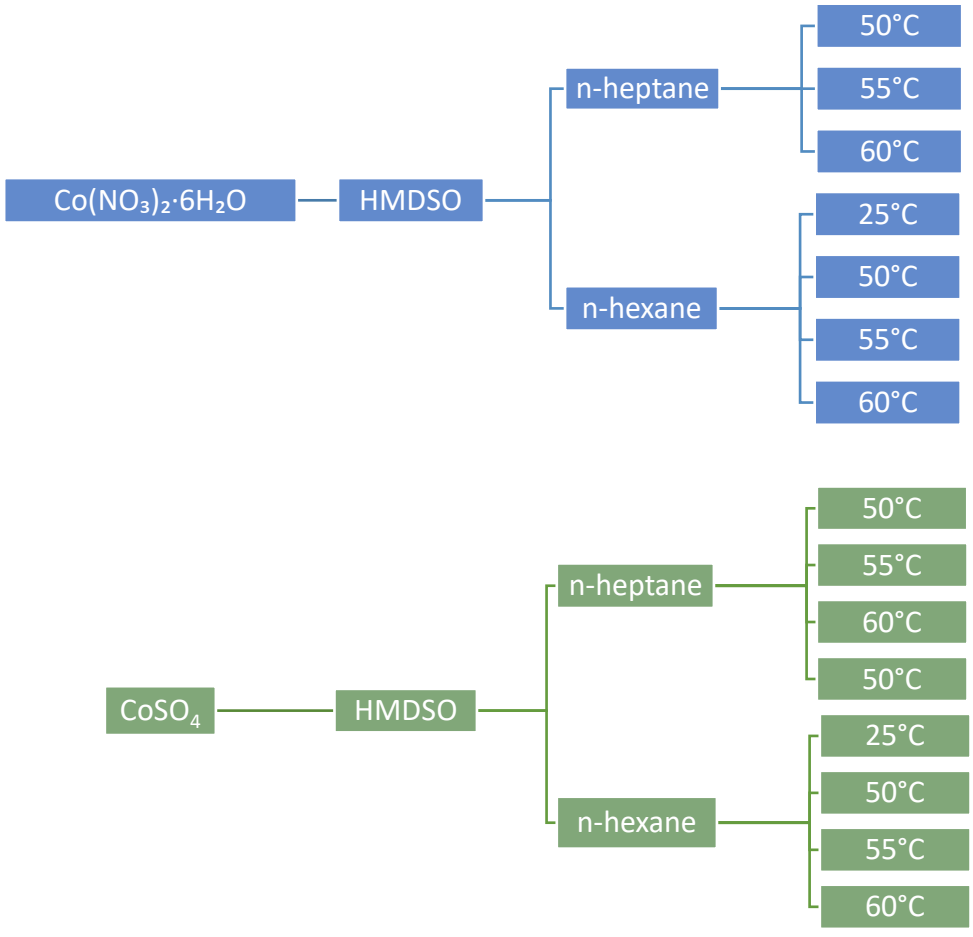

Fig. 4.6 Overview of the synthesis parameters of Co- Silica gel by varying organic solvent and temperature

Table 4.3 Synthesis parameters including type of cobalt precursor, molar ratio of organic solvent used and temperature for surface modification.

Sample Name	**Cobalt Precursor**	**Molar ratio HMDSO: C_7H_{16}: C_6H_{14}**	**Temperature (°C)**
N_C_7_50C	$Co(NO_3)_2 \cdot 6H_2O$	1: 6.25: 0	50
N_ C_7_55C			55
N_ C_7_60C			60
N_C_6_50C		1: 0: 6.25	50
N_ C_6_55C			55
N_ C_6_60C			60
S_ C_7_50C	$CoSO_4$	1: 6.25: 0	50
S_ C_7_55C			55
S_ C_7_60C			60
S_ C_6_50C		1: 0: 6.25	50
S_ C_6_55C			55
S_ C_6_60C			60

4.2.4 Varying Cobalt Contents

In this section, 4 gels were prepared by adding different amounts of $CoSO_4$ with molar ratios of Si:Co ranging from 0.1 to 0.3. For all samples, mixture solution of HMDSO in n-heptane/ethanol was used for ISE/SM at 50°C. The overview of the parameters for this section is shown in Figure 4.7 and the preparation conditions is given in Table 4.4.

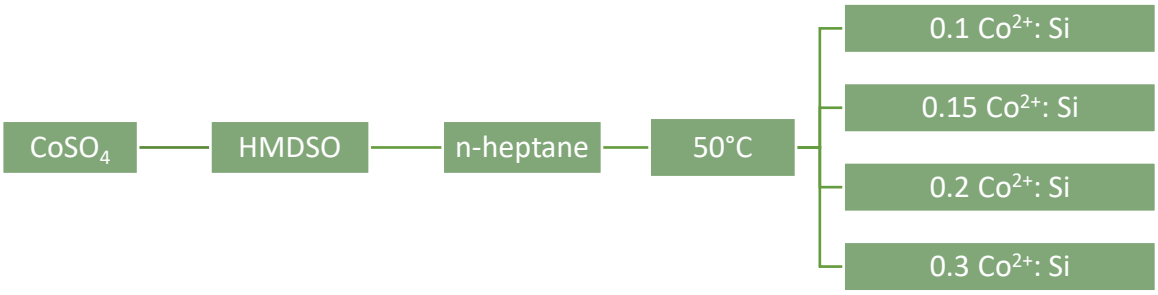

Fig. 4.7 Overview of the synthesis parameters of Co- Silica gel by varying cobalt loading

Table 4.4 Synthesis parameters including type of cobalt precursor, molar ratio of reagents used and cobalt loadings

Sample Name	**Cobalt Precursor**	**Molar ratio Si: H_2O: HMDSO: EtOH**	**Molar ratio Si:Co added**
0.1Co	$CoSO_4$	1: 40: 14: 21	0.1
0.15Co			0.15
0.2Co			0.2
0.3Co			0.3

4.3 Characterisation

Candidates were chosen based on the physical properties of the silica aerogel samples. A good candidate should have an amorphous structure with a surface area above 400 cm^2/g. Powder X-ray diffraction (XRD) was used as a tool to rule out samples that contained crystalline phases. The selected samples were then further investigated by nitrogen adsorption/desorption isotherm measurement, inductively coupled plasma mass spectrometry (ICP-MS) and x-ray absorption spectroscopy (XAS).

4.3.1 Powder X-ray Diffraction

The samples were characterised by XRD to exclude the samples with unwanted crystalline phases. The instrument used was a Bruker D8 A25 DaVinci X-ray Diffractometer with CuKα radiation and LynxEye^{TM} detector. Powdered samples were prepared on quartz sample holders for analysis. All samples were run with the program that using a divergence slit with a constant 6 mm opening and a step size of 0.013°. Data were collected from 10° to 75° 2θ for 30 minutes.

XRD was used to characterize all samples in order to exclude any samples that with unwanted crystalline phases in the gel structure. These phases can be identified by the presence of reflection signals in the XRD diffractograms. Any crystalline phases in the samples is attributed to the formation or introduction of impurities in the gel matrix during synthesis.

4.3.2 Nitrogen Adsorption and Desorption Isotherms

A Tristar 3000 surface area and porosity analyser was used for the BET and BJH analysis. The samples (0.07-0.09 g) were degassed under vacuum at 250°C for 24h. Specific surface areas were calculated from BET model on the adsorption isotherm and pore sizes were calculated from BJH equation on the adsorption isotherm. In this work, nitrogen adsorption and desorption isotherm were used to determine the specific surface area and pore size.

4.3.3 Inductive Coupled Plasma Mass Spectrometry

Sample preparation was required prior to analysis. 20-40 mg of sample was transferred to a clean vessel that was rinsed with MQ-water. Sample was then digested by addition of concentrated hydrofluoric (HF, 0.5g) and concentrated nitric acid (HNO_3, 1.5 mL). The decomposed samples were transferred to a larger Teflon container and were diluted with deionized water until a weight of 215-220g were reached. Diluted sample was transferred to a Teflon tube which was also rinsed with MQ-water to remove impurities. Three blank solution was prepared to eliminate background noise. The analysis was carried by Syverin Lierhagen at NTNU using ELEMENT 2 ICP-MS. In this project, ICP-MS was used to calculate cobalt loading.

4.3.4 X-ray Absorption Spectroscopy

X-ray Absorption Spectroscopy data was collected at the Balder beamline at the MAX IV synchrotron. The multibunch filling mode of the synchrotron was used with a current of 250mA. The beamline is positioned at wiggler with a double crystal monochromator, Si (111) for EXAFS data collection. The XAS data were recorded in transmission mode. The data was collected at the Co K-edge (7709 eV). The incident beam (I_0) and transmitted beam (I_t) intensities were detected in ion chambers I_0 (30 cm) filled with bar of N_2 , and ion chambers I_t (30 cm) filled with 400 mbar of Ar and 2.1bar of N_2. Samples powder were placed in aluminium sample holders and held in place with Kapton® tape. Reference compounds, Cobalt foil, CoO, Co_3O_4 and $Co(OH)_2$, were diluted in boron nitride for optimum absorption. The XAS at the Co K-edge was measured as a fly scan with 4095 points from 7600eV to 8600eV with 0.01 seconds per point. The data collection was carried by PhD candidate Karsten Granlund Kirste (IKJ).

Data Analysis

XAS data were reduce with Athena software from the IFEFFIT package.[78] The data energy were calibrated with a cobalt reference foil (7709 eV) and were corrected by setting E_0 to 0.5 of the normalized μ(E). XAS data was collected for as prepared, annealed and calcined sample, as well as reference compounds, cobalt foil, CoO, Co_3O_4, $Co(OH)_2$. Several scans for the same sample were merged in order to improve the signal-to-noise ratio. Deglitching and truncating were also preformed, if necessary, to remove glitches and noise from the measurements. The normalization range for XANES was 30 eV-150 eV and for EXAFS was 150 eV to the end of the spectrum.

The reduced data were then analysed by DL_EXCURVE software. (ref) The program was used to curve fit the experimental χ (k) to the theoretical χ (k) by applying the curve wave theory and calculated the backscattering amplitude and the ab initio phase-shift for the expected neighbouring atoms. k^3 weighting was used for all samples. [79]

Reference compounds were first refined to obtain the amplitude reduction factor (AFAC) by keeping the known parameter, coordination number (N), constant and refining distance (R), fermi energy (E_F) and the Debye- Waller factor ($2\sigma^2$). Then, AFAC of reference compounds was then refined and transferred to the EXAFS scans of unknown samples for analysis. The parameters, N, R, E_F and $2\sigma^2$ were refined for the unknown samples while keeping the AFAC transferred from the reference constant.

In this work, XAS is used to analyse the local environment of the Co species in silica aerogel to determine whether the cations are successfully incorporated into single site.

4.4 Catalytic Reaction

Different reactions were performed to test the catalytic performance of samples on selective catalytic reduction with hydrocarbons, propane oxidation and methanol to hydrocarbon reaction.

4.4.1 Hydrocarbons Selective Catalytic Reduction (HC-SCR)

The experimental setup for the HC-SCR testing shown in Figure 4.8 was used. Gas bottles were coupled with a mass flow controller (MFC) and were connected to a tube oven. The MFC was controlled by the computer to obtain the right mix of reaction gas flowing into the reactor. The outlet was connected to a NO/NOx analyzer to measure the concentration of nitrogen monoxides (NO). A mixture of gas containing NO (2000ppm), propene (1200ppm), oxygen (2%) and argon was used as the carrier gas.

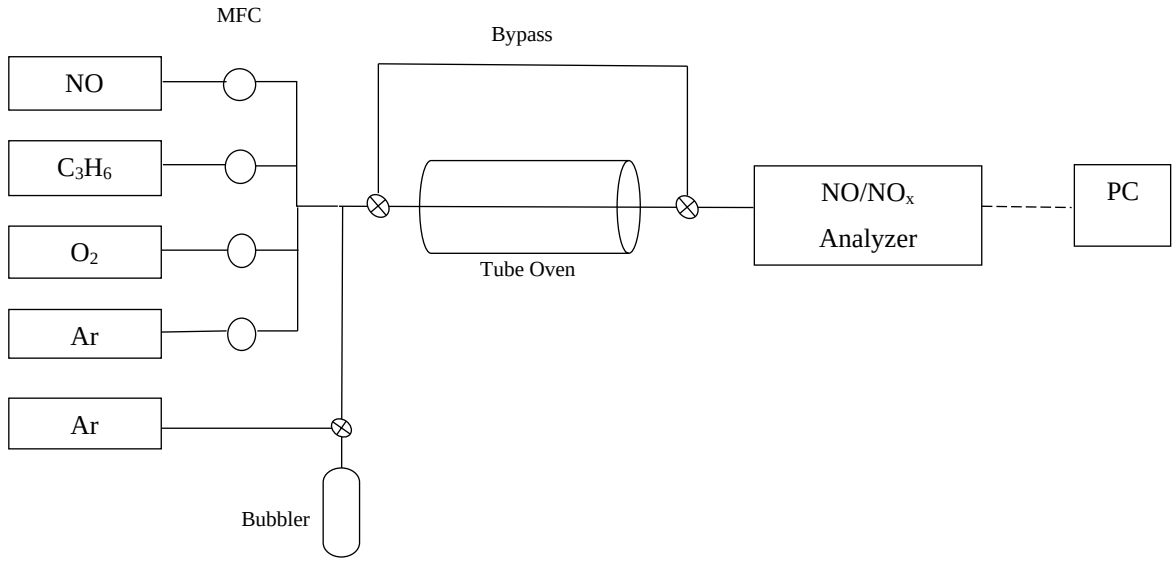

Fig. 4.8 Experimental setup of HC-SCR catalytic testing

15mg of sample was weighed out and was placed in the reactor tube. Quartz wool was used to keep the sample in place while allowing gas to flow freely through the sample. The sample was heated up to 500°C in argon (5 mL/min) overnight in the tube oven. The sample was then activated in oxygen (2%) in argon for 1h at 500°C with a gas feed of 30mL/min. The reaction begun at 500°C and ended at 275°C. Measurements were taken at every 25°C increments, each

temperature being held for 30 minutes. The gas feed containing NO (2000ppm), propene (1200 ppm), oxygen (20000 ppm) balanced in argon passed through the sample to measure the conversion of NO for 20 minutes. Bypass measurements were performed at 500°C, 400°C and 275°C by switching the gas feed to the by-pass line for 10 minutes. The NO conversion was then calculated by the formula in Equation 15:

$$Conversion\% = \frac{NO_{[bypass]} - NO_{[reactor]}}{NO_{[bypsss]}} \quad (15)$$

4.4.2 Propene Oxidation

The experimental setup for the propene oxidation was shown in Figure 4.9. Gas bottles were coupled with a mass flow controller (MFC) and were connected to a tube furnace. The outlet was connected to a FT-IR to measure the change in the propene concentration. A mixture of gas containing propene (3000 ppm), oxygen (2%) and argon was used as the carrier gas.

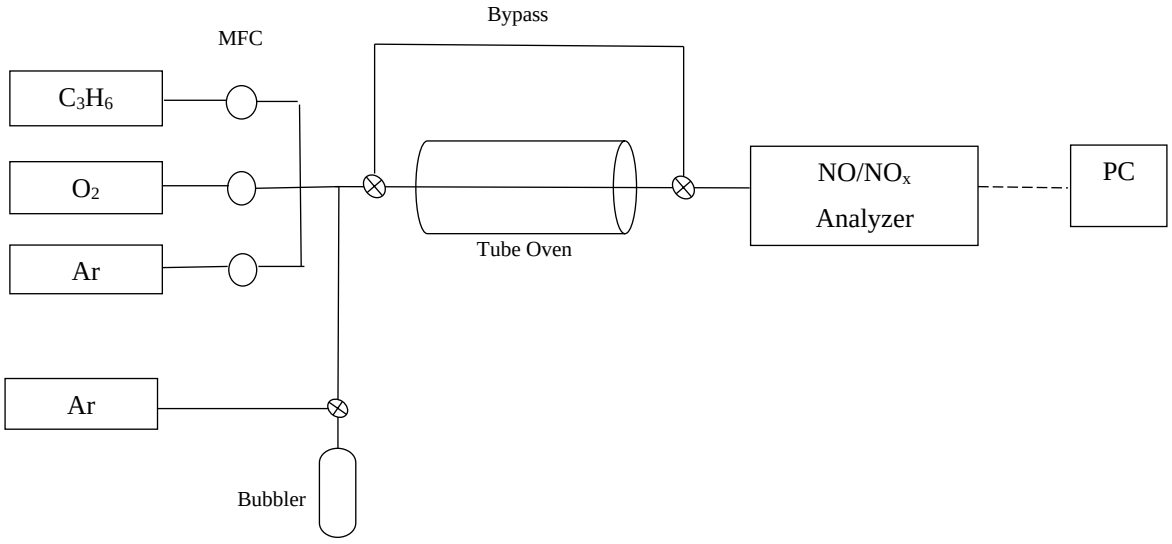

Fig. 4.9 Experimental setup of HC-SCR catalytic testing

15mg of sample was weighed out and was placed in the reactor tube. Quartz wool was used to keep the sample in place. The sample was heated up to 450°C in argon (5 mL/min) overnight in a tube oven. The sample was then activated in oxygen (2%) in argon for 40 minutes at 450°C

with a gas feed of 20mL/min. The reactor was then cooled down to 250°C. For catalytic testing, the reaction begun at 250°C and ended at 450°C. Measurements were taken at every 50°C increments, each temperature was being held for 45minutes. The gas feed containing propene (3000 ppm), oxygen (1200 ppm) balanced in argon passed through the sample to measure the concentration of propene for 35 minutes. Bypass measurements were performed at each increment by switching the gas feed to the by-pass line for 10 minutes. The propene conversion was then calculated by the formula in Equation 16:

$$Conversion\% = \frac{C_3H_{6[bypass]} - C_3H_{6[reactor]}}{C_3H_{6[bypsss]}} \quad (16)$$

4.4.3 Methanol to Hydrocarbon (MTH)

Sample was sieved to obtain a particle size of 212-425 µm. 10-15mg of sample was transferred to a porous ceramic cup. The surface of the sample was smoothed in order to obtain a good signal for diffuse reflectance infrared fourier transform spectroscopy (DRIFTS) measurement. The cup was placed in the DRIFTS cell and heated to 500℃ at 5℃/min in synthetic air/ helium. The sample was dehydrated at 500 ℃ for 1 hour before cooling down to 400℃ for catalytic testing.

At 400℃, the MTH reaction was carried out by flushing helium into a bubble filled with methanol to obtain WHSV of 1.8 -7.0$g_{MeOH}/(g_{cat} \cdot h^{-1})$, and subsequently over the sample. IR measurements were performed continuously during the reaction using a LN-MCT detector to obtain IR spectra. The exhaust from the DRIFTS cell was then fed to a gas chromatography–mass spectrometry (GC-MS) for identification and quantification of the products. Injections to GC/MS were performed every 30 minutes. The reaction was stopped when a low conversion of methanol was observed. The DRIFTS cell was the cooled down to room temperature while continuously feeding air/helium through the cell.

5 RESULT

5.1 Observations

5.1.1 Varying Cobalt Precursors and Silylation Agents

During the preparation, cobalt precursors were added to the sol and led to colour changes. The sol changed from colourless to pink after the addition of $CoSO_4$, $Co(NO_3)_2$ and $CoCl_2$, and the changed to orange after addition of $[Co(NH_3)_6]Cl_3$, (Figure 5.1)

Figure 5.1. Picture was taken after aging and before surface modification. *(left)* S(II)-H: Gel prepared using CoSO4 as cobalt precursor. *(right)* A(III)-H: Gel prepared using $[Co(NH_3)_6]Cl_3$ as cobalt precursor.

After aging, the gels were soaked in a surface modifying solution containing silylation agent (TMCS or HMDSO) and n-heptane/ ethanol. During surface modification, pore water was expelled from the gel. After surface modification was completed, two immiscible layers of solutions formed. The top layer was the colourless organic layer containing silylation agent and n-heptane/ethanol. The bottom layer was the aqueous layer, where the colour changed due to the extraction of cobalt species from the gel matrix. In beakers containing TMCS, the aqueous layer was coloured blue. It indicated the formation of tetrachloridocobaltate (II) ion,

$[CoCl4]^{2-}$. A higher concentration of TMCS showed a higher formation rate of $[CoCl4]^{2-}$. In beakers containing only HMDSO, the aqueous layer was pink, indicating the presence of $[Co(H_2O)_6]^{2+}$ species. (Figure 5.2)

Figure 5.2. Pictures were taken 10 minutes after gel immersed in surface modifying solutions. *(left)* S(II)-T: The gel immersed in a solution containing TMCS and n-heptane/EtOH, *(middle)* S(II)-T/H: The gel immersed in a solution containing mixture of TMCS/HMDSO and n-heptane/EtOH *(right*) S(II)-H: The gel immersed in a solution containing HMSDO and n-heptane/EtOH

Gels that immersed in a solution containing TMCS changed from a pink to blue. C(II)-T, N(II)-T and S(II)-T showed a core-shell structure, made up with light blue outer layer and dark blue core, where C(II)-T/H, N(II)-T/H and S(II)-T/H were complete dark blue. A higher concentration of TMCS led to more rapid extraction of cobalt species from the gel. C(II)-H, N(II)-H and S(II)-H remained pink after surface modification. (Figure 5.3)

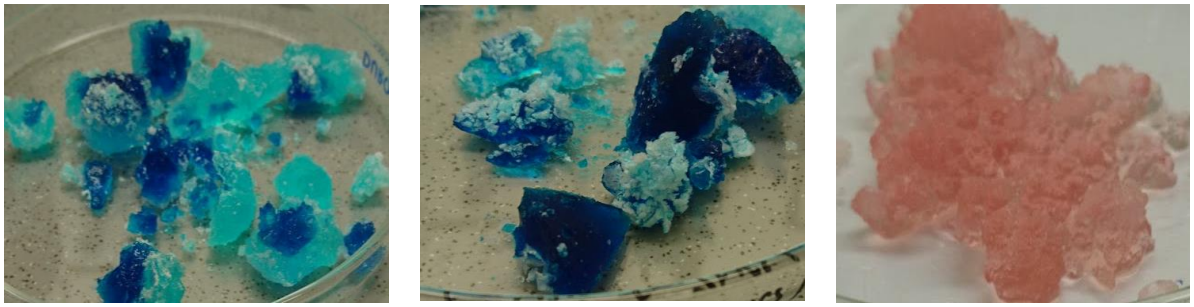

Figure 5.3, Gels surface modified for 24 hours. *(left)* S(II)-T: Gel immersed in a solution containing TMCS and n-heptane/EtOH, *(middle)* S(II)-T/H: The gel immersed in a solution containing TMCS/HMDSO and n-heptane/EtOH *(right)* S(II)-H: The gel immersed in a solution containing HMSDO and n-heptane/EtOH

After drying, samples were mortared into powder. The hydrophobicity of samples was tested by dropping a droplet of water on the powder sample. Samples that surface modified by TMCS were shown to be hydrophobic as the droplet suspended on the powder. Samples that surface modified by HMDSO were not hydrophobic as the water spread. (Figure 5.4)

Figure. 5.4. Pictures show hydrophobicity of samples. *(left)* S(II)-T *(middle)* S(II)-T/H *(right)* S(II)-H

5.1.2 Varying Gelation pH Values

Gelation time of the gel is affected by the pH of the sol. By increasing pH from 4 to 6.5, a decrease in gelation time was observed, due to the higher condensation rate between silica particles at high pH. (Table 5.1) Colour of the sol was pink prior addition of the base catalyst. When NH_4OH was added, blue coagula were formed simultaneously (Figure 5.5), which indicated the formation of $[Co(H_2O)_4(OH)_2]$ complexes. (Equation 17) After continuous stirring, $[Co(H_2O)_4(OH)_2]$ complex redissolved. At pH 4, all $[Co(H_2O)_4(OH)_2]$ complex redissolved before gelation occurred. For pH higher than 5, the sol gelled before the blue coagula redissolved.

$$[Co(H_2O)_6]_2+ \ NH_4OH \longrightarrow [Co(H_2O)_4(OH)_2] \qquad (17)$$

Table 5.1. Table showing measured gelation time with corresponding pH value of the selected sol: N(II)-H_pH4, N(II)-H _pH5 and N(II)-H _pH6.5

Sample Name	pH	Gelation Time
N(II)-H_pH4	4	>6 hours
N(II)-H_pH5	5	30 minutes
N(II)-H_pH6.5	6.5	<10 minutes

Figure. 5.5 Addition of Ammonium hydroxide to sol led to the formation of blue coagula (green circle) in the gel.

5.1.3 Varying Exchange Solvents and Temperature

In section 5.1.1, the gels prepared with HMDSO were found to be hydrophilic or expressed low hydrophobicity. Therefore, the temperature for surface modification was raised and different exchange solvents was used to increase the reactivity of HMDSO and to improve hydrophobicity of the final gels. All as prepared samples are pink after drying. For samples hydrophobized at 60°C, the colour of powder changed to black after calcination, which indicates the formation of cobalt oxides. (Figure 5.6)

Figure. 5.6. Colour of S_C_6_60C powder sample hydrophobized at 60°C in modifying solvents of HMDSO and n-heptane/ EtOH: as prepared (*left*), annealed (*middle*) and calcined (*right*).

5.1.4 Varying Cobalt Content

Different amount of cobalt precursor added during synthesis also affect the physical properties of the final products. As prepared samples with lower cobalt content, 0.1Co and 0.15Co, are shown as pink while as prepared samples with higher cobalt content, 0.2Co and 0.3Co, are purple. (Figure 5.7)

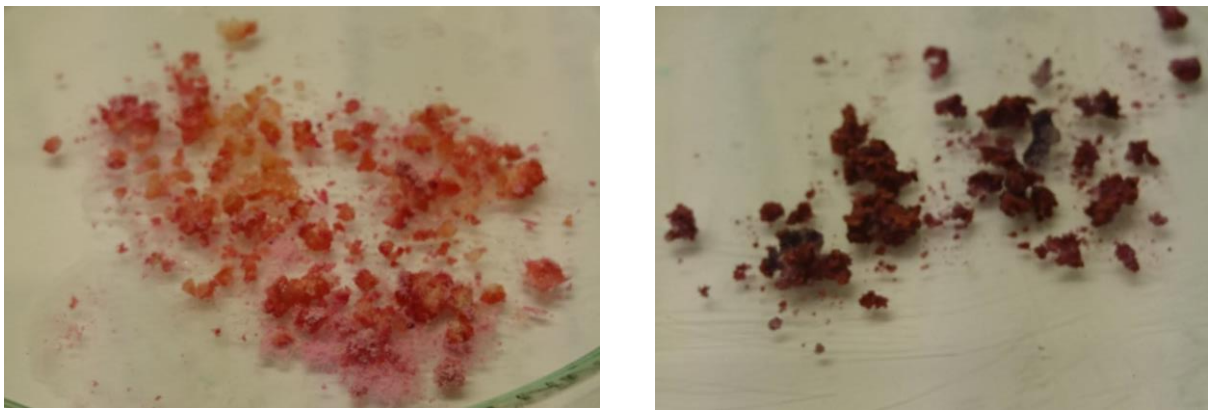

Figure. 5.7. Colour of 0.1Co as prepared sample (*left*) and 0.3Co as prepared sample (*right*).

5.2 X-ray Diffractogram

XRD was used to characterize all samples in order to exclude any samples that with unwanted crystalline phases in the gel structure. Only samples with amorphous structure, before and after heat treatment at 450℃ and 700℃, are chosen for further investigations.

5.2.1 Varying Cobalt Precursors and Silylation Agents

XRD diffractograms of as prepared samples using different Co precursors and silylation agents are shown in Figure 5.8-5.10. All samples synthesised using $CoCl_2 \cdot 6H_2O$ as cobalt precursor show reflection signals in the diffractograms. These signals indicate the presence of crystalline phase in samples. Crystalline phases, which are identified as $CoCl_2$ and SiO_2, are also found in samples N(II)-T, N(II)-T/H, A(III)-H. Diffractograms of samples N(II)-H and all samples using $CoSO_4$ as Co precursor is found to be amorphous. XRD result is summarized in Table 5.2.

Table 5.2. Summary of the result of XRD analysis showing if the as prepared samples are amorphous. Sample with colour-coded in green indicates the gel is amorphous before heat treatment.

Sample Name	**Cobalt Precursor/ Silylation agent**	**Amorphous**
N(II)-T	$Co(NO_3)_2 \cdot 6H_2O$/ TMCS	No
N(II)-T/H	$Co(NO_3)_2 \cdot 6H_2O$/ TMCS, HMDSO	No
N(II)-H	$Co(NO_3)_2 \cdot 6H_2O$/ HMDSO	Yes
S(II)-T	$CoSO_4$/ TMCS	Yes
S(II)-T/H	$CoSO_4$/ TMCS, HMDSO	Yes
S(II)-H	$CoSO_4$/ HMDSO	Yes
C(II)-T	$CoCl_2 \cdot 6H_2O$/ TMCS	No
C(II)-T/H	$CoCl_2 \cdot 6H_2O$/ TMCS, HMDSO	No
C(II)-H	$CoCl_2 \cdot 6H_2O$/ HMDSO	No
A(III)-H	$[Co(NH_3)6]Cl_3$/ HMDSO	No

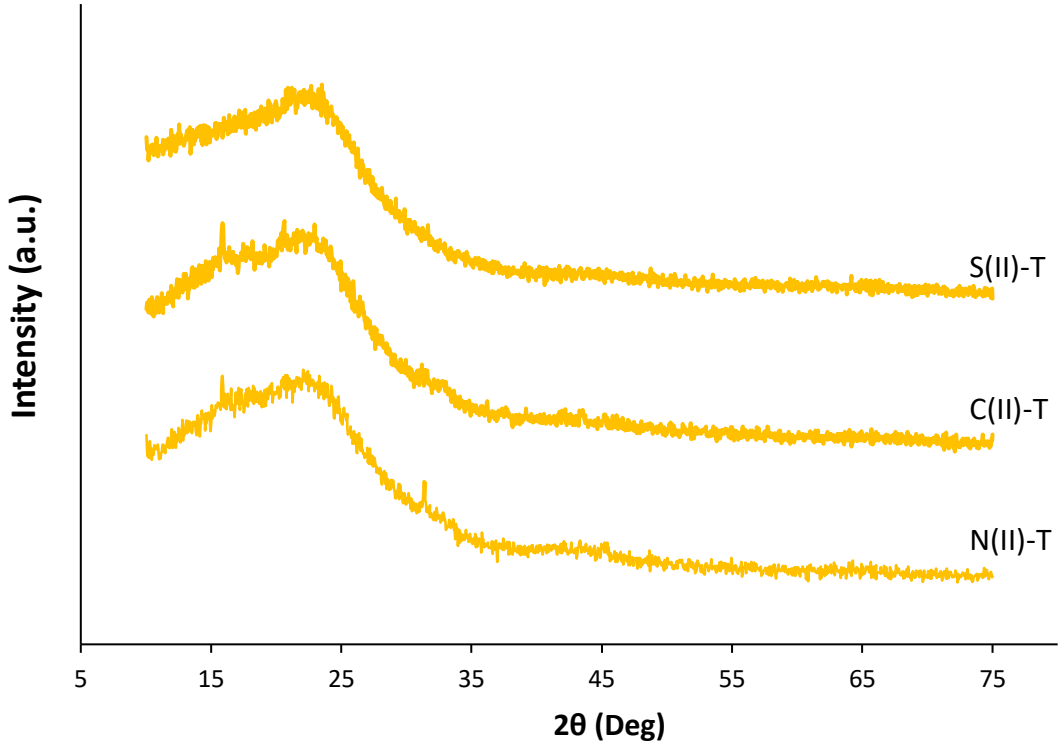

Figure. 5.8. Stacked X-ray diffraction pattern of as prepared sample of S(II)-T, C(II)-T and N(II)-T.

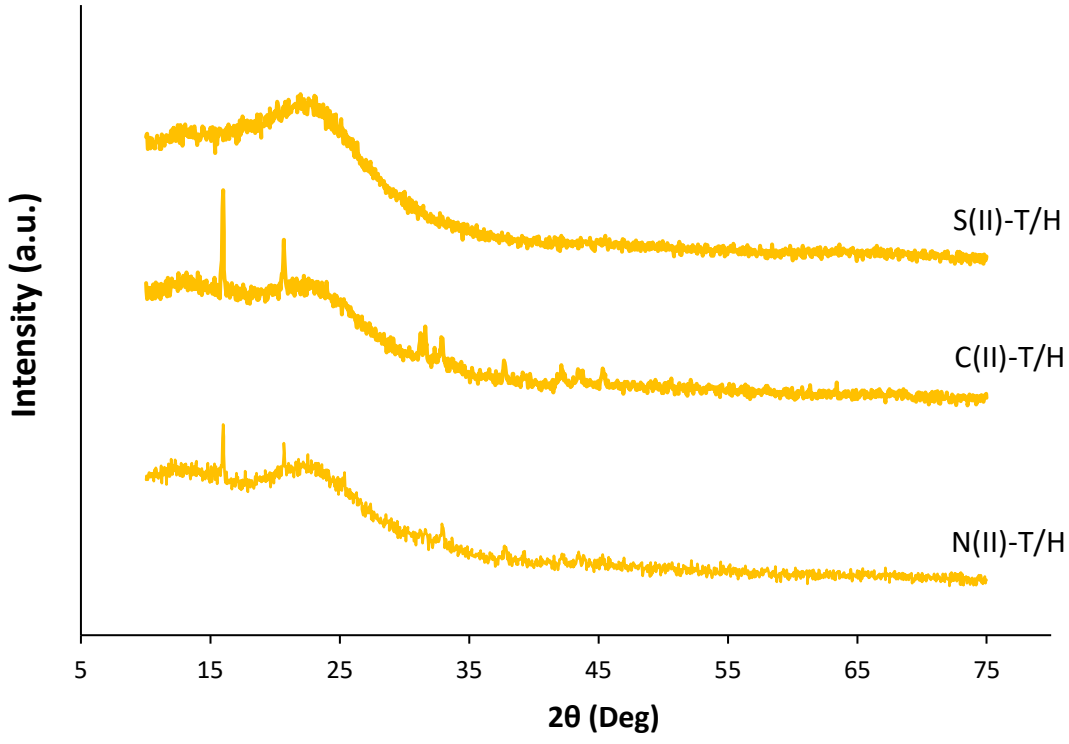

Figure. 5.9. Stacked X-ray diffraction pattern of as prepared sample of S(II)_T/H, C(II)_T/H and N(II)_T/H

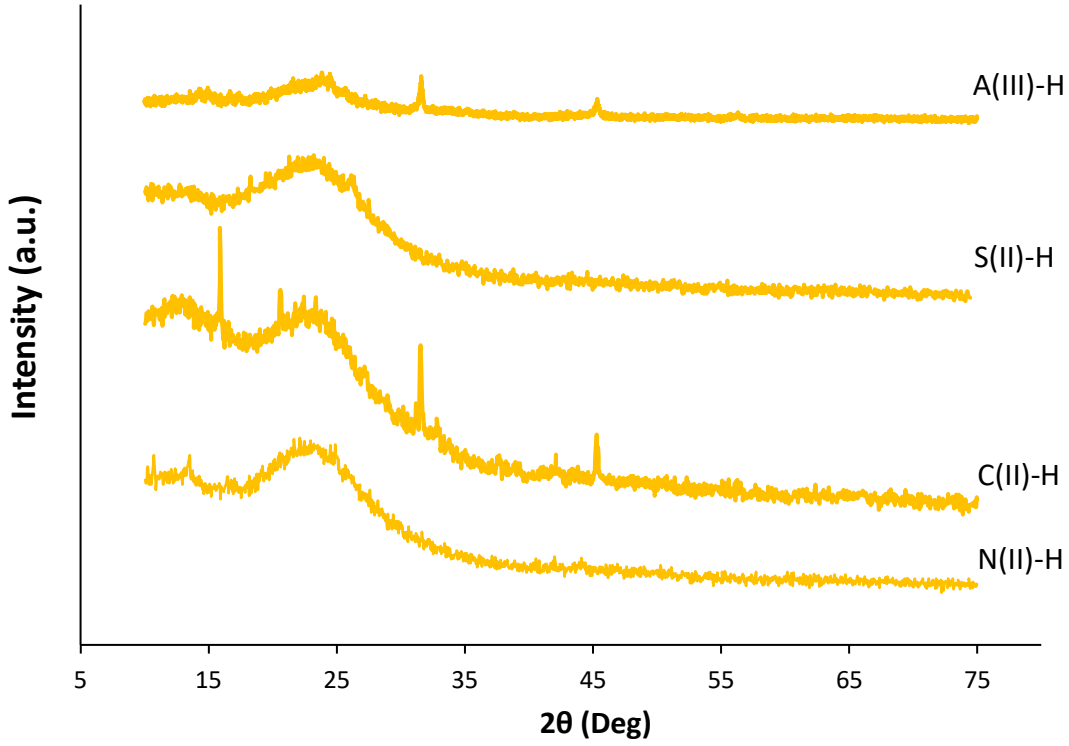

Figure. 5.10. Stacked X-ray diffraction pattern of as prepared sample of A(III)-H, S(II)-H, C(II)-H and N(II)-H

5.2.2 Varying Gelation pH Values

The XRD diffractograms of as prepared and annealed samples that synthesised at different pH are shown in Figure 5.11. The diffractograms suggested that no crystallinity was found in all samples before heat treated at 450°C (annealed). Only sample N(II)-H_pH4 was amorphous for both as prepared and annealed form. It is because all blue coagula redissolved before gelation occurred. However, for annealed N(II)-H_pH5, N(II)-H_pH5.5 and N(II)-H_pH6.5, the diffractograms show crystalline phase that attributed to the formation of cobalt oxides during heat treatment (annealed at 450°C). XRD result is summarized in Table 5.3

Table. 5.3. Summary of the result of XRD analysis showing if the as prepared and annealed (at 450°C) samples are amorphous. Sample with colour-coded in green indicates the gel is amorphous for both as prepared and annealed

Sample Name	**pH**	**Amorphous**	
		As Prepared	**Annealed**
N(II)-H_pH4	4	Yes	Yes
N(II)-H_pH5	5	Yes	No
N(II)-H_pH5.5	5.5	Yes	No
N(II)-H_pH6	6.5	Yes	No

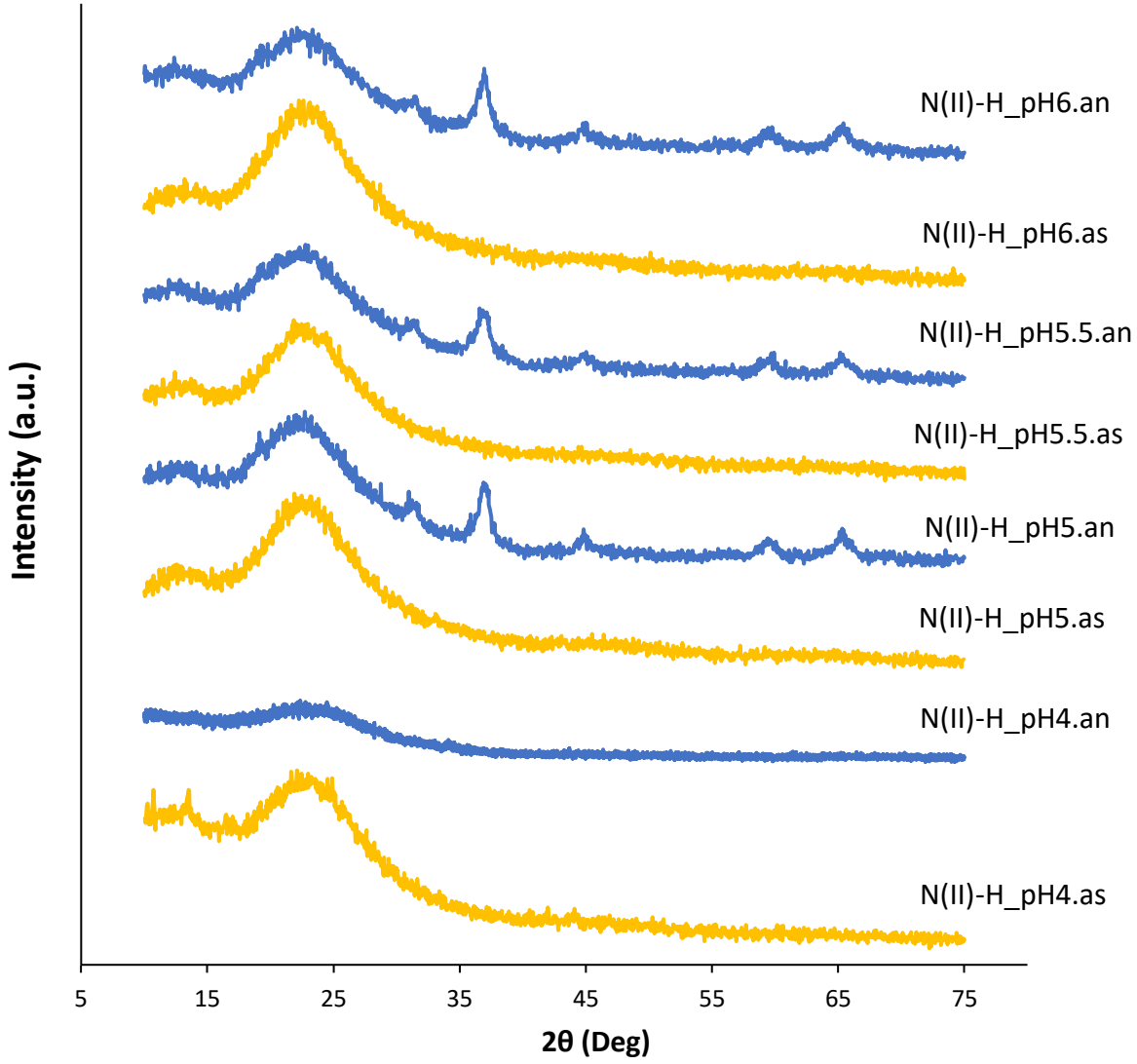

Figure 5.11. Stacked X-ray diffraction pattern of as prepared sample (yellow) and annealed sample (blue) of N(II)-H_pH4, N(II)-H_pH5, N(II)-H_pH5.5 and N(II)-H_pH6

5.2.3 Varying Exchange Solvents and Temperature

Conditions of the solvent exchange process can influence the final structure of the gel. XRD analysis was carried out on samples immersed in different exchange solvents (n-heptan and n-hexane) at temperature varying from 50°C to 60°C. XRD results is summarized in Table 5.4.

Table 5.4. Summary of the result of XRD analysis showing if the as prepared, annealed (at 450°C) and calcined (at 700°C) samples are amorphous. Sample with colour-coded in green indicates the gel is amorphous for all samples: as prepared, annealed and calcined.

Sample Name	**Cobalt Precursor**	**Temperature/ solvent**	**Amorphous**		
			As Prepared	Annealed	Calcined
N_C_7_50C	$Co(NO_3)_2 \cdot 6H_2O$	50°C / n-heptane	Yes	Yes	No
N_C_7_55C		55°C / n-heptane	Yes	Yes	No
N_C_7_60C		60°C / n-heptane	No	No	No
N_C_6_50C		50°C / n-hexane	Yes	Yes	No
N_C_6_55C		55°C / n-hexane	Yes	Yes	No
N_C_6_60C		60°C / n-hexane	Yes	No	
S_C_7_50C	$CoSO_4$	50°C / n-heptane	Yes	Yes	Yes
S_C_7_55C		55°C / n-heptane	Yes	Yes	No
S_C_7_60C		60°C / n-heptane	Yes	No	
S_C_6_50C		50°C / n-hexane	Yes	No	No
S_C_6_55C		55°C / n-hexane	No	No	No
S_C_6_60C		60°C / n-hexane	No	No	No

$N\_C_7\_50C$ and $N\_C_6\_50C$ show no indication of crystalline phases that related to the presence of cobalt oxides and other impurities in the gel matrix. (Figure 5.12) However, samples show low crystallinity after calcined at 700°C which attributed to the formation of cobalt oxides during heat treatment.

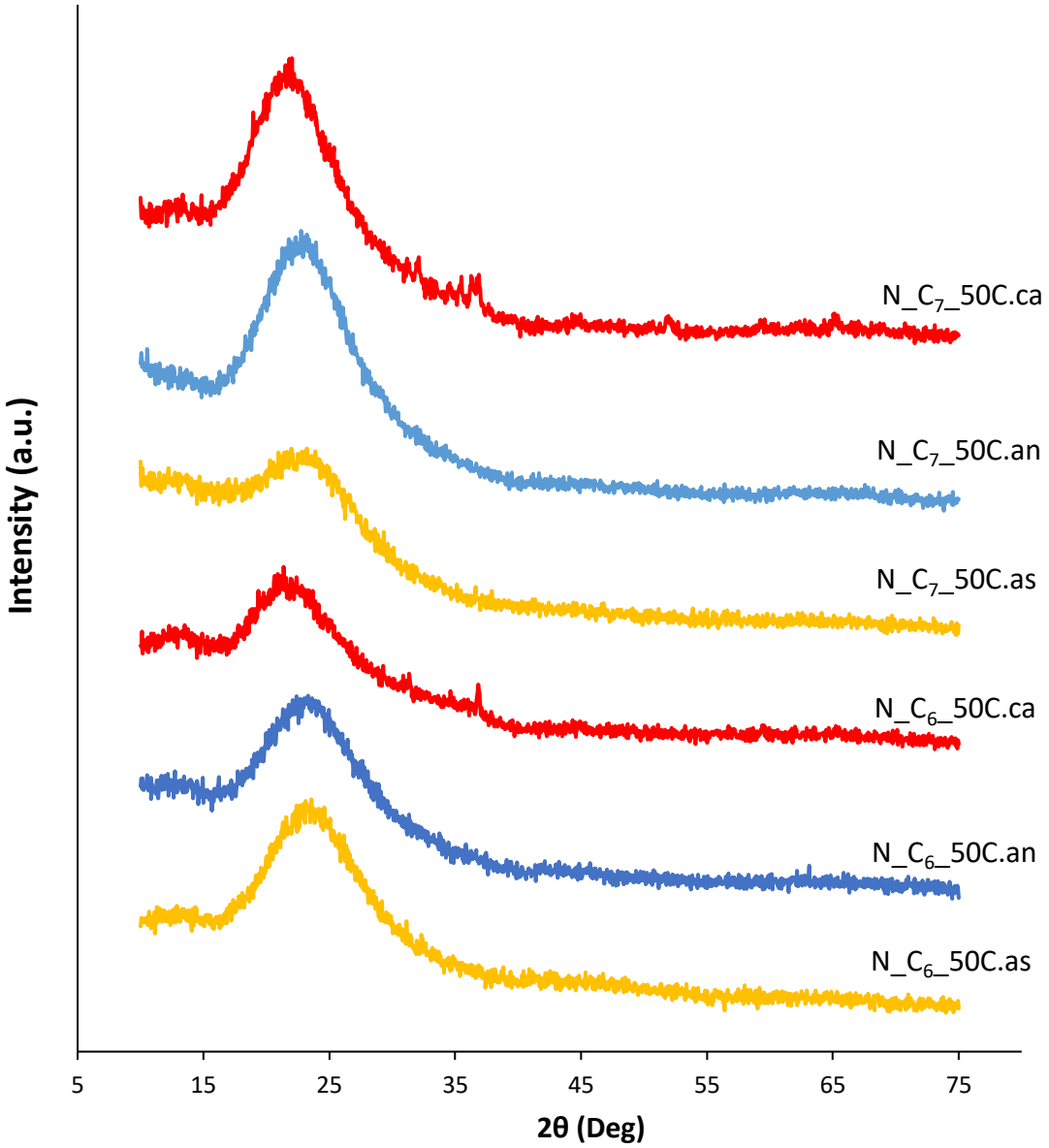

Figure. 5.12. Stacked X-ray diffractograms of $N\_C_6\_50C$ and $N\_C_7\_50C$: as prepared (yellow), annealed (blue) and calcined (red)

All gels prepared with cobalt sulphate and immersed in n-hexane shows high crystallinity after annealed and calcined. (Figure 5.13)

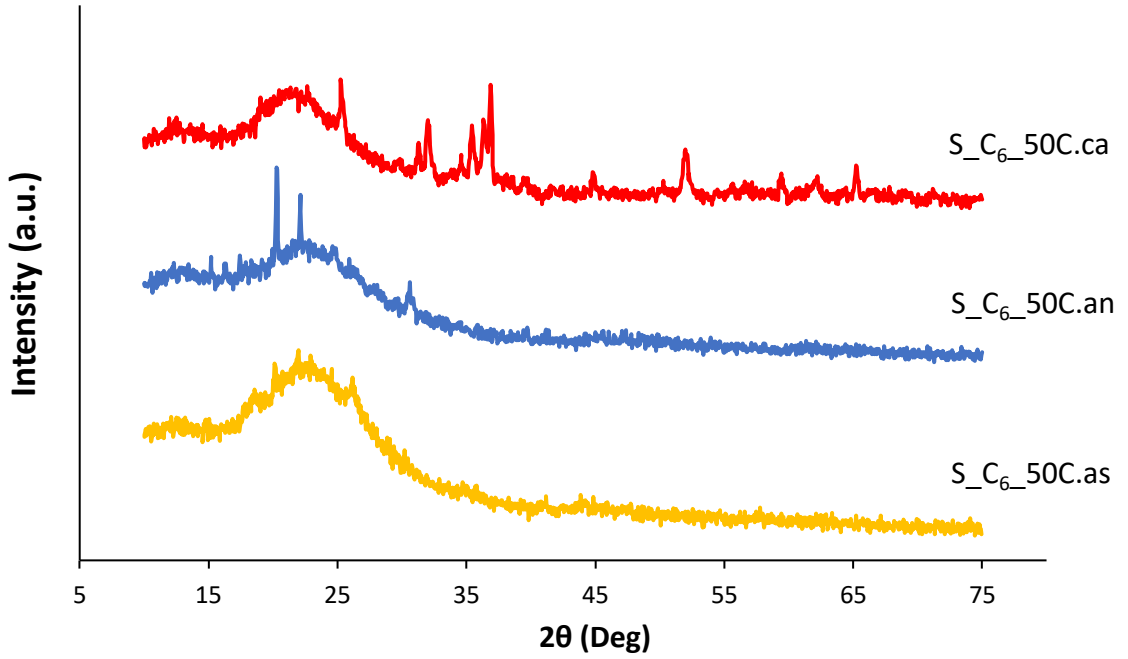

Figure. 5.13. Stacked X-ray diffractograms of S_C_6_50C: as prepared (yellow), annealed (blue) and calcined (red)

S_C_7_50C showed no crystallinity in samples before and after heat treatment (annealed at 450°C and calcined at 700°C). (Figure 5.14)

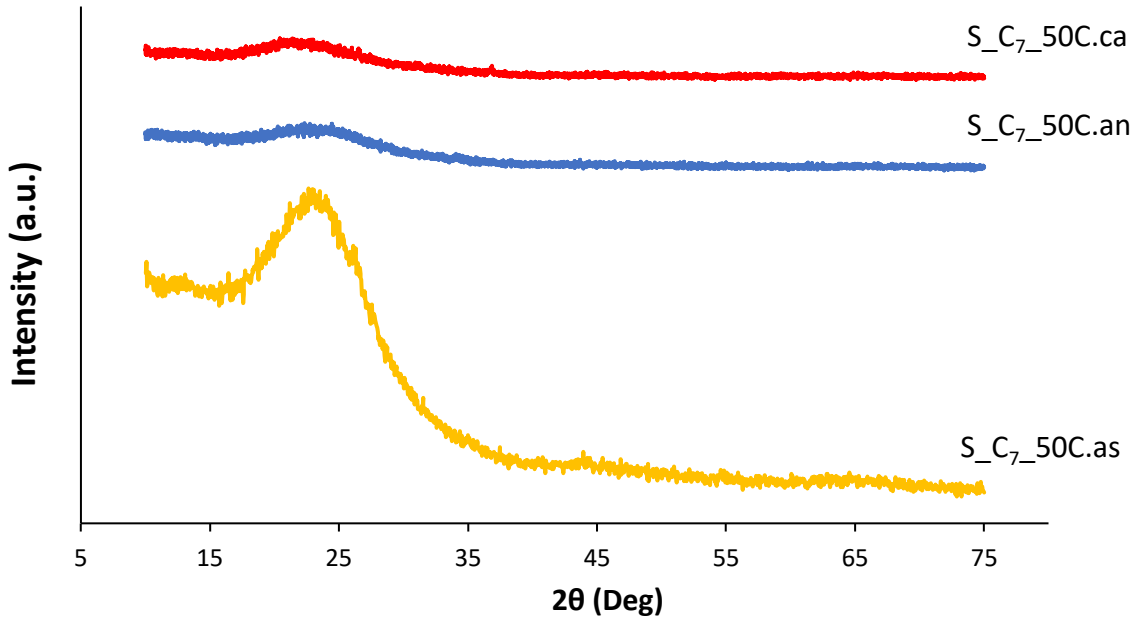

Figure. 5.14. Stacked X-ray diffractograms of S_C_7_50C: as prepared (yellow), annealed (blue) and calcined (red)

At 60°C, all gels have crystalline phases. The reflection signals detected by XRD suggest the presence of cobalt oxide in the gel matrix. (Figure 5.15) XRD diffractograms for the remaining gels are presented in Appendix B.

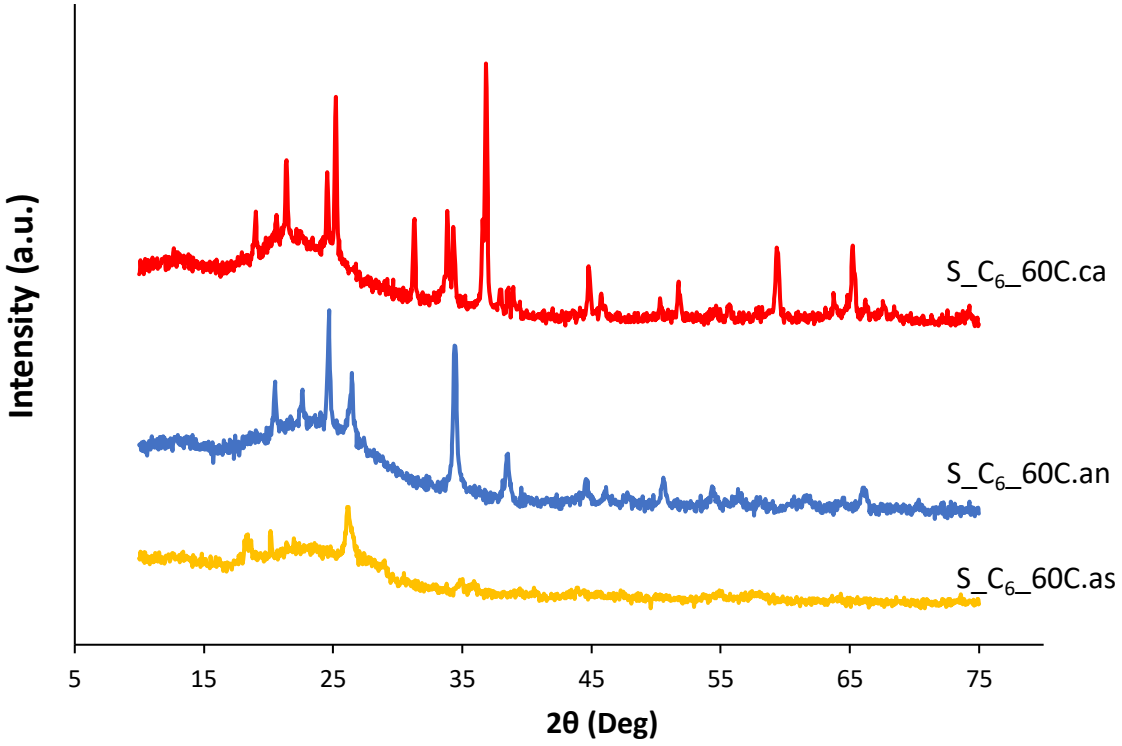

Figure. 5.15 Stacked X-ray diffractograms of S_C_6_60C: as prepared (yellow), annealed (blue) and calcined (red)

5.2.4 Varying Cobalt Contents

In this section, XRD analysis was performed on samples prepared with different amount of cobalt precursor, $CoSO_4$. Each sample was characterized as prepared and after heat treated at 450 °C (annealed) and at 700 °C (calcined). XRD results are summarized in Table 5.5.

Table. 5.5. Summary of the result of XRD analysis showing if the as prepared, annealed (at 450°C) and calcined (at 700°C) samples are amorphous. Sample with colour-coded in green indicates the gel is amorphous for all samples: as prepared, annealed and calcined.

Sample Name	**Co:Si ratio added during synthesis**	**Amorphous**		
		As Prepared	**Annealed**	**Calcined**
0.1Co	0.1	Yes	Yes	Yes
0.15Co	0.15	Yes	Yes	Yes
0.2Co	0.2	No	No	No
0.3Co	0.3	No	No	No

Samples with low cobalt content (theoretical Co:Si ratio ≤ 0.15) show a board signal in the diffractogram attributed to the amorphous structure of silica gels and no crystalline phases were detected. (Figure 5.16) Crystalline phases were detected in sample with high cobalt content (theoretical Co:Si ratio ≥ 0.2). As cobalt content in gel increases, intensity of reflection peaks in XRD diffractograms increases. (Figure 5.17) XRD diffractogram of 0.1Co is presented in Appendix B.

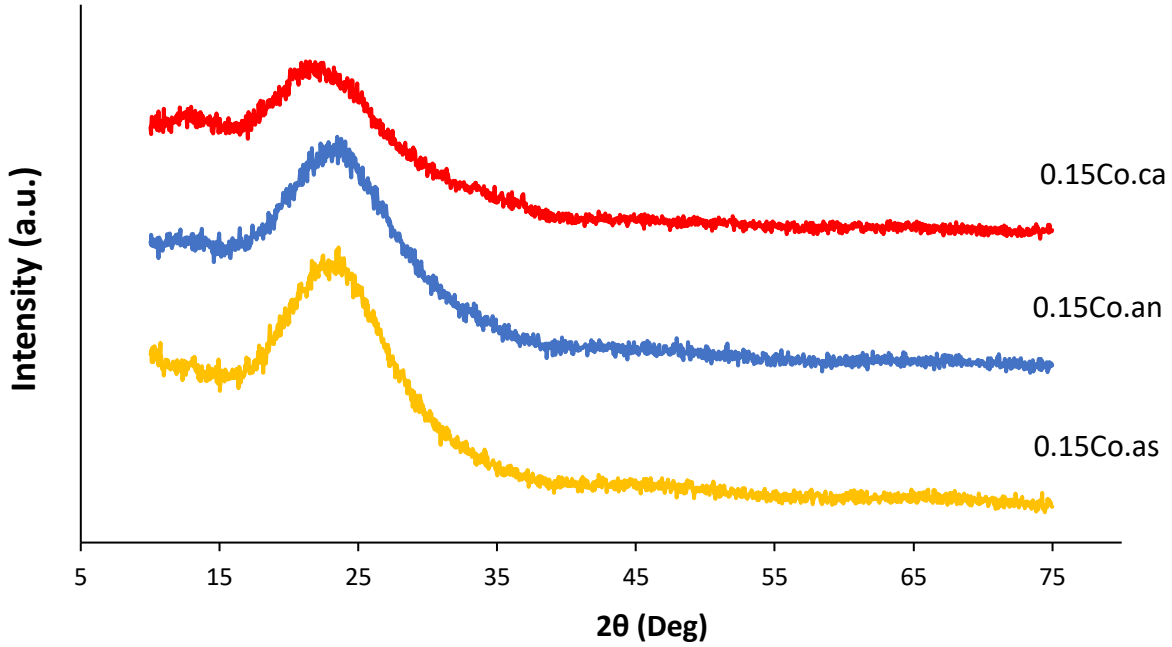

Figure. 5.16. Stacked X-ray diffractograms of 0.15Co as prepared (yellow), annealed (blue) and calcined (red)

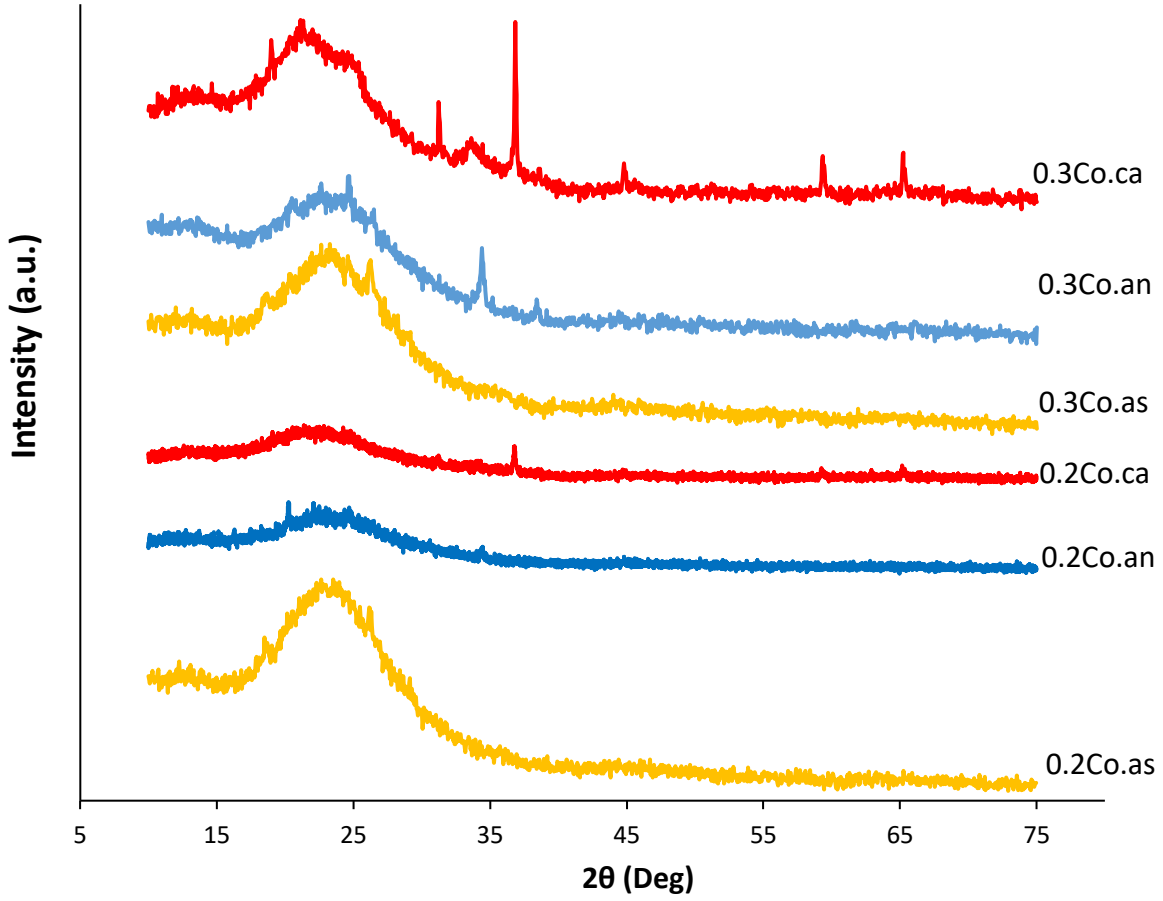

Figure. 5.17. Stacked X-ray diffractograms of 0.2Co and 0.3Co as prepared (yellow), annealed (blue) and calcined (red).

5.3 Nitrogen Adsorption and Desorption Isotherms

Only sample with no or low crystallinity were chosen for further investigation. Preparation conditions of each selected sample were summarized in Table 5.6.

Table. 5.6. Preparation conditions of sample for further investigation: surface modifying temperature, molar ratio of precursor used.

Sample Name	**Cobalt Precursor**	**Temperature (°C)**	**Molar ratio Si: H_2O: Co: TMCS: HMDSO**			
			Si	H_2O	Co	HMDSO
N(II)-H	$CoNO_3$	r.t	1	40	0.1	7
N_C_7_50C		50				
Co0.1	$CoSO_4$					
Co0.15					0.15	

For mesopores silica aerogel, a type IV isotherm with a hysteresis loop is expected. However, all selected samples show a type I isotherm with type H4 loop. (Figure 5.18 and Appendix C) It indicates the pores consist mainly micropores and small amount of mesopores. For the calcined samples, the isotherm with a hysteresis loop shows presence of small degree of mesopores and the pore distribution is slightly shifted towards larger average pore diameter (Figure 5.18 and Appendix C) This is due to the oxidation of the Si-OC_2H_5 group to Si-OH group.[66] However, there are no significant changes in the average pore size and pore volume after heat treatment. (Appendix C)

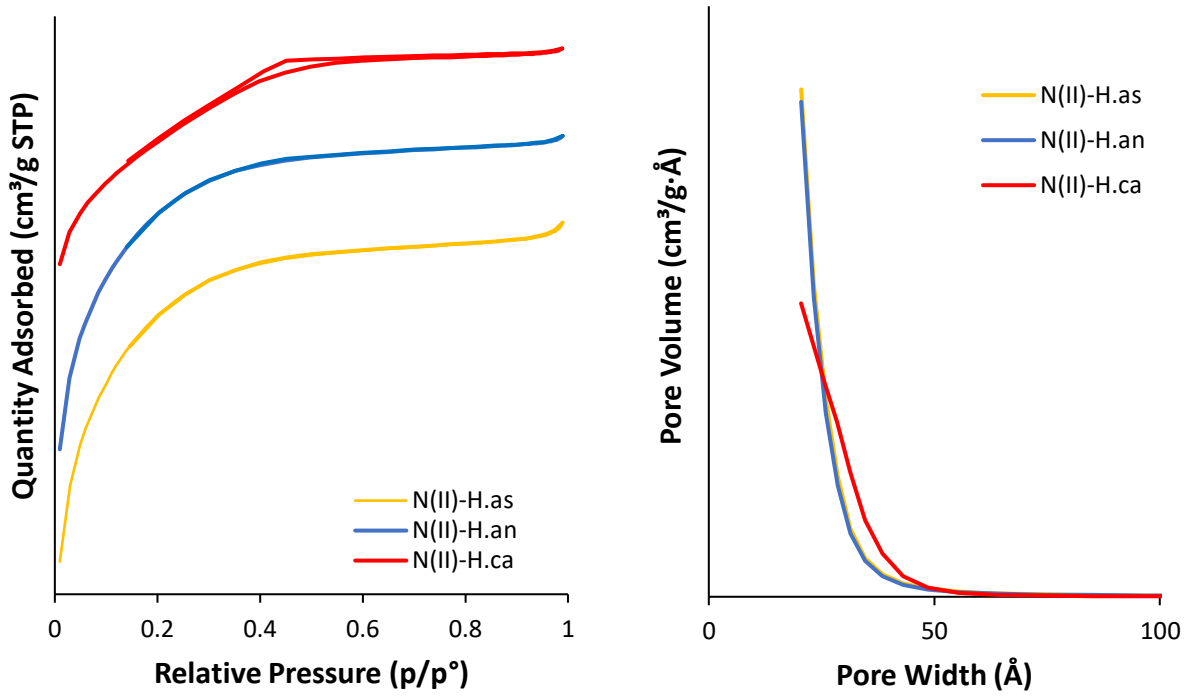

Figure. 5.18. Adsorption and desorption isotherms (*left*) and pore distribution (*right*) of N(II)-H: as prepared (yellow), annealed (blue), calcined (red).

Specific surface area of samples was calculated by BET method. No significant different of surface area are seen between as prepared and anneal sample. A decrease in surface area after calcining is seen due to the collapse of the pore structure during heat treatment. The effect of temperature on the gel structure was studied by comparing N(II)-H and N_C_7_50C. Increase in surface modification temperature, from room temperature to 50°C, did not change the surface area of the gels. (Figure 5.19) The results from nitrogen adsorption and desorption analysis are summarized in Table 5.7.

Table 5.7. BET & BJH measurement for sample with different surface modifying temperature.

Sample Name	Surface Area (m^2/g)	Pore Volume (cm^3/g)	Pore Width (Å)
N(II)-H.as	496	0.093	26.5
N(II)-H.an	468	0.090	25.5
N(II)-H.ca	206	0.088	27.2
N_C_7_50C.as	468	0.091	26.4
N_C_7_50C.an	455	0.090	25.8
N_C_7_50C.ca	223	0.085	26.6

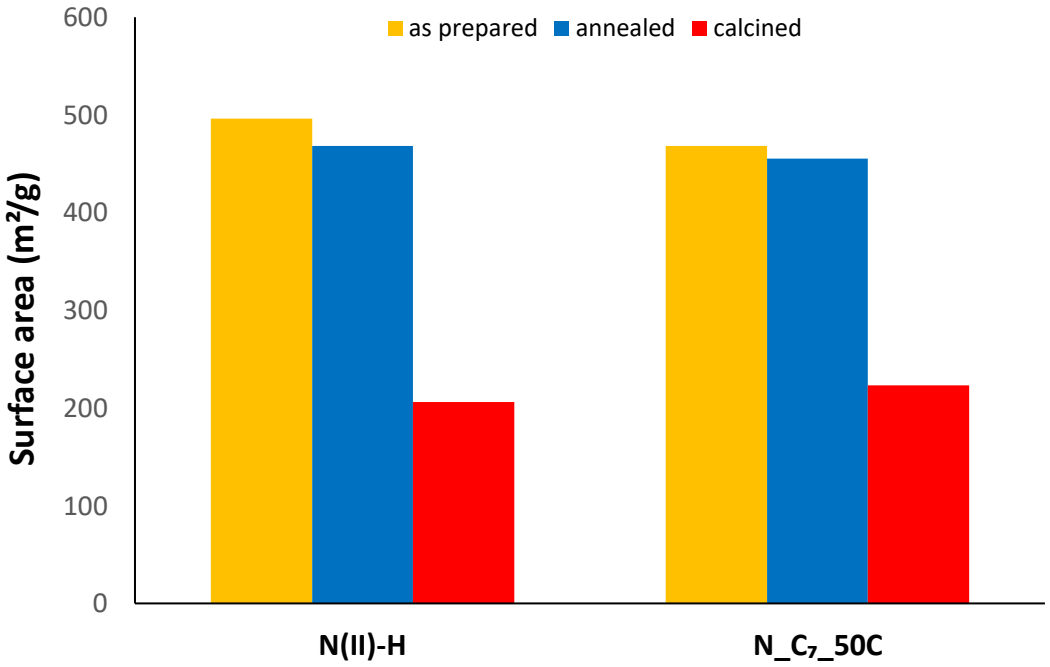

Figure. 5.19. BET surface area of samples prepared at different surface modifying temperature: as prepared (yellow), annealed (blue), calcined (red).

The effect of cobalt content on the gel structure was studied by comparing plain aerogel, 0.1Co and 0.15Co. Introduction of cobalt into silica aerogel increase total surface area of the as prepared sample. Increase in cobalt content did not have observable effects on the porosity of the gels. (Figure 5.20) However, no correlation can be drawn due to the limited studies of varying cobalt content was conduct. The results from nitrogen adsorption and desorption analysis are summarized in Table 5.8.

Table 5.8. BET & BJH measurement for sample with different cobalt content.

Sample Name	Surface Area (m^2/g)	Pore Volume (cm^3/g)	Pore Size (Å)
Plain aerogel	446	0.64	45.0
0.1Co.as	540	0.0789	26.4
0.1Co.an	541	0.0754	26.3
0.1Co.ca	292	0.0644	26.8
0.15Co.as	532	0.0986	25.9
0.15Co.an	486	0.0946	25.8
0.15Co.ca	356	0.126	28.8

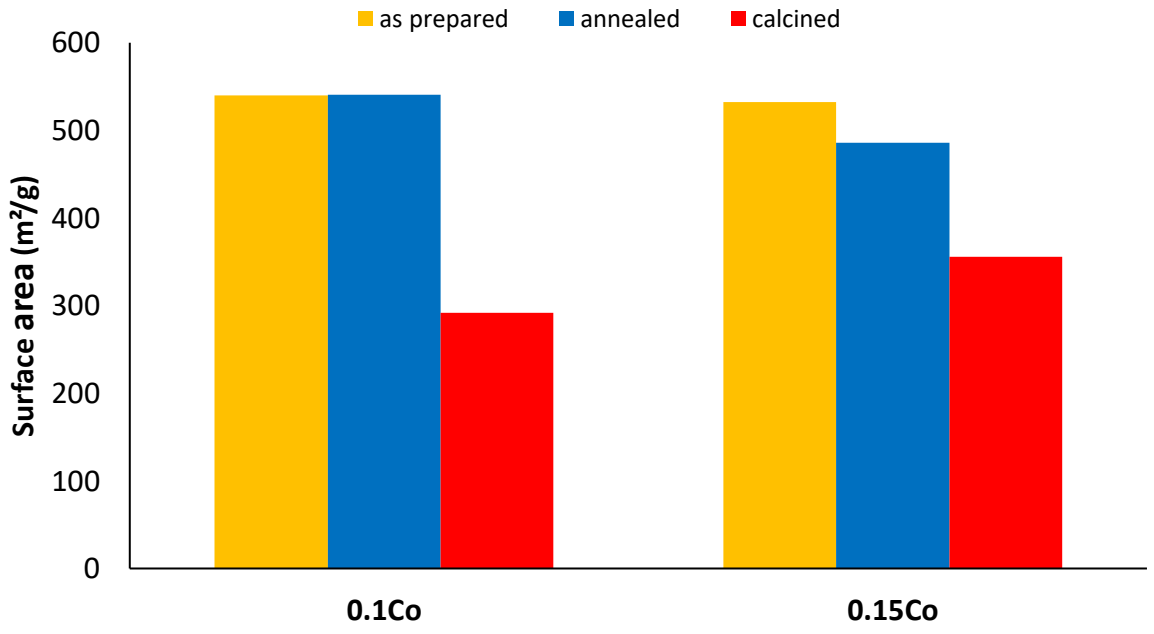

Figure. 5.20. BET surface area of samples prepared with different amount of cobalt added during synthesis: as prepared (yellow), annealed (blue), calcined (red).

5.4 Elemental Composition of Cobalt Silica Aerogel

ICP-MS analysis was performed in all as prepared samples that described in section 4.2.4. The amount of cobalt content in silica aerogel was determined from gels synthesised with different cobalt loadings. The results of cobalt uptake in wt% are shown in Figure 5.21.

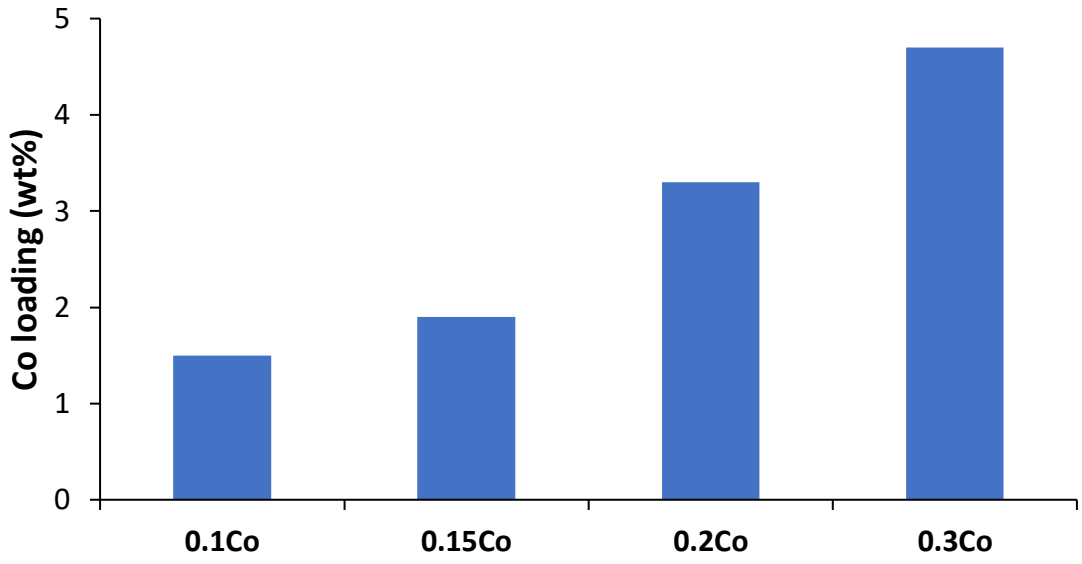

Figure. 5.21. Measured Cobalt loading in wt % of each as prepared sample

Table 5.9 summarized the theoretical and experimental cobalt composition in silica aerogels. Loss in cobalt content from gel was seen in all samples. Cobalt species was removed from the gel matrix while pore water is exchanged with organic solvent. It can be observed during preparation where water collected after solvent exchange was pink.

Table 5.9. Theoretical and experimental cobalt composition in as prepared samples that obtain from ICP-MS analysis

Sample Name	Molar Ratio Co:Si		Cobalt Loading (wt%)
	Theoretical	Experimental	
0.1Co	0.1	0.020	1.5
0.15Co	0.15	0.024	1.9
0.2Co	0.2	0.045	3.3
0.3Co	0.3	0.072	4.7

5.5 X-ray Absorption Spectroscopy

XAS analysis was performed to determine the local environment and oxidation state of cobalt species in the gel, 0.1Co and 0.15Co. For 0.1Co and 0.15Co samples, as prepared, annealed, and calcined were studied subject to ex-situ XAS analysis, as well as reference compounds. These reference compounds are cobalt foil, CoO, Co_3O_4 and $Co(OH)_2$. All measurements were collected at the cobalt K edge (7709 eV). The XAS spectra were measured by Karsten Granlund Kirste (IKJ).

5.5.1 XANES on cobalt silica aerogel

Stacked plots of normalized XANES and the first derivative normalized XANES of 0.1Co and 0.15Co samples as well as the reference compounds are shown it Figure 5.22 and Appendix D. Spectra of the reference compounds are coloured in blue and the samples are coloured in black. All E_0 values were corrected with respected to cobalt foil at 7709eV.

In the XANES region, information about site symmetry and oxidation state of cobalt in the gel can be obtained by comparing the samples with the reference compounds. In Figure 5.22, there is no resemblance can be seen in the normalized derivatives XANES between samples and the reference compounds. This suggests that the local environment of cobalt species in the gel is different to the local environment of cobalt species in CoO, Co_3O_4 and $Co(OH)_2$. However, some resemblances can also be seen between samples, 0.1Co and 0.15Co, suggesting that the local environment of cobalt is similar in both samples. It also shows some resemblances between as prepared and annealed samples, where less resemblances with the calcined sample is shown. It may suggest that the environment of cobalt is stable before 400°C. but changes between 400- 700°C.

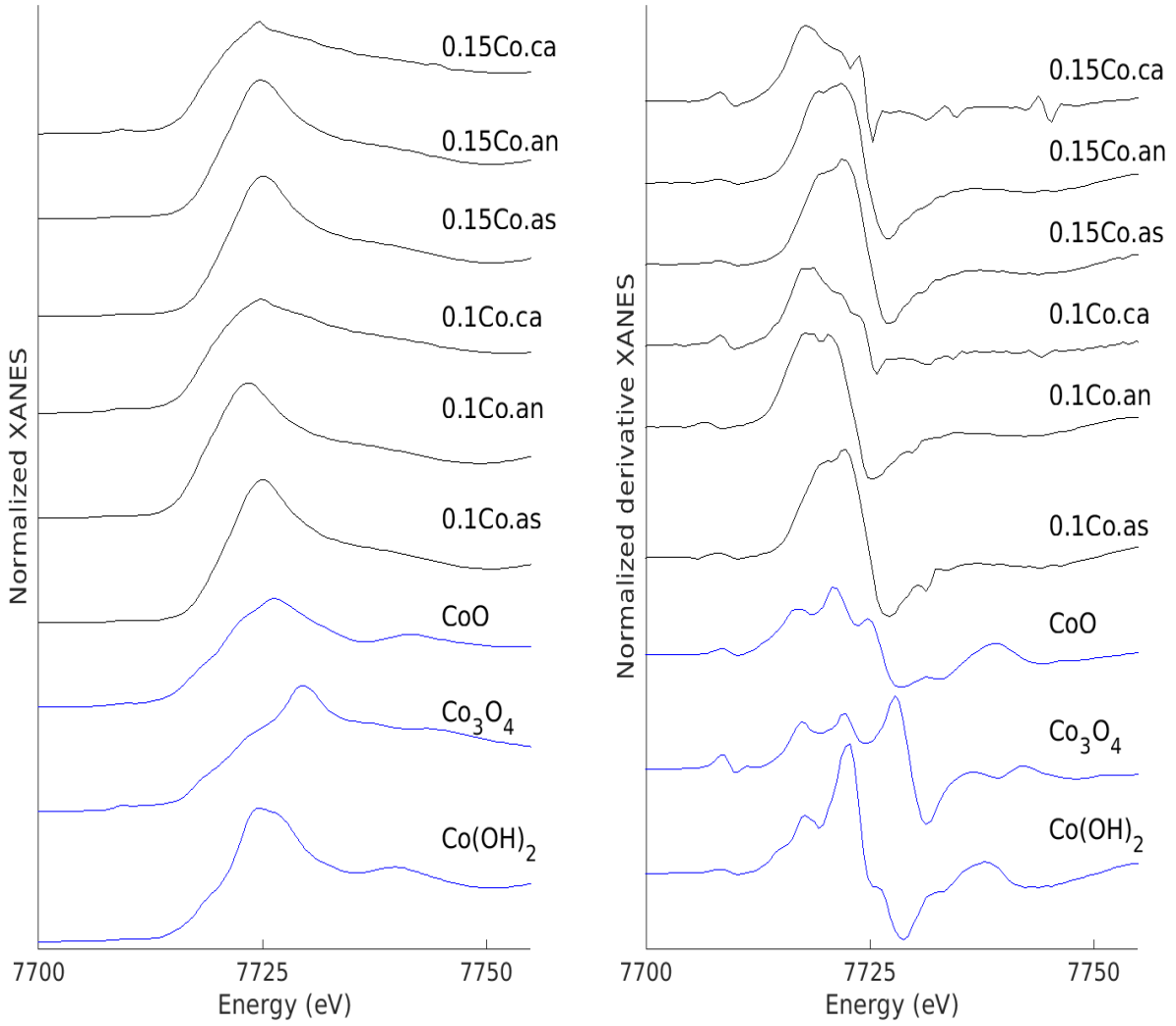

Figure. 5.22. Normalized XANES (*left*) and the normalized derivative XANES (*right*) of the samples, Co0.1 and Co0.15, coloured in black and the reference compounds, CoO, Co_3O_4 and $Co(OH)_2$, coloured in blue.

Oxidation state of the cobalt species in the sample can be determined from the E_0 obtained from the absorption edge. This can be done by plotting E_0 of references against the known oxidation state of cobalt in reference compounds. The oxidation number of samples can then be calculated from the trendline drawn with respect to the reference compounds. (Figure 5.23) The known oxidation state of cobalt in each reference compound and measured E_0 is given in Table 5.10.

Table 5.10. Known oxidation number of cobalt in reference compounds, CoO, Co_3O_4, $Co(OH)_2$ and cobalt foil, and absorption energy (E_0) obtained from the edge in XANES.

Sample Name	E_0 (eV)	Oxidation Number
Co Foil	7709	0
CoO	7717.27	2
Co_3O_4	7718.26	2.667
$Co(OH)_2$	7717.81	2

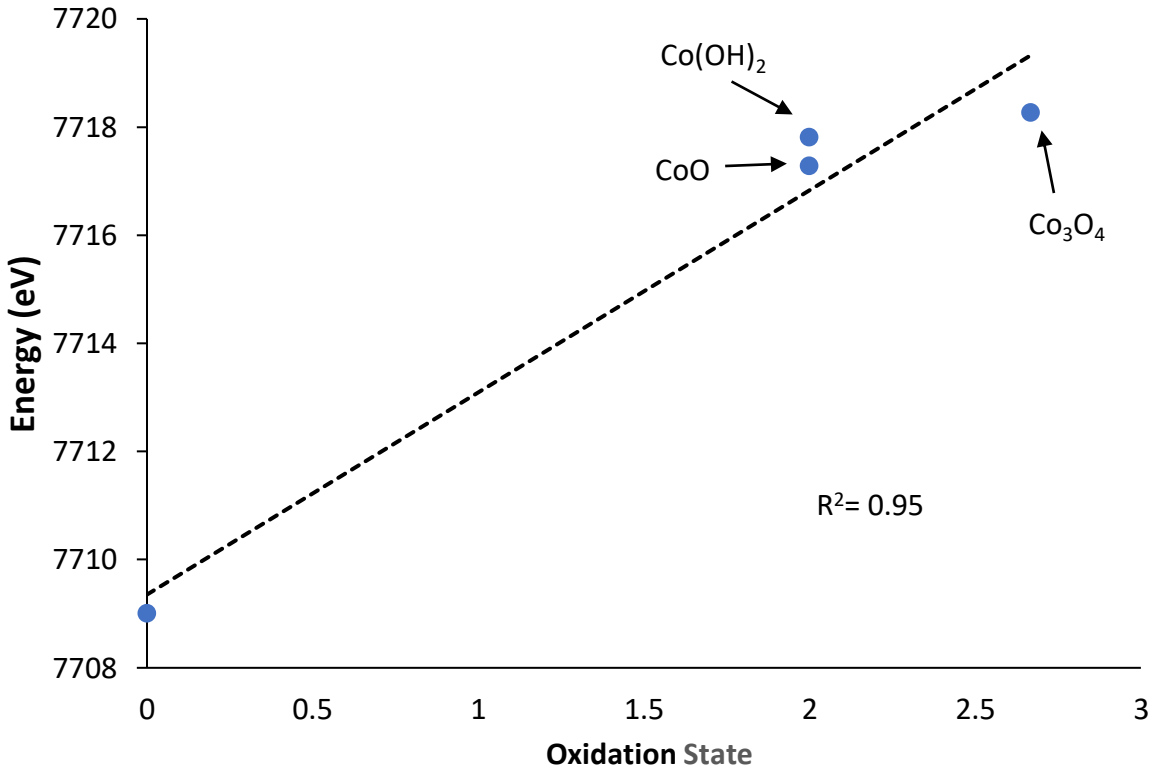

Figure 5.23. A plot of measured absorption energy against the known oxidation state of cobalt in reference compounds, CoO, Co_3O_4, $Co(OH)_2$ and cobalt foil, with a trendline with R^2 is equal to 0.95.

Summary of calculated oxidation states of cobalt in each sample is shown in Table 5.11. Both as prepared sample have an oxidation number at 2.4, which indicates the presence of Co^{2+} and Co^{3+} site (Co^{2+}: Co^{3+} = 60:40) in the gel. When samples are heated at higher temperature, the oxidation number decreases. In calcined samples, all cobalt species have an oxidation state of

2+. It suggests that some Co^{3+} sites in the gel is reduced to Co^{2+} during heat treatment., which is not expected.

Table 5.11. Summary of absorption energy (E_0) obtained from the edge in XANES and calculated oxidation number of cobalt species in the samples, 0.1Co and 0.15Co, before and after heat treated.

Sample Name	E_0 (eV)	Oxidation Number
0.1Co.as	7718.44	2.4
0.1Co.an	7716.55	1.9
0.1Co.ca	7717.01	2.0
0.15Co.as	7718.38	2.4
0.15Co.an	7718.16	2.4
0.15Co.ca	7717.19	2.1

A pre-edge or small shoulder can be seen in all samples and the reference compounds. Plots of the pre-edge of samples (Appendix D) and reference compound (Figure 5.24) in the range between 7704eV - 7714 eV is provided. According to data extracted from the references, Co^{2+} compounds give a pre-edge centroid energy at 7709eV. (Table 5.10) The position of pre-edge centroid energy in samples are about 7708-7709eV, which suggests the Co^{2+} species present in the gel. (Table 5.11)

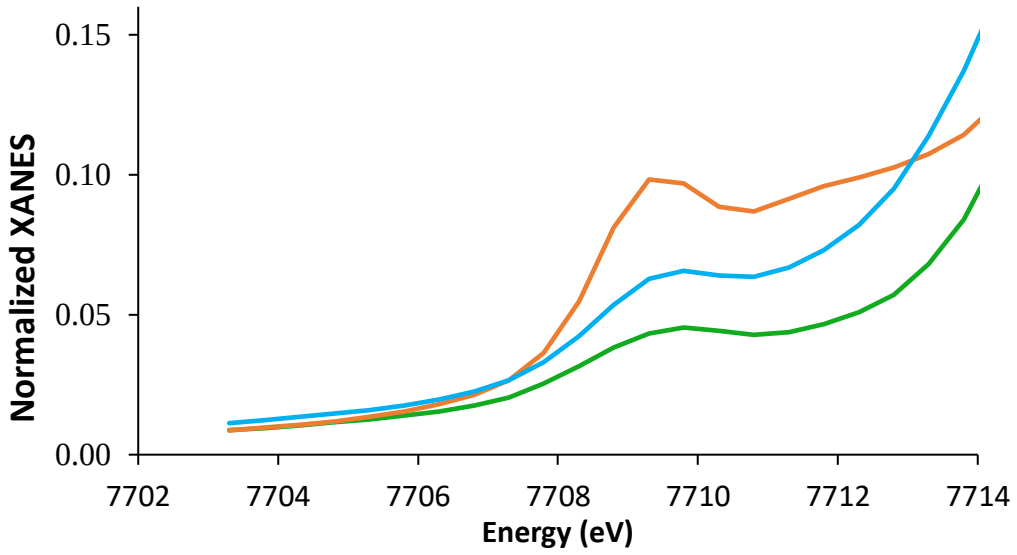

Figure 5.24. Pre-edge region of the normalized XANES of reference compounds: Co_3O_4 (orange), CoO (blue) and $Co(OH)_2$ (green)

Intensity of the pre-edge can provide information about the symmetry of the cobalt site in the gel. The intensity of the pre-edge increase as the degree of centrosymmetry decrease. In Co_3O_4, cobalt is present as both tetrahedrally coordinated Co^{2+} and octahedrally coordinated Co^{3+}.[80] Therefore, the intensity of Co_3O_4 is higher than octahedrally coordinated CoO and $Co(OH)_2$.. (Figure 5.24)

Table 5.10. Summary of pre-edge centroid energy and integrated area of the pre-edge extracted from reference samples, CoO, Co_3O_4 and $Co(OH)_2$.

Reference	Centroid (eV)	Integrated Area	Height	R-factor
Co_3O_4	7709.14	0.66(5)	0.082(9)	0.001014
CoO	7709.42	0.8(1)	0.034(9)	0.005645
$Co(OH)_2$	7709.14	1.0(1)	0.035(6)	0.003067

Table 5.11. Summary of pre-edge centroid energy and integrated area of the pre-edge extracted from sample 0.1Co and 0.15Co.

Sample	Centroid (eV)	Integrated Area	Height	R-factor
0.1Co.as	7709.32	0.896(453)	0.03(2)	1.89×10^{-1}
0.1Co.an	7708.06	0.94(28)	0.04(2)	1.55×10^{-3}
0.1Co.ca	7709.8	0.767(103)	0.07(1)	1.05×10^{-5}
0.15Co.as	7709.46	0.881(198)	0.030(9)	01.67×10^{-3}
0.15Co.an	7709.42	0.883(207)	0.02(3)	7.52×10^{-4}
0.15Co.ca	7709.13	0.782(31)	0.065(5)	3.21×10^{-5}

An increase of pre-edge intensity is related to the transition between octahedral and tetrahedral structure where an increase in pre-edge width is related to increase in tetrahedral distortion.[81] Therefore, using integrate peak area for comparison can help understanding effects of both factors. Pre-edge area of samples increases after annealed and decrease after calcined. (Table 5.11) It suggests that transition in symmetry of cobalt site between tetrahedral and octahedral, and axial distortion occur during heating. However, there are also other factors affect the position and area of pre-edge, such as electronegativity between cobalt and the ligands.

5.5.2 EXAFS on cobalt silica aerogel

EXAFS least-square refinements of the theoretical EXAFS $k^3\chi(k)$ to the experimental $k^3\chi(k)$ were performed on all as prepared, anneal and calcined samples and reference compounds. The result is summarized in Table 5.12 and Table 5.13. AFAC is obtained from reference compounds with known coordination number and is transferred to the sample for refinement. In this work, all samples are using AFAC calculated from $Co(OH)_2$ for the refinements.

Table 5.12. EXAFS refinement results of reference compounds. The refined parameters are coordination number (N), bond length (R), Debye-Waller factor ($2\sigma^2$) energy correction of E_0 (E_F), goodness of fit (R%), k range (Δk) and Amplitude Reduction Factor (AFAC)

Reference	Shell[82]	N	R(Å)	$2\sigma^2$(Å^2)	E_F (eV)	R%	Δk	AFAC
$Co(OH)_2$	Co-O	6	2.11(1)	0.012(3)	-5(1)	43.88	3−10	0.84
	Co---Co	6	3.183(9)	0.012(2)				
CoO	Co-O	6	2.11(3)	0.004(1)	-6(1)	56.45	3−10	0.79
	Co---Co	12	3.01(1)	0.018(2)				
Co_3O_4	Co-O	5.5	1.93(2)	0.009(4)	-6(2)	57.56	3−9	0.83
	Co---Co	3.5	2.90(2)	0.009(3)				

Table 5.13. EXAFS refinement results of samples, as prepared, annealed and calcined. The refined parameters are coordination number (N), bond length (R), Debye-Waller factor ($2\sigma^2$) energy correction of E_0 (E_F), goodness of fit (R%), k range (Δk) and Amplitude Reduction Factor (AFAC)

Sample	Shell	N	R(Å)	$2\sigma^2$(Å^2)	EF (eV)	R%	Δk	AFAC
0.1Co.as	Co-O	6.0(6)	2.10(8)	0.01(3)	−4.6(7)	35.07	2−10	0.84
0.1Co.an	Co-O	5.8(6)	2.10(9)	0.01(2)	−4.5(7)	34.21	2−10	0.84
0.1Co.ca	Co-O	6.3(8)	2.00(6)	0.036(2)	1(2)	50.23	3−9	0.84
0.15Co.as	Co-O	6.2(5)	2.102(2)	0.011(2)	−4.9(6)	30.91	2−10	0.84
0.15Co.an	Co-O	5.9(3)	2.098(9)	0.01(2)	−4.5(7)	33.8	2−10	0.84
0.15Co.ca	Co-O	4.2(6)	1.99(2)	0.01(5)	1.8(2)	35.15	3−9	0.84

For as prepared and anneal sample of 0.1Co and 0.15Co, only the first shell is seen and is fitted. (Figure 5.25) The refinement shows that the scattering element is oxygen. Cobalt are bond to approximately 6 oxygen atoms in the first shell at about 2Å. This result yields an R factor 30-

35. However, for calcined samples, a second shell is shown at about 3Å. (Figure 5.26 and Appendix D) Therefore, a Fourier filtering was applied to both calcined 0.1Co and 0.15Co sample in order to identify the scattering element in the second shell.

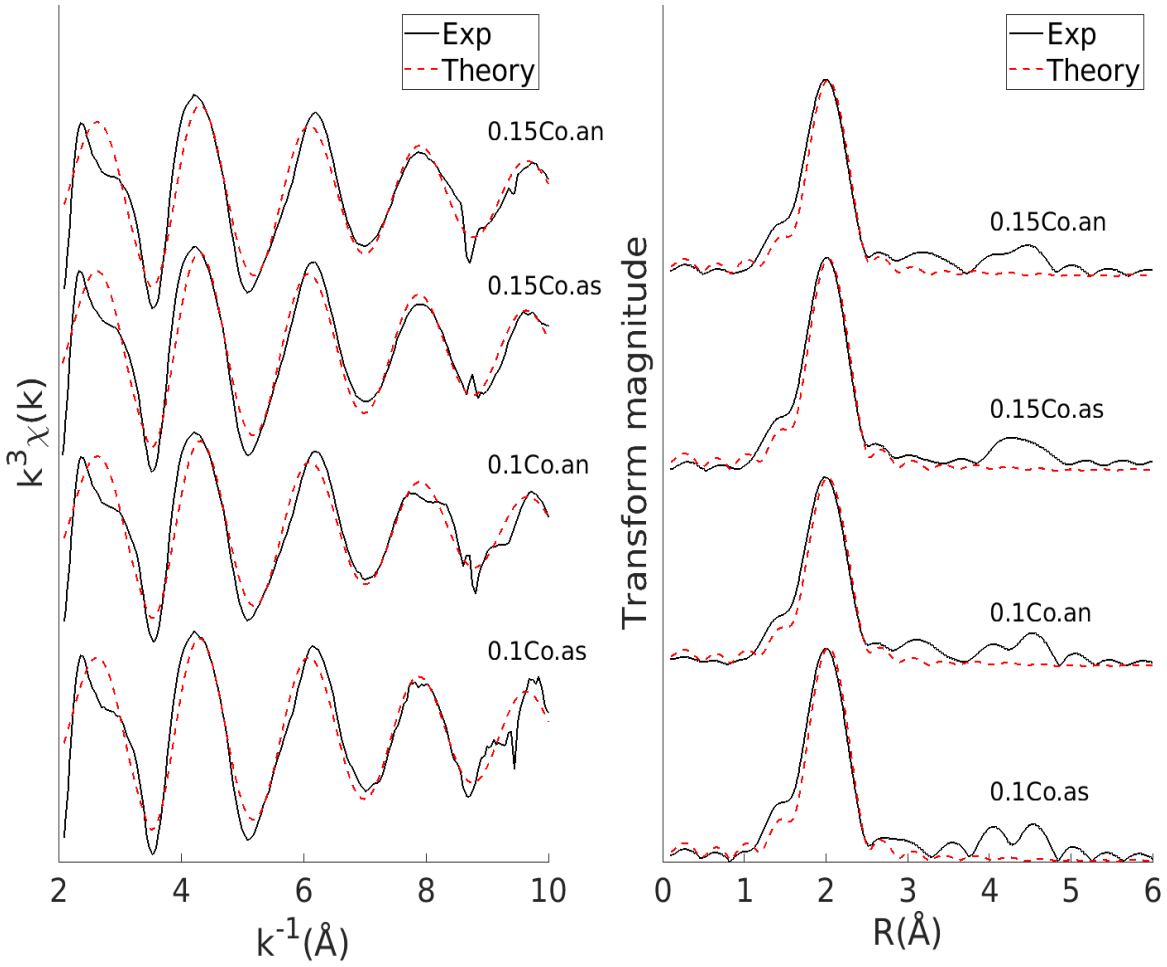

Figure 5.25. EXAFS least-square refinements of samples 0.1Co and 0.15Co as prepared (.as) and annealed (.an) sample in k^3-weighted k-space $\chi(k)$ and R-space $\chi(r)$ with k a range 2-10.

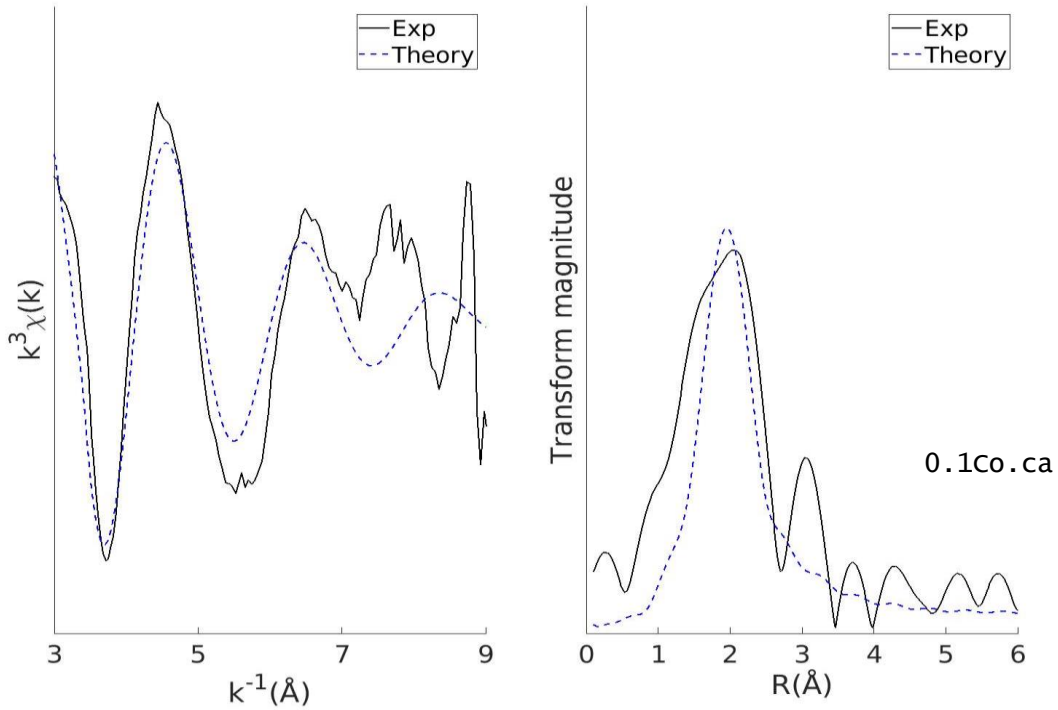

Figure 5.26. EXAFS least-square refinements of the first shell for 0.1Co calcined sample in k^3-weighting k-space and R-space.

In Fourier filtering, the least-square refinements for Co…Si, Co….O and Co…Co pairs in the second shell was performed. (Figure 5.27 and Appendix D) The refinement values are summarized in Table 5.14. Although all the refinement results give relatively low R value, not all of them are realistic. For example, the refinement suggested coordination of Co----Co pairs is 59. Therefore, cobalt species is not present in the second shell, in the other words, no unwanted Co-O-Co oxide species is found in the gel. It indicates that cobalt is incorporated into gel matrix in single site and the cobalt oxides is not formed after annealing at 450°C and calcining 700°C.

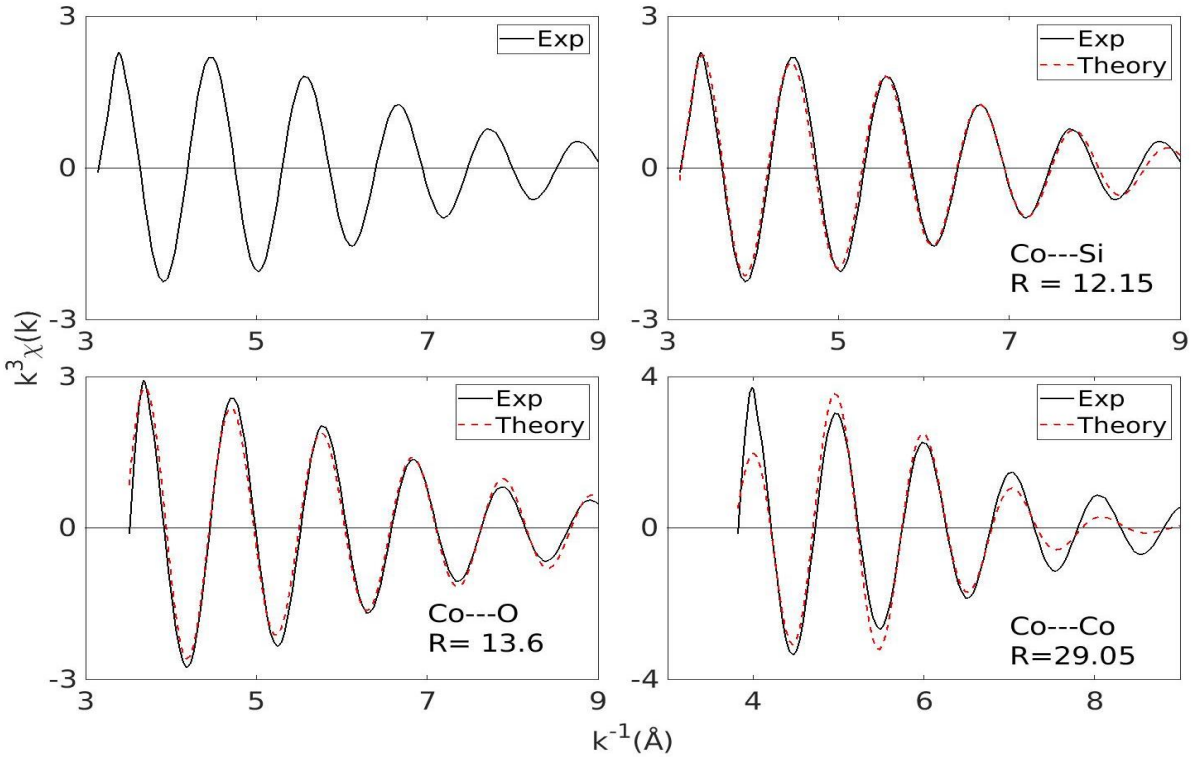

Figure 5.27. Fourie filtered to isolate the second shell of calcined 0.1Co sample. R is the goodness of fit.

Table 5.14. Fourier filtered refinement results of calcined 0.1Co and 0.15Co sample (k-range 3.4-3.2). The refined parameters are coordination number (N), bond length (R), Debye-Waller factor ($2\sigma^2$) energy correction of E_0 (E_F), goodness of fit (R%).

Sample	Shell	N	R(Å)	$2\sigma^2$(Å^2)	E_F (eV)	R%
0.1Co.ca	Co---Si	5.9(5)	3.19(3)	0.03(8)	5.5(2)	12.15
	Co---O	8.2(1)	3.30(1)	0.02(4)	14.8(4)	13.6
	Co---Co	59.4(7)	3.26(9)	0.09(5)	25(1)	29.05
0.15Co.ca	Co---Si	4.7(3)	2.99(5)	0.02(6)	14.4(3)	4.239
	Co---O	7.7(4)	3.09(0)	0.01(8)	25.3(7)	7.233
	Co---Co	24.7(4)	3.08(4)	0.06(5)	33(8)	24.83

5.6 Catalytic reaction

All catalytic testing was performed on 0.15Co. This sample is selected for testing because it retains the amorphous properties after introduction of cobalt. The structure of the gel is stable after annealed at 450°C and calcining at 700°C.

5.6.1 Hydrocarbons Selective Catalytic Reduction (HC-SCR)

HC-SCR is performed by passing reactant gas, NO, propene and O_2, through the activated sample in the tube oven. The concentration of NO was detected by the NO_x-box. The conversion of NO is calculated by the following equation:

$$Conversion\% = \frac{NO_{[bypass]} - NO_{[reactor]}}{NO_{[bypsss]}} \quad (18)$$

NO conversion is illustrated in Figure 5.28 by plotting the conversion percentage of NO against temperature. The catalyst is not active for HC-SCR, where the conversion % of NO is zero.

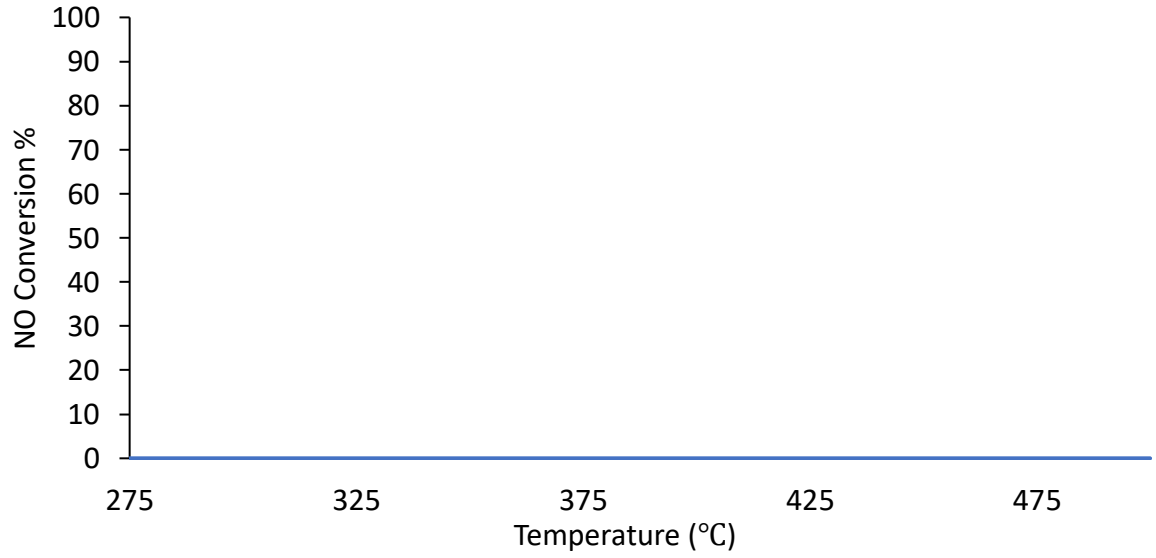

Figure. 5.28. NO conversion for 0.15Co

5.6.2 Propene oxidation

Propene oxidation is performed by passing reactant gas, propane and O_2, through the sample. The exhausted gas was analysed and measured by FT-IR. The conversion of propene was calculated by the following equation:

$$Conversion\% = \frac{C_3H_{6[bypass]} - C_3H_{6[reactor]}}{C_3H_{6[bypsss]}} \quad (19)$$

The conversion of propene is shown as a function of temperature. (Figure 5.29) The conversion % of propene is very low (below 4%), and the catalyst is inactive for propene oxidation.

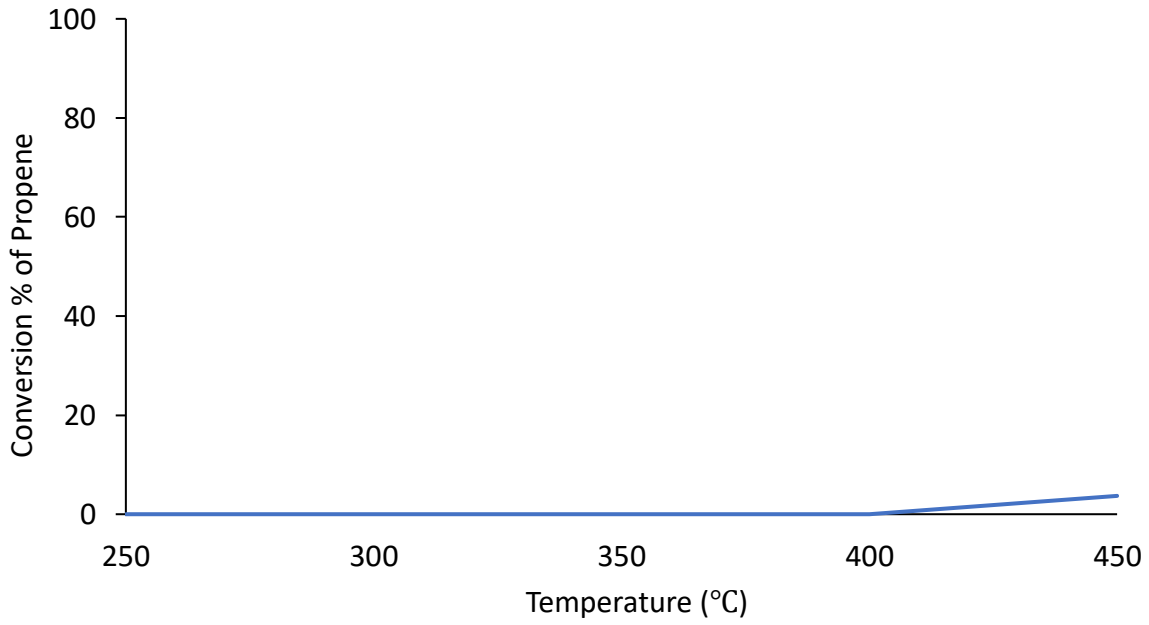

Figure. 5.29. Propene conversion for 0.15Co

5.6.3 Methanol to Hydrocarbon (MTH)

MTH was performed by flushing reactant gas into the DRIFTS cell and subsequently over the sample. Exhaust from the cell transport to the GC-MS for separation and detection of the product. The conversion of methanol is calculated and shown as a function of time in Figure 5.30. The sample is found to be inactive for MTH.

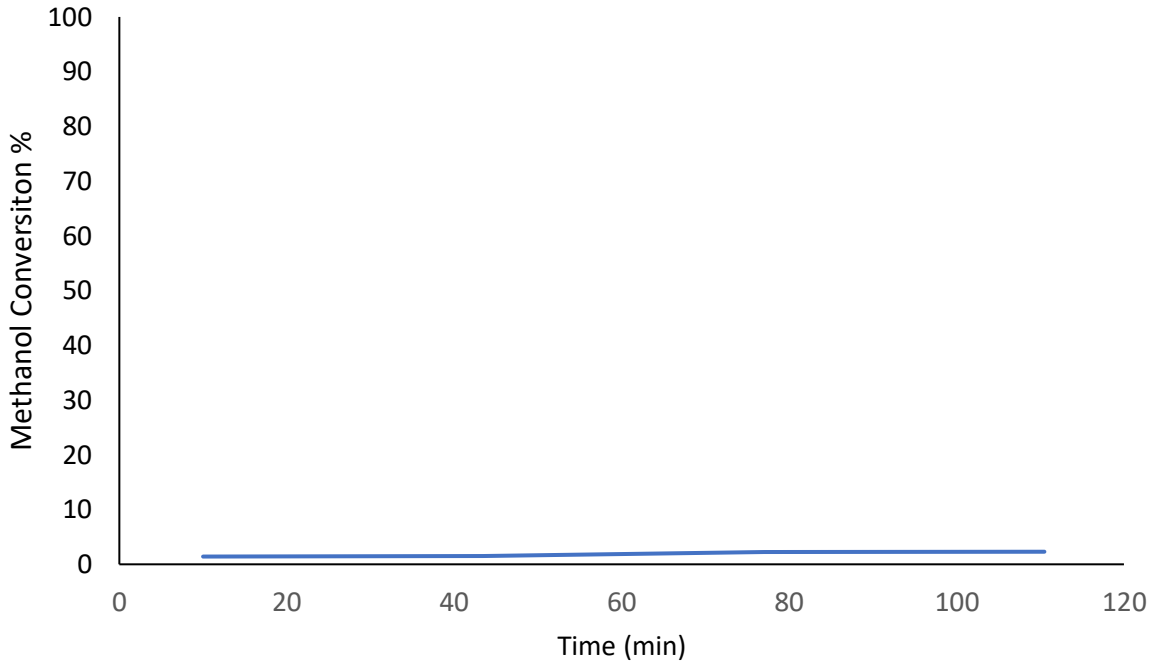

Figure. 5.30. Methanol conversion for 0.15Co

6 DISCUSSION

The goal of this project is to introduce cobalt into the matrix of water-glass based silica aerogel in single site, which has not been successfully made before. Several parameter studies have been done in this work to investigate the possibility of introducing cobalt into the gel while retaining the important features, such as amorphous structure, high surface area and high porosity, of the plain aerogel.

6.1 Effects of Introduced Cobalt on Silica Aerogel

According to the previous attempts performed by Sondre Håbrekke[1], preparing cobalt silica aerogel under basic condition results in the formation of cobalt hydroxide in the gel and oxidized to cobalt oxides at high temperature due to sintering. These oxides species can reduce the activity and selectivity of the catalyst by blocking pores and reducing dispersion of cobalt in the gel matrix.

In order to avoid the formation of these unwanted oxides, the cobalt silica aerogel is synthesised under acidic condition at pH 4. When NH_4OH is added to elevate the pH of the sol from 3 to 4 for gelation, cobalt hydroxide is formed and re-dissolve after equilibrium has reached. When $pH \geq 5$, the gelation rate increases, and the gel is formed before the cobalt hydroxide redissolve. Therefore, crystalline phases are identified by XRD analysis in samples prepared at $pH \geq 5$. However, acid catalysed gel generally has a lower surface area comparing to basic catalysed gel. It is because the colloidal silica particles at pH 4 carry a positive surface charge. Repulsion forces between particles prevents the formation of secondary particles by aggregation, resulting in a yarn like structure with small pores.[38] To prevent a further decrease in total surface area of the gel during APD, an effective surface modification agent is needed.

Samples surface modified by TMCS showed a high degree of hydrophobicity. It is because TMCS performs both solvent exchange and surface modification simultaneously. It reacts with

pore water, yields HMDSO and hydrochloric acid. (Equation 20) TMCS also reacts with silanol (Si-OH) groups on the surface and forms a hydrophobic surface for further solvent exchange. (Equation 21)

$$2\ TMCS + H_2O \rightleftharpoons HMDSO + 2\ HCl \quad (20)$$

$$TMCS + HO\text{-}Si\equiv \longrightarrow \equiv Si\text{-}O\text{-}Si(CH_3)_3 + HCl \quad (21)$$

Because of the formation of HCl as a by-product, it reacts with Co^{2+} ions in the gel, forming tetrachloridocobaltate (II) ion, $[CoCl_4]^{2-}$, which can be indicated by the colour change from pink to blue, and signals in XRD diffractograms. (Equation 22)

$$[Co(H_2O)_6]^{2+} + HCl \rightarrow [CoCl4]^{2-} \quad (22)$$

Comparing to TMCS, HMDSO is a less effective silylation agent. When the gel surface is hydrophobized, water is expelled out from the pores. Since HMDSO and water is immersible, the water layer is formed around the gel and isolates the gel from HMDSO, eventually, surface modification no longer takes place. Samples prepared with HMDSO did not show hydrophobicity, which might due to the incomplete surface modification. In order to increase the effectiveness of HMDSO, ethanol is added to the surface modification solution. Alcohols have a bifunctional nature (polar/nonpolar) that can promote the miscibility of water and HMDSO, as well as the organic exchange solvent.[33]

The surface area of the aerogel can also be affected by the exchange solvent used during preparation. Exchanging water with a low surface tension solvent can minimized the capillary forces that causing pore structure to collapse during drying.[46] N-heptane and n-hexane were used in this project to study the effect of exchange solvents on cobalt silica aerogel. According to XRD analysis, crystalline phases were found in all samples prepared using n-hexane as the exchange solvent. It can be explained by the increase in silica solubility with the decrease of the solvent molecular weight.[83] Cobalt species may leave the gel matrix when silica particles dissolve and reprecipitate, which can be observed from the pink colour of the used surface

modification solution. Surface modification by HMDSO is also performed at different temperatures, r.t, 50°C, 55°C and 60°C, to investigate how changes in temperature affect the activity of HMDSO in surface modification. In BET/BJH analysis, it shows that there are no significant differences in surface area between sample modified at room temperature and at 50°C. It suggests that either increase in modification temperature does not influence the reactivity of HMDSO or heating at 50°C is not high enough to see a significant change in surface area. However, samples surface modified above 55°C are found to have unwanted crystalline phases. It is because the solubility of silica increases as temperature increase, and so cobalt species leave the gel matrix. Therefore, 50°C is the maximum surface modifying temperature that can be used to prepare an amorphous cobalt silica aerogel. Introduction cobalt into the gel matrix also affects the structure of the gel. As prepared plain silica aerogel has a total surface area of 446 m^2/g. As cobalt cation introduced into the gel, the surface area and pore volume increases, as pore size decreases. For as prepared sample with 1.9 wt % of cobalt cation, the total surface area is 532 m^2/g.

Many catalytic reactions are performed at a high temperature. Therefore, characterization of annealed (at 450°C) and calcined (at 700°C) samples are done to ensure the synthesised gel is thermally stable. Gels that prepared at pH4 and ISE/MS in a solution containing HMDSO, ethanol and n-heptane retained its amorphous structure at high temperature. The total surface area of the aerogel remained the same before annealing at 450°C and halved while calcining at 700°C. The losses of the surface area are due to the decrease in pore volume which may be the result of a condensation reaction between two adjacent silanol groups on the wall of the pores, forming Si-O-Si bonds. This reaction is irreversible and so causing shrinkage in a gel.

6.2 Identifying Single Site Cobalt silica aerogel

By looking at the XRD diffractograms, the absent of reflection signals suggest that the gel is amorphous, and cobalt is introduced into the gel matrix. However, it is unable to tell whether the cobalt species is incorporated in single site. Information about the local structure of cobalt in the gel can be obtained by using XAS, and to identify the presence of unwanted Co-O-Co bonds in the gel matrix.

Due the lack of resemblance in XANES spectra between the sample and reference compound, the local structure of cobalt atoms in the gel is expected to be different from those in the CoO, Co_3O_4 and $Co(OH)_2$. From the XANES spectra of samples, oxidation state of cobalt in the gel can be estimated from the absorption edge. The result suggested that the presence of mostly Co^{2+} species are found in the gel matrix.(84) An unexpected decrease in oxidation state is also observed for sample after heating in air. However, oxidation state is not the only factor changes the position of E_0. Apart from the valency, coordination number, electronegativity of the atom pair forming the bond and covalency of the bond also contribute to the shift of E_0.(75)

To gain quantitative information for the first shell, the linear least square combination refinements is preformed to obtain structural parameters, such as bond length, coordination number and Debye-Waller factor, of cobalt atom in the gel. The results suggest that the first shell only contains oxygen atoms and the average bond length, R_{Co-O}, is about 2Å. The refinement results also suggest that the cobalt atoms in the as prepared samples have an octahedral coordination. The small changes of coordination number in as prepared, annealed and calcined samples is observed. It can be attributed to the decrease in level of structural disorder surrounding the cobalt atoms, related to the decrease value of Debye-Waller factor, when sample is heat treated. This structural distortion can also be seen in the pre-edge of XANES spectra. The distortion in octahedral complex allows s⟶d transition to happen and can observed by the change of pre-edge area. Larger pre-edge area indicates more distortion of the octahedral structure in as prepared sample comparing to the calcined samples.

From the Fourier transformed spectra, $\chi(R)$, only the scattering signal from the first nearest shell atoms is observed. This suggests that only the first shell around cobalt atoms in as prepared and annealed sample is highly ordered and any structure beyond the first shell is lack of long-range order. This indicates that the sample have an amorphous structure, which agrees with its XRD result. The absent of an observable second shell at 3Å in $\chi(R)$ indicates that the cobalt atoms in sample prepared is in a single site environment, which has no indication of Co-O-Co bond in the gel matrix. The local environment of cobalt atoms is also observed to be thermally stable after heating at 450°C.

7 CONCLUSION

A single site cobalt silica aerogel has been successfully made via sol-gel method by using sodium silicate as silica precursor. XAS analysis was done on the sample to study the local environment of cobalt atoms in the gel matrix. The absent of second shell in EXAFS indicates the Co-O-Co bonds is not present in the gel matrix. The amorphous structure and thermal stability of the silica aerogel can be maintained only if the gel is synthesis at pH4. Using TMCS as the silylation agent, n-hexane as exchange solvent and surface modifying at high temperature can cause cobalt species to exit from the gel matrix, leading to the formation of cobalt oxides. Although the surface area of cobalt silica aerogel is in the acceptable range that reported in literature (400-1000m^2/g),[85] it is still relatively low compare to the gel synthesised with different surface modification agents, such as TMCS. The incomplete hydrophobization of the gel surface cause an irreversible shrinkage in the gel structure after calcined. However, the samples were not active for catalytical reaction. such as HC-SCR, MTH and propane oxidation.

7.1 Future Work

According to the work done by Hu et al. and Li et al, resistance of cobalt towards both oxidation and reduction has been observed in single site supported cobalt catalysts under reaction condition.[86, 87] This may be related to low catalytic activity reported in the work. To confirm this, in-situ XAS can be performed to investigate the change in oxidation state and chemical environment during catalytic performance and heating in reducing and oxidizing atmospheres. It also has been reported that tetrahedral Co^{2+} supported on silica has higher catalytic activity in propane dehydrogenation reaction comparing to the octahedral Co^{2+} site. Therefore, further studies can also be done on investigating the effect of change in contribution of tetrahedral and octahedral cobalt site on the catalytic activity. Hu et al reported that tetrahedral Co^{2+} active site in the gel can be prepared by using Co (III) precursors.[86] It can also be done by adding hydrogen peroxide to Co (II) precursors before mixing with the sol. [88] Catalytic activity can also increase by increasing cobalt loading of the gel. According to previous studies, the co-precursor method offers the advantage of an improved cobalt intake by the gel.[1] However, addition of silylation agent into the sol during gelation may affect the pH, resulting in the

formation cobalt hydroxide. Therefore, a precise control of pH is the key to prepare a single site cobalt silica aerogel.

Apart from HC-SCR, MTH and propene oxidation, cobalt is also found to be active for Fisher-Tropsch (F-T) synthesis. Cobalt silica aerogel prepared from tetramethoxysilane was found to be active toward F-T synthesis with good selectivity for the production of C_{10+} hydrocarbons.[4] Studies can also be done on synthesis bimetal catalyst with cobalt aerogel. Research have suggested that cobalt can act as a promoter to increase selective and reactivity of several reactions.[6, 52, 89]

8 BIBLIOGRAPHY

1. Håbrekke S. Introduction of Cobalt Into Silica Aerogels, Metal Speciation and Reducibility. In: Mathisen K, editor.: NTNU; 2017.
2. Maggio G, Cacciola G. A variant of the Hubbert curve for world oil production forecasts. Energy Policy. 2009;37(11):4761-70.
3. Fu T, Lv J, Li Z. Effect of Carbon Porosity and Cobalt Particle Size on the Catalytic Performance of Carbon Supported Cobalt Fischer-Tropsch Catalysts. Industrial & Engineering Chemistry Research. 2014;53(4):1342-50--50.
4. Dunn BC, Cole P, Covington D, Webster MC, Pugmire RJ, Ernst RD, et al. Silica aerogel supported catalysts for Fischer–Tropsch synthesis. Applied Catalysis A, General. 2005;278(2):233-8.
5. Ma Z, Dunn BC, Turpin GC, Eyring EM, Ernst RD, Pugmire RJ. Solid state NMR investigation of silica aerogel supported Fischer–Tropsch catalysts. Fuel Processing Technology. 2007;88(1):29-33.
6. Kobayashi Y, Suzuki H. Cobalt : occurrence, uses and properties. New York: Nova Publishers; 2013.
7. Schulz H. Comparing Fischer-Tropsch synthesis on iron- and cobalt catalysts: The dynamics of structure and function. Studies in Surface Science and Catalysis. 2007;163:177-99.
8. Font Freide JJHM, Collins JP, Nay B, Sharp C. A history of the BP Fischer-Tropsch catalyst from laboratory to full scale demonstration in Alaska and beyond. Studies in Surface Science and Catalysis. 2007;163:37-44.
9. Maleki H, Hüsing N. Current status, opportunities and challenges in catalytic and photocatalytic applications of aerogels: Environmental protection aspects. Applied Catalysis B: Environmental. 2018;221:530-55.
10. Thomas JM, Raja R, Lewis DW. Single-Site Heterogeneous Catalysts. Angewandte Chemie International Edition. 2005;44(40):6456-82.
11. Thomas J, Raja R. The advantages and future potential of single-site heterogeneous catalysts. Topics in Catalysis. 2006;40(1):3-17.
12. Rao A, Pajonk G. Hydrophobic and Physical Properties of the Two Step Processed Ambient Pressure Dried Silica Aerogels with Various Exchanging Solvents. Journal of Sol-Gel Science and Technology. 2005;36(3):285-92.
13. Kristiansen T, Mathisen K, Einarsrud MA, Bjorgen M, Nicholson DG. Single-Site Copper by Incorporation in Ambient Pressure Dried Silica Aerogel and Xerogel Systems: An X-ray Absorption Spectroscopy Study. J Phys Chem C. 2011;115(39):19260-8.
14. Kistler SS. Coherent Expanded Aerogels and Jellies. Nature. 1931;127(3211):741.
15. S.S.Kistler. Coherent Expanded Aerogel and Jellies. Nature. 1931;127:741.
16. Fricke J. Aerogels — a Fascinating Class of High-Performance Porous Solids. Springer Proceedings in Physics. 1986;6.
17. Maleki H, Durães L, Portugal A. An overview on silica aerogels synthesis and different mechanical reinforcing strategies. Journal of Non-Crystalline Solids. 2014;385:55–74.
18. Soleimani Dorcheh A, Abbasi MH. Silica aerogel; synthesis, properties and characterization. Journal of Materials Processing Tech. 2008;199(1):10-26.
19. Wittwer V. DEVELOPMENT OF AEROGEL WINDOWS. J Non-Cryst Solids. 1992;145(1-3):233-6.

20. Geis S, Müller B, Fricke J. Dielectric Constants of SiO2 and RF Aerogels Measured by a Response Function Method. Journal of Porous Materials. 2000;7(4):423-33.
21. Perdigoto MLN, Martins RC, Rocha N, Quina MJ, Gando-Ferreira L, Patrício R, et al. Application of hydrophobic silica based aerogels and xerogels for removal of toxic organic compounds from aqueous solutions. Journal of Colloid And Interface Science. 2012;380(1):134-40.
22. Štandeker S, Novak Z, Knez Ž. Removal of BTEX vapours from waste gas streams using silica aerogels of different hydrophobicity. Journal of Hazardous Materials. 2009;165(1-3):1114-8.
23. Gurav JL, Jung I-K, Park H-H, Kang ES, Nadargi DY. Silica Aerogel: Synthesis and Applications. Journal of Nanomaterials. 2010;2010(2010).
24. Foster HD, Keyes DB. Catalysts for the Vapor-phase Oxidation of Acetaldehyde. Industrial & Engineering Chemistry. 1937;29(11):1254-60.
25. Parvathy Rao A, Venkateswara Rao A. Microstructural and physical properties of the ambient pressure dried hydrophobic silica aerogels with various solvent mixtures. Journal of Non-Crystalline Solids. 2008;354(1):10-8.
26. Brinker CJ. Sol-gel science : the physics and chemistry of sol-gel processing. Scherer GW, editor. Boston: Academic Press; 1990.
27. Einarsrud MA, Nilsen E, Rigacci A, Pajonk GM, Buathier S, Valette D, et al. Strengthening of silica gels and aerogels by washing and aging processes. Journal of Non-Crystalline Solids. 2001;285(1):1-7.
28. Chou K, Lee B. Solvent effect on ageing of silica gels. Journal of Materials Science. 1994;29(13):3565-71.
29. Tadjarodi A, Haghverdi M, Mohammadi V, Rajabi M. Synthesis and Characterization of Hydrophobic Silica Aerogel by Two Step(Acid-Base) Sol-Gel Process. Journal of Nanostructures. 2013;3(2):181-9.
30. Silva CR, Airoldi C. Acid and Base Catalysts in the Hybrid Silica Sol–Gel Process. Journal of Colloid And Interface Science. 1997;195(2):381-7.
31. Dorcheh AS, Abbasi MH. Silica aerogel; synthesis, properties and characterization. Journal of materials processing technology. 2008;199:10–26.
32. Hüsing N, Schubert U. Aerogels—Airy Materials: Chemistry, Structure, and Properties. Weinheim1998. p. 22-45.
33. Rao AV, Pajonk GM, Bangi UKH, Rao AP, Koebel MM. Sodium Silicate Based Aerogels via Ambient Pressure Drying. 1 ed. Aegerter MA, Leventis N, Koebel MM, editors. New York, NY: New York, NY: Springer New York; 2011. 103-24 p.
34. LEE CJ, KIM GS, HYUN SH. Synthesis of silica aerogels from waterglass via new modified ambient drying. JOURNAL OF MATERIALS SCIENCE. 2002;37:2237 – 41.
35. Gurav JL, Jung I, Park H, Kang E, Nadargi DY. Silica Aerogel: Synthesis and Applications. Journal of Nanomaterials. 2010;2010:1-11.
36. Rao A, Bangi U. Low thermalconductive, transparent and hydrophobic ambient pressure dried silica aerogels with various preparation conditions using sodium silicate solutions. Journal of Sol-Gel Science and Technology. 2008;47(1):85-94.
37. Bergna HE, Roberts WO. Colloidal Silica: Fundamentals and Applications: CRC Press; 2005.
38. Knoblich B, Gerber T. Aggregation in SiO2 sols from sodium silicate solutions. J Non-Cryst Solids. 2001;283(1-3):109-13.
39. Malfait WJ, Verel R, Koebel MM. Hydrophobization of silica aerogels: Insights from quantitative solid-state NMR spectroscopy. Journal of Physical Chemistry C. 2014;118(44):25545-54.

40. Scherer GW. Aging and drying of gels. Journal of Non-Crystalline Solids. 1988;100(1):77-92.
41. Hench LL, West JK. The sol-gel process. Chemical Reviews. 1990;90(1):33-72.
42. Gurav JL, Rao AV, Rao AP, Nadargi DY, Bhagat SD. Physical properties of sodium silicate based silica aerogels prepared by single step sol–gel process dried at ambient pressure. Journal of Alloys and Compounds. 2009;476(1):397-402.
43. Shewale P, Rao A, Gurav J. Synthesis and characterization of low density and hydrophobic silica aerogels dried at ambient pressure using sodium silicate precursor. Journal of Porous Materials. 2009;16(1):101-8.
44. Cao G. Nanostructures & nanomaterials : synthesis, properties & applications. London: Imperial College Press; 2004.
45. Rao AP, Rao AV, Pajonk GM. Hydrophobic and physical properties of the ambient pressure dried silica aerogels with sodium silicate precursor using various surface modification agents. Applied Surface Science. 2007;253:6032–40.
46. Khedkar MV, Somvanshi SB, Humbe AV, Jadhav KM. Surface modified sodium silicate based superhydrophobic silica aerogels prepared via ambient pressure drying process. Journal of Non-Crystalline Solids. 2019;511:140-6.
47. Lee C, Kim G, Hyun S. Synthesis of silica aerogels from waterglass via new modified ambient drying. Journal of Materials Science. 2002;37(11):2237-41.
48. Hwang S-W, Kim T-Y, Hyun S-H. Optimization of instantaneous solvent exchange/surface modification process for ambient synthesis of monolithic silica aerogels. Journal of Colloid And Interface Science. 2008;322(1):224-30.
49. Hagen J. Industrial catalysis : a practical approach. Weinheim an der Bergstrasse, Germany: Wiley-VCH; 2015.
50. Hutter R, Mallat T, Peterhans A, Baiker A. Control of acidity and selectivity of titania–silica aerogel for the epoxidation of β-isophorone. Journal of Molecular Catalysis A, Chemical. 1999;138(2):241-7.
51. Bartholomew CH. Mechanisms of catalyst deactivation. Applied Catalysis A, General. 2001;212(1-2):17-60.
52. Casula MF, Corrias A, Paschina G. Iron-Cobalt-Silica Aerogel Nanocomposite Materials. Journal of Sol-Gel Science and Technology. 2003;26(1):667-70.
53. Dominguez M, Taboada E, Idriss H, Molins E, Llorca J. Fast and efficient hydrogen generation catalyzed by cobalt talc nanolayers dispersed in silica aerogel. Journal of Materials Chemistry. 2010;20(23):4875-83.
54. Domínguez M, Taboada E, Molins E, Llorca J. Co–SiO 2 aerogel-coated catalytic walls for the generation of hydrogen. Catalysis Today. 2008;138(3):193-7.
55. Schmid L, Rohr M, Baiker A. A mesoporous ruthenium silica hybrid aerogel with outstanding catalytic properties in the synthesis of N,N-diethylformamide from CO2, H-2 and diethylamine. Chem Commun. 1999(22):2303-4.
56. Glomm WR, Øye G, Sjöblom J. Cobalt functionalization of mesoporous silica by incipient wetness impregnation and co-precipitation. London: Taylor & Francis; 2005.
57. Dzwigaj S, Che M. Toward redox framework single site zeolite catalysts. Catalysis Today. 2011;169(1):232-41.
58. Schwarz JA, Contescu C, Contescu A. Methods for Preparation of Catalytic Materials. Chemical Reviews. 1995;95(3):477-510.
59. Thomas JM. The concept, reality and utility of single-site heterogeneous catalysts (SSHCs). Phys Chem Chem Phys. 2014;16(17):7647-61.
60. Carta D, Mountjoy G, Navarra G, Casula MF, Loche D, Marras S, et al. X-ray Absorption Investigation of the Formation of Cobalt Ferrite Nanoparticles in an Aerogel Silica Matrix. The Journal of Physical Chemistry C. 2007;111(17):6308-17.

61. Harris KDM. Powder Diffraction Crystallography of Molecular Solids. Rissanen K, editor. Berlin, Heidelberg: Berlin, Heidelberg: Springer Berlin Heidelberg; 2012. 133-77 p.
62. Kniess CT, Prates PB, de Lima JC, Kuhnen NC, Riella HG, Maliska AM. Quantitative Determination of the Crystalline Phases of the Ceramic Materials Utilizing the Rietveld Method. Materials Science Forum. 2010;660:164-9.
63. Lynch J. Physico-chemical analysis of industrial catalysts : a practical guide to characterisation. Paris: Editions technip; 2003.
64. Nishi Y, Inagaki M. Chapter 11 - Gas Adsorption/Desorption Isotherm for Pore Structure Characterization: Elsevier Inc; 2016. 227-47 p.
65. REPORTING PHYSISORPTION DATA FOR GAS SOLID SYSTEMS WITH SPECIAL REFERENCE TO THE DETERMINATION OF SURFACE-AREA AND POROSITY (RECOMMENDATIONS 1984). Pure and applied chemistry. 1985;57(4):603-19.
66. Liao J-j, Gao P-z, Xu L, Feng J. A study of morphological properties of SiO 2 aerogels obtained at different temperatures. Journal of Advanced Ceramics. 2018;7(4):307-16.
67. Thomas R. Practical Guide to ICP-MS: A Tutorial for Beginners, Third Edition: CRC Press; 2013.
68. Principles of Instrumental Analysis. Sensor Review. 1999;19(2).
69. Koningsberger DC, Mojet BL, Dorssen GEV, Ramaker DE. XAFS Spectroscopy : Fundamental Principles and Data Analysis. 2000.
70. European Synchrotron Radiation Facility. Synchrotron Science 2012, Sept 2012 [Available from: http://www.esrf.eu/about/synchrotron-science.
71. Newville M. Fundamentals of XAFS. Reviews in Mineralogy and Geochemistry. 2014;78(1):33-74.
72. Fay MJ, Proctor A, Hoffmann DP, Hercules DM. UNRAVELING EXAFS SPECTROSCOPY. Analytical Chemistry. 1988;60(21):1225A-43A.
73. O'Brien JJ, O'Brien JF. The Laporte Selection Rule in Electronic Absorption Spectroscopy: Visually Reinforcing the Result of the Transition Moment Integral. Journal of College Science Teaching. 1999;29(2):138-40.
74. George DS, Brant P, Solomon EI. Metal and ligand K-edge XAS of organotitanium complexes: Metal 4p and 3d contributions to pre-edge intensity and their contributions to bonding. Journal of the American Chemical Society. 2005;127(2):667.
75. Joseph D, Basu S, Jha SN, Bhattacharyya D. Chemical shifts of K-X-ray absorption edges on copper in different compounds by X-ray absorption spectroscopy (XAS) with Synchrotron radiation. Nuclear Inst and Methods in Physics Research, B. 2012;274:126-8.
76. Teo BK. EXAFS Spectroscopy : Techniques and Applications. New York, NY: Springer US : Imprint: Springer; 1981.
77. Kristiansen T, Støvneng JA, Einarsrud M-A, Nicholson DG, Mathisen K. There and Back Again: The Unique Nature of Copper in Ambient Pressure Dried-Silica Aerogels. The Journal of Physical Chemistry C. 2012;116(38):20368-79.
78. Ravel B, Newville M. ATHENA , ARTEMIS , HEPHAESTUS : data analysis for X-ray absorption spectroscopy using IFEFFIT. Journal of Synchrotron Radiation. 2005;12(4):537-41.
79. Tomic SS, B. G.; Wander, A.; Harrison, N. M.; Dent, A. J.; Mosselmans, J. F.W.; Inglesfield, J. E.,. New Tool for the Analysis of EXAFS: The DL_EXCURV Package. 2004.

80. Giuli G, Paris E, Hess K-U, Dingwell DB, Cicconi MR, Eeckhout SG, et al. XAS determination of the Fe local environment and oxidation state in phonolite glasses. 2011;96(4):631.
81. Dubrail J. Not all chromates show the same pre-edge feature. implications for the modelling of the speciation of cr in environmental systems. Journal of Physics: Conference Series. 2009;190(1):012176.
82. Aksoy Akgul F, Akgul G, Kurban M. Microstructural properties and local atomic structures of cobalt oxide nanoparticles synthesised by mechanical ball-milling process. Philosophical Magazine. 2016;96(30):3211-26.
83. Rao AP, Rao AV, Pajonk GM. Hydrophobic and physical properties of the ambient pressure dried silica aerogels with sodium silicate precursor using various surface modification agents. Applied Surface Science. 2007;253(14):6032-40.
84. Yildirim B, Riesen H. Coordination and oxidation state analysis of cobalt in nanocrystalline liga 5 o 8 by x-ray absorption spectroscopy. Journal of Physics: Conference Series. 2013;430(1):012011.
85. Maleki H, Durães L, Portugal A. An overview on silica aerogels synthesis and different mechanical reinforcing strategies. Journal of Non-Crystalline Solids. 2014;385(C):55-74.
86. Hu B, Getsoian A, Schweitzer N, Das U, Kim H, Niklas J, et al. Selective propane dehydrogenation with single-site Co-II on SiO2 by a non-redox mechanism. J Catal. 2015;322(C):24-37.
87. Li W, Yu SY, Meitzner GD, Iglesia E. Structure and Properties of Cobalt-Exchanged H-ZSM5 Catalysts for Dehydrogenation and Dehydrocyclization of Alkanes. The Journal of Physical Chemistry B. 2001;105(6):1176-84.
88. Liu L, Wang DK, Martens DL, Smart S, Diniz da Costa JC. Influence of sol--gel conditioning on the cobalt phase and the hydrothermal stability of cobalt oxide silica membranes.(Report). Journal of Membrane Science. 2015;475:425.
89. Czekajło Ł, Lendzion-Bieluń Z. Wustite based iron-cobalt catalyst for ammonia synthesis. Catalysis Today. 2017;286:114-7.

APPENDIX A

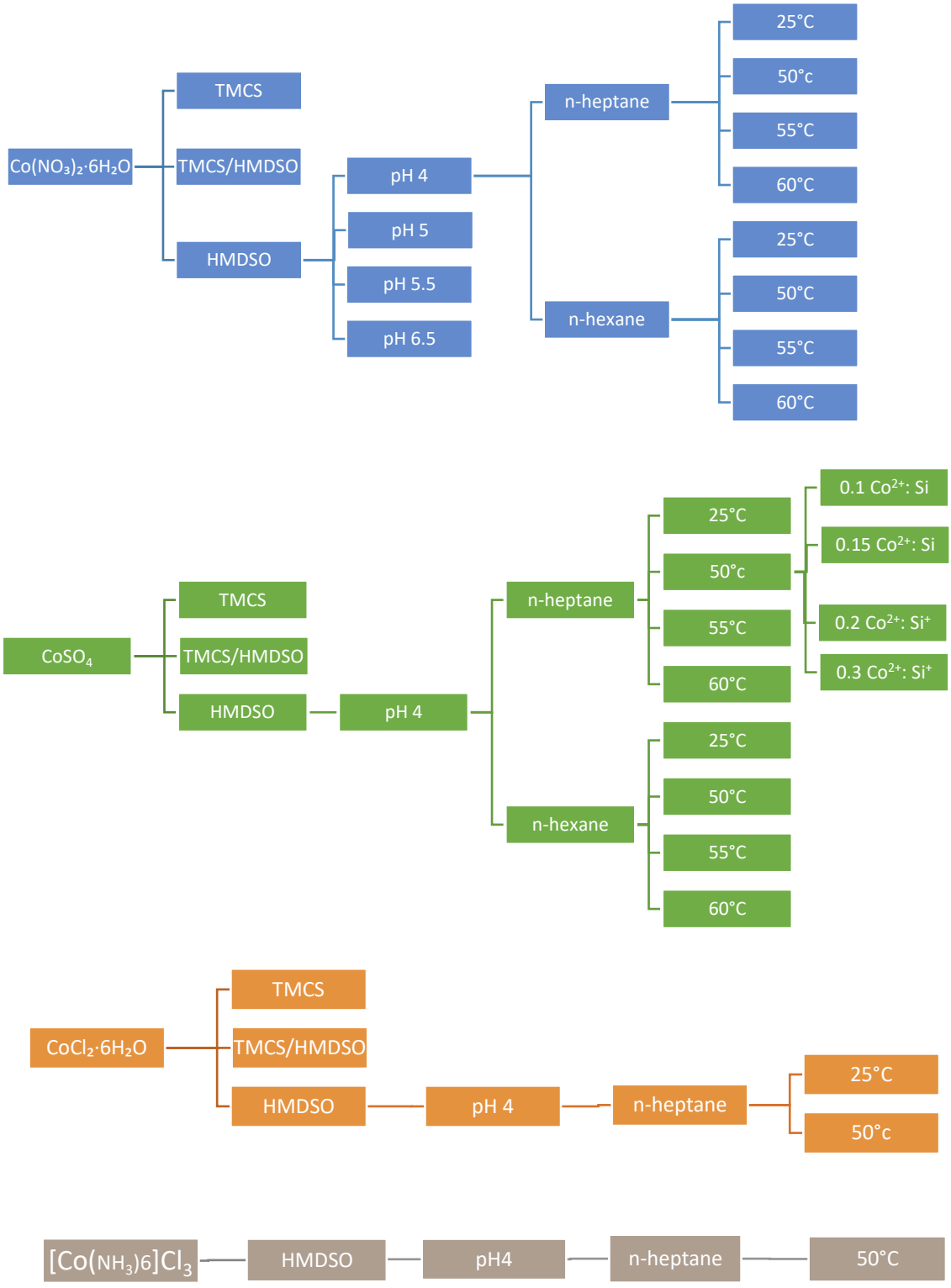

Figure A-1. Overview of all parameters studied in this project.

APPENDIX B

Additional XRD Diffractograms

- Varying Exchange Solvents and Temperature

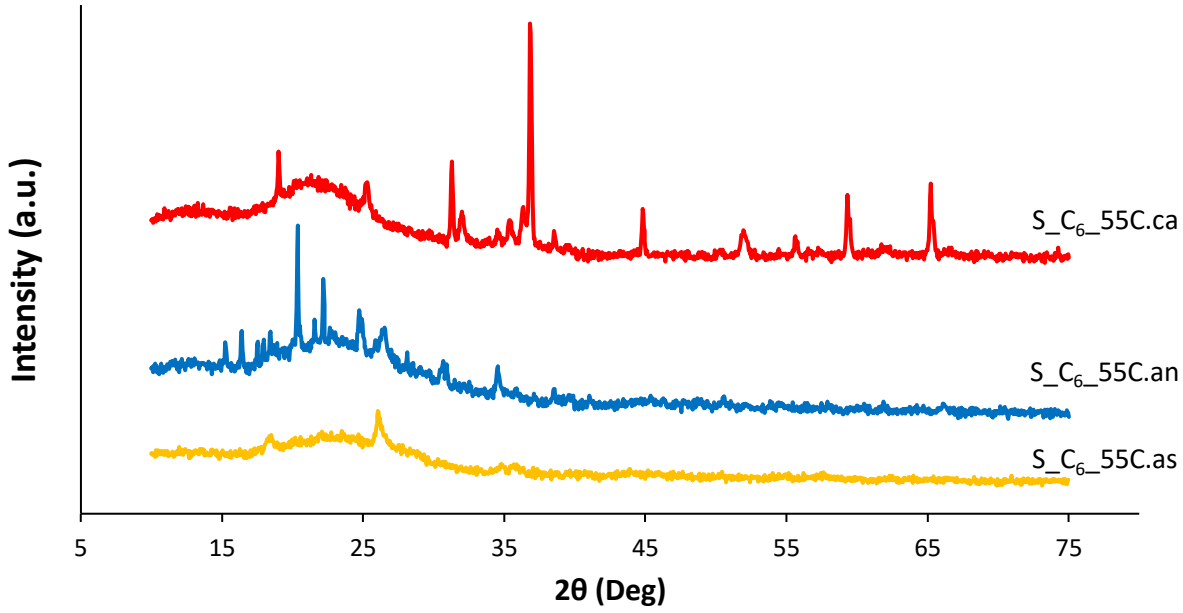

Figure. B-1. Stacked X-ray diffractograms of S_C_6_55C: as prepared (yellow), annealed (blue) and calcined (red)

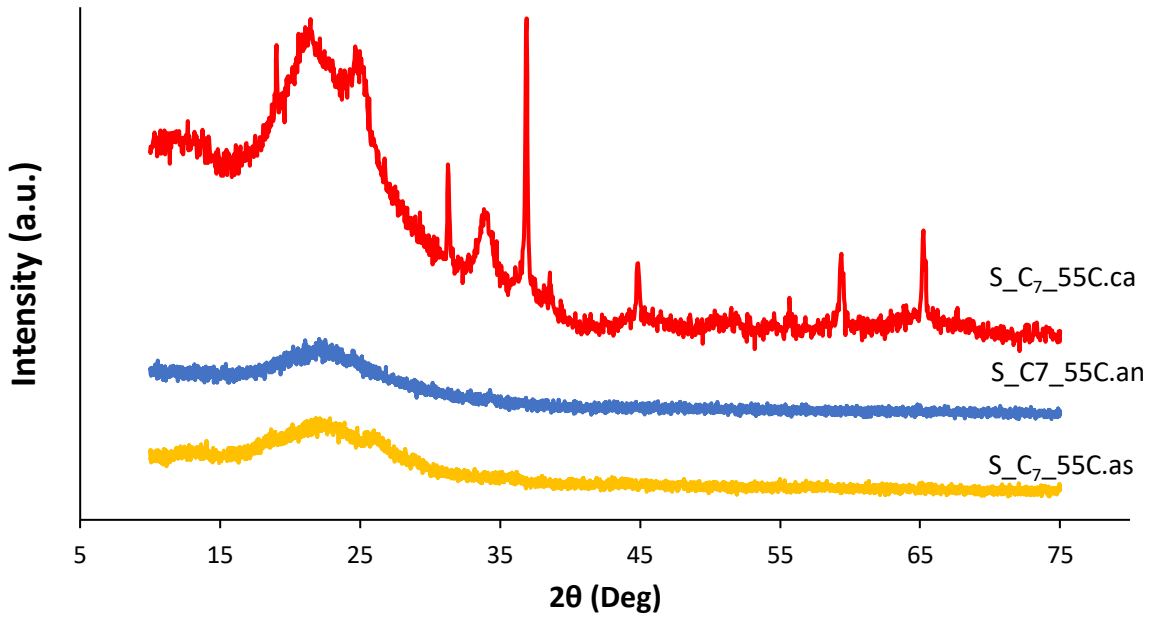

Figure. B-2. Stacked X-ray diffractograms of S_C_7_55C: as prepared (yellow), annealed (blue) and calcined (red)

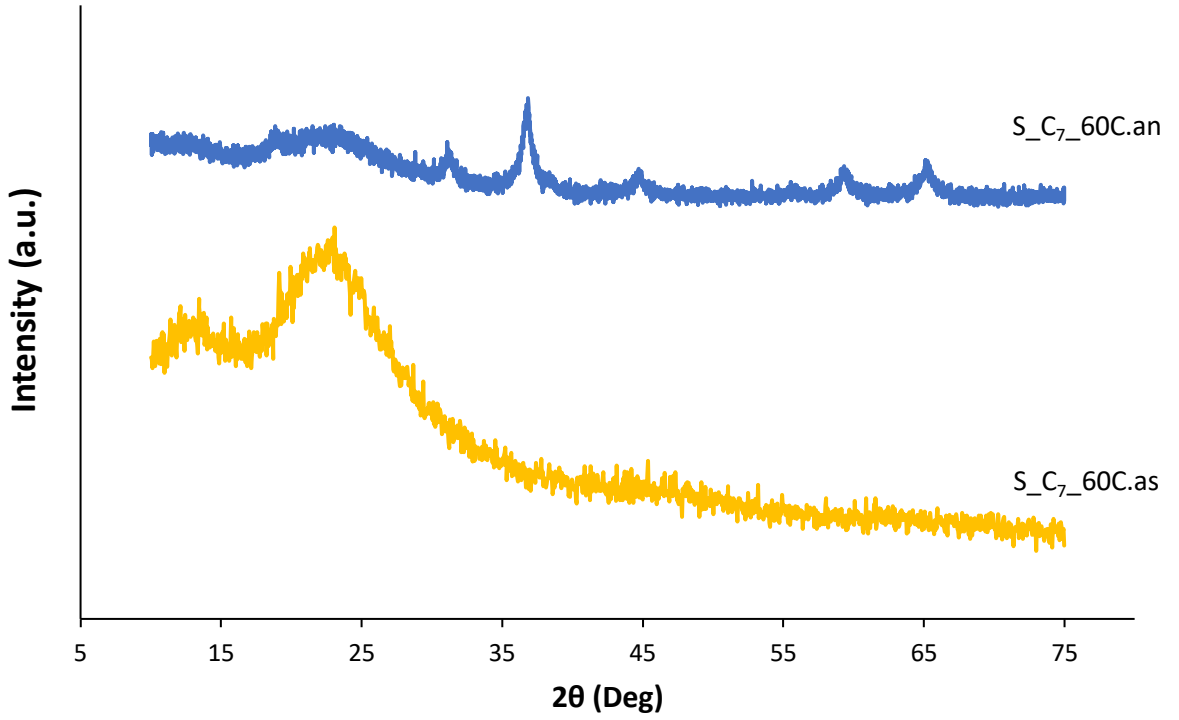

Figure. B-3. Stacked X-ray diffractograms of S_C_7_60C: as prepared (yellow) and annealed (blue)

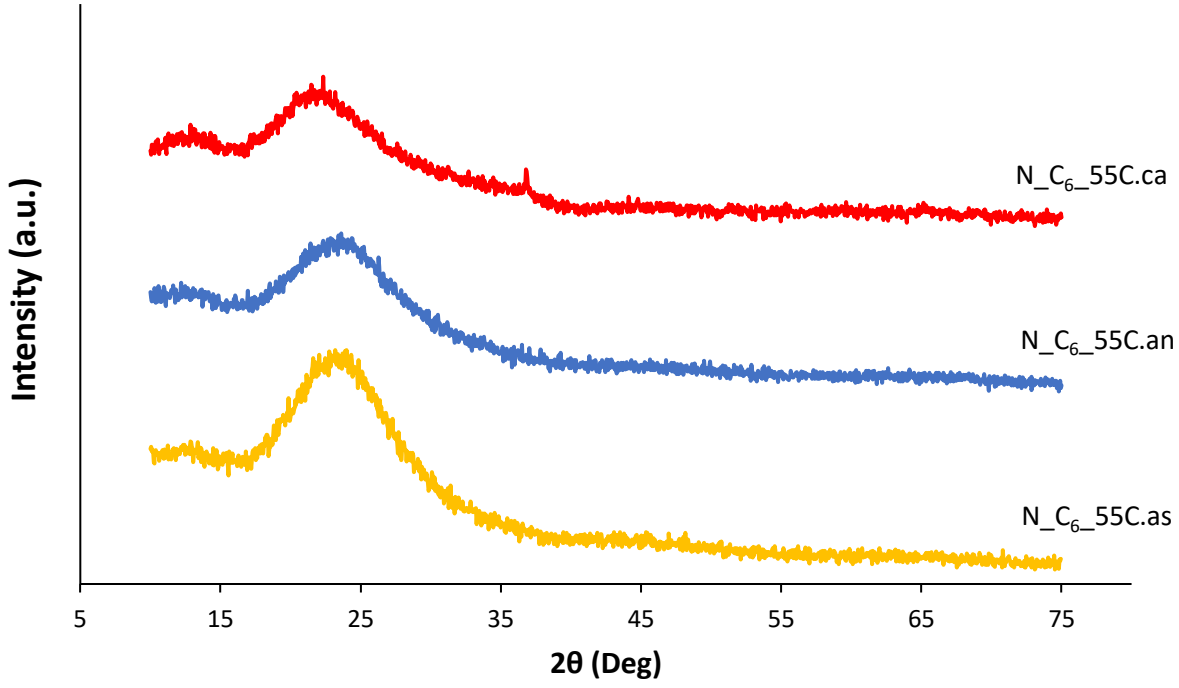

Figure. B-4. Stacked X-ray diffractograms of N_C_6_55C: as prepared (yellow), annealed (blue) and calcined (red)

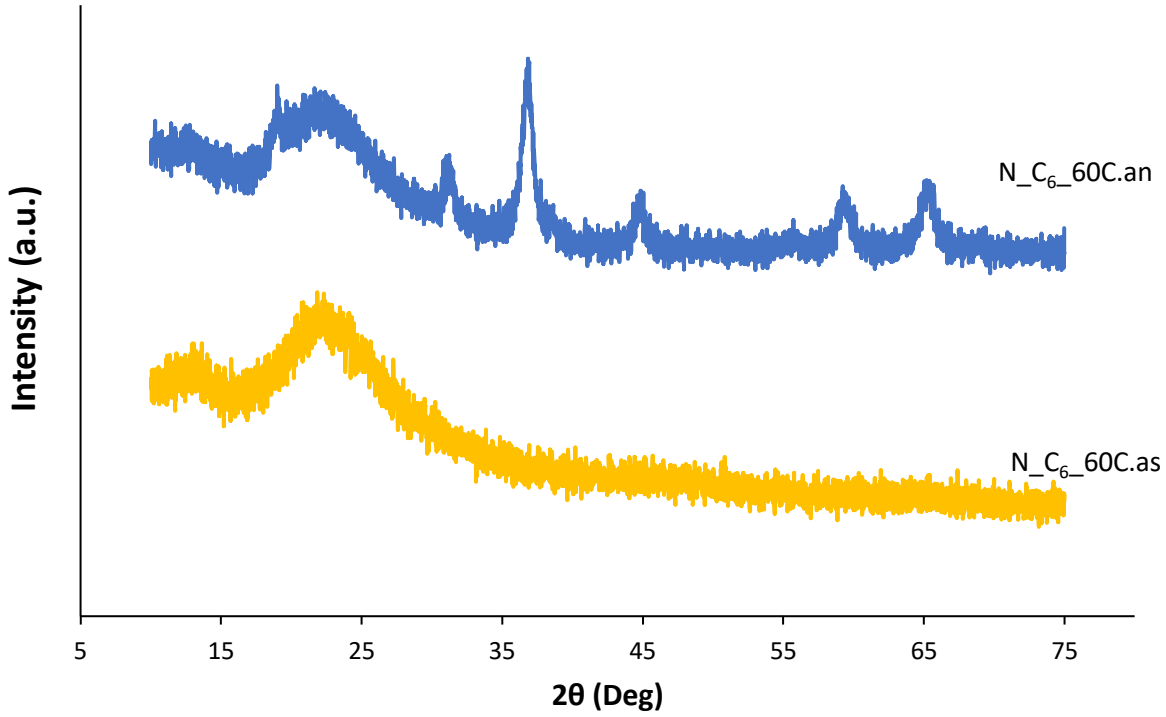

Figure. B-5. Stacked X-ray diffractograms of N_C_6_60C: as prepared (yellow) and annealed (blue)

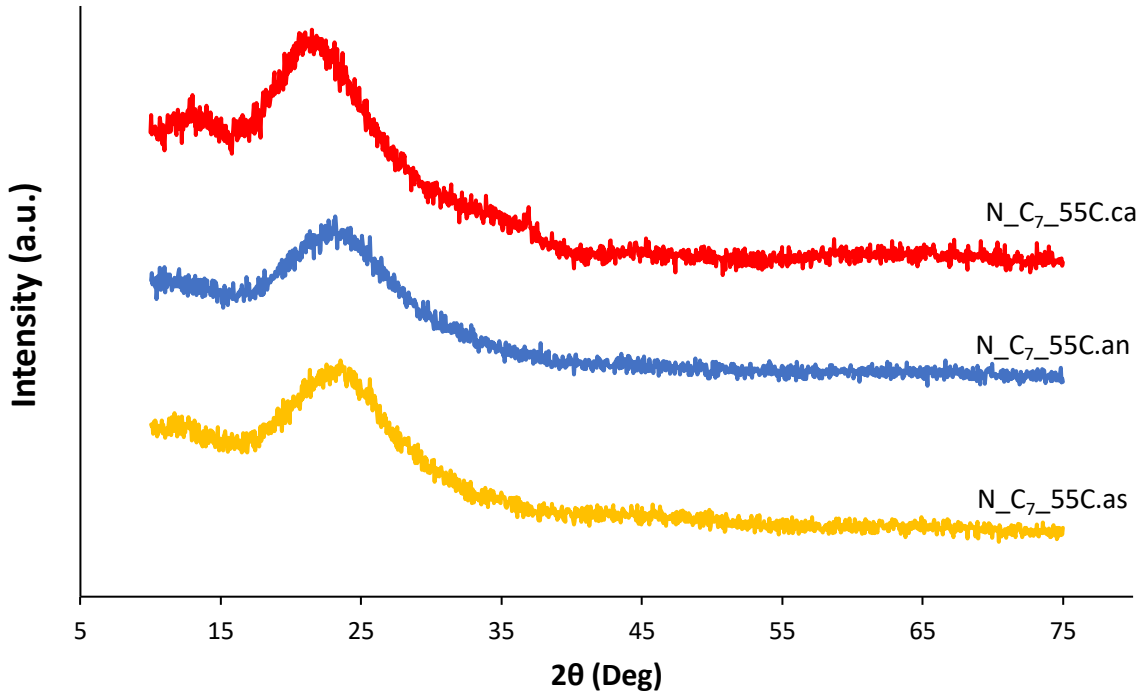

Figure. B-6. Stacked X-ray diffractograms of N_C_7_55C: as prepared (yellow), annealed (blue) and calcined (red)

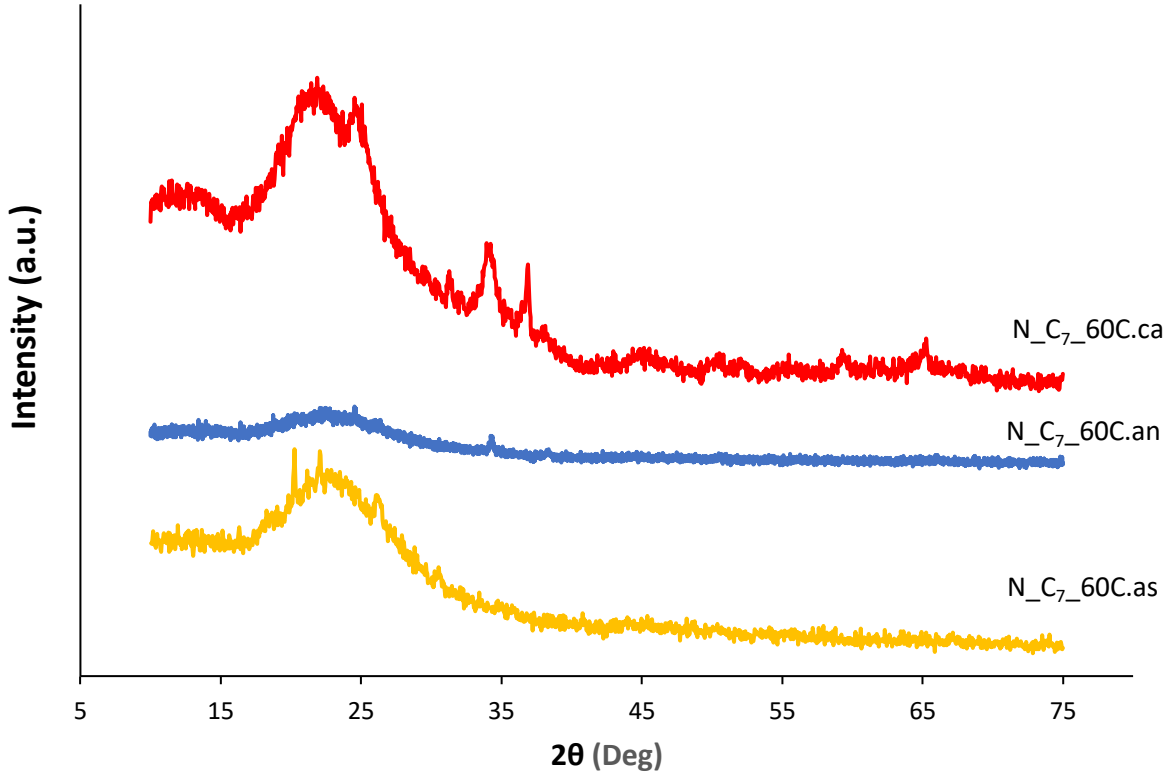

Figure. B-7. Stacked X-ray diffractograms of N_C_7_60C: as prepared (yellow), annealed (blue) and calcined (red)

- Varying Cobalt Contents

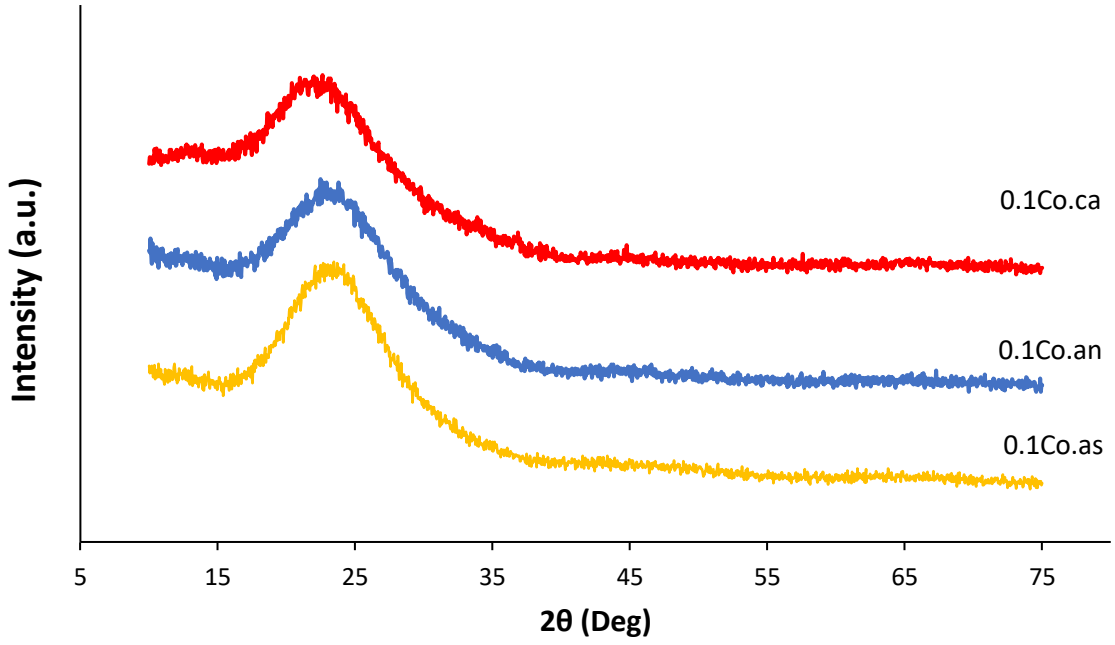

Figure. B-8. Stacked X-ray diffractograms of 0.1Co: as prepared (yellow), annealed (blue) and calcined (red)

APPENDIX C

Additional Adsorption and Desorption Isotherm and Pore distribution

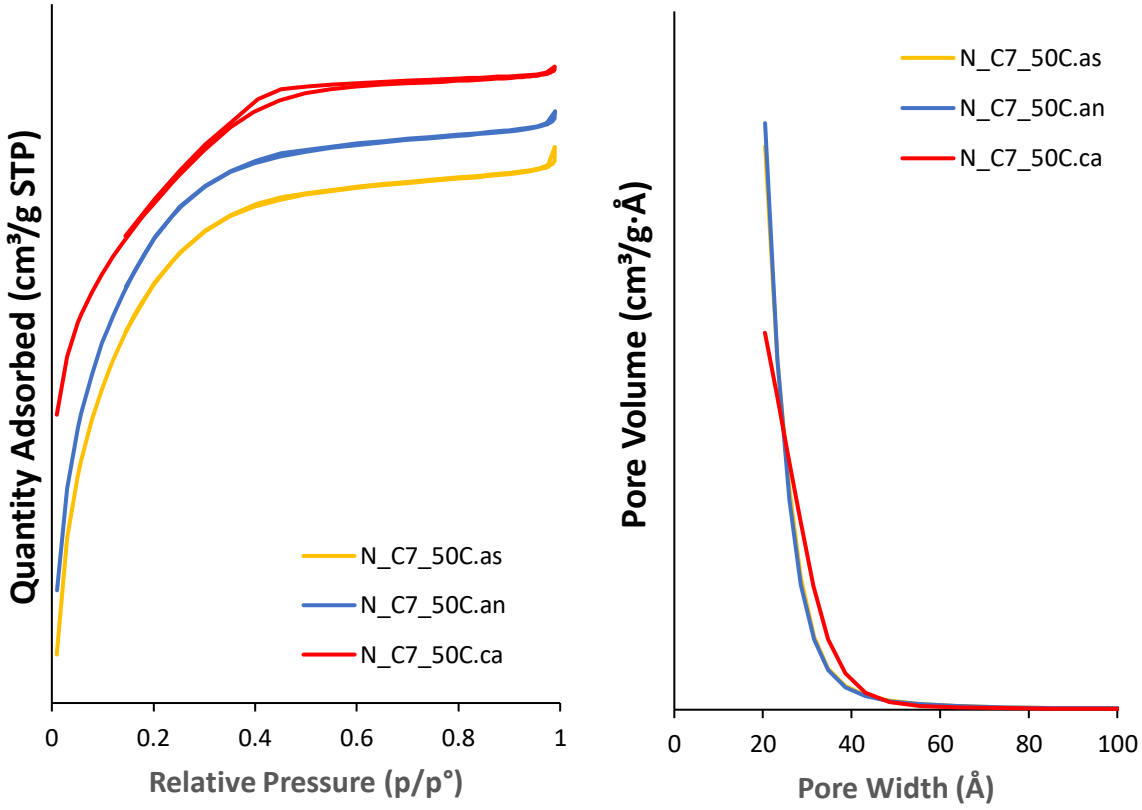

Figure. C--1. Adsorption and desorption isotherms and pore distribution of N_C_7_50C: as prepared (yellow), annealed (blue), calcined (red).

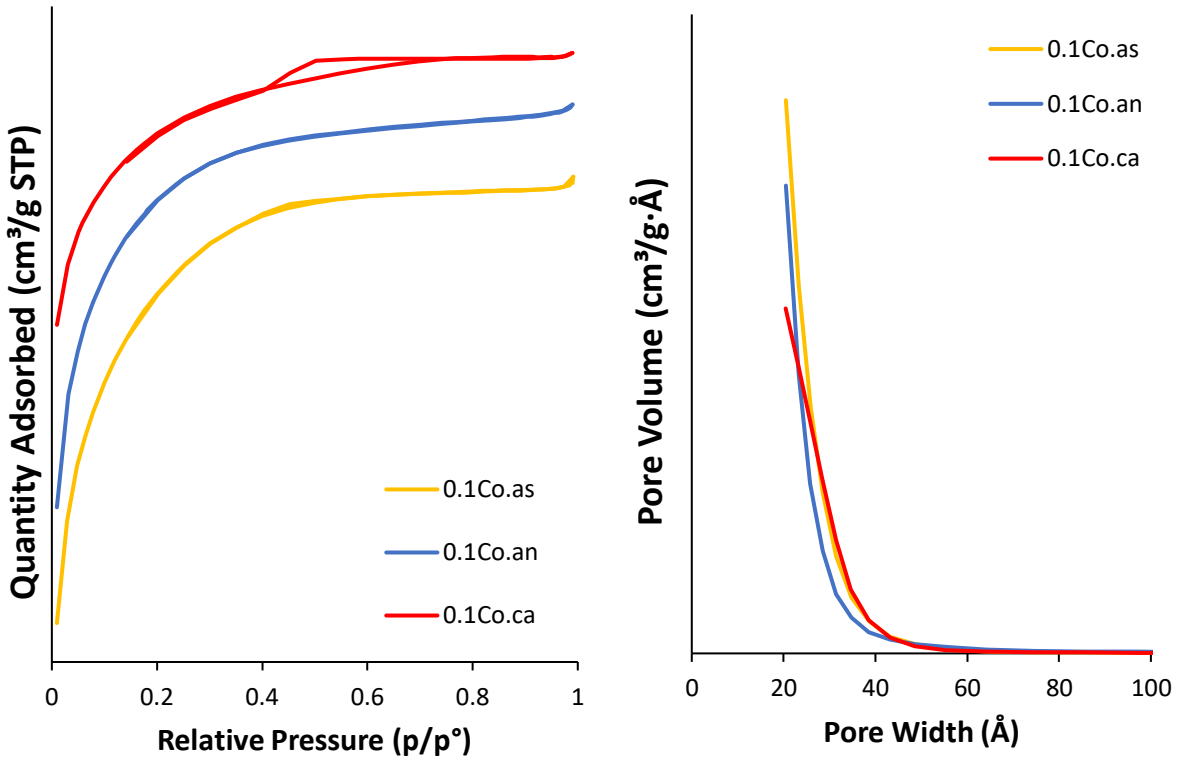

Figure. C-2. Adsorption and desorption isotherms and pore distribution of 0.1Co: as prepared (yellow), annealed (blue), calcined (red).

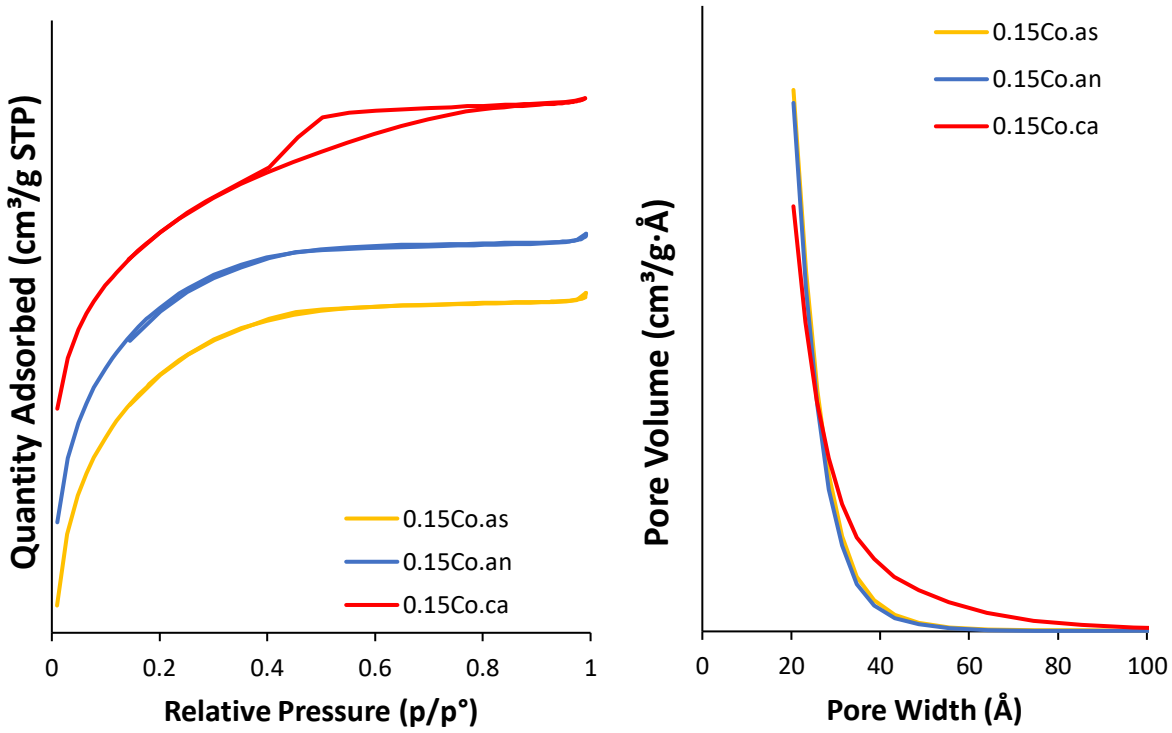

Figure. C-3. Adsorption and desorption isotherms and pore distribution of 0.15Co: as prepared (yellow), annealed (blue), calcined (red).

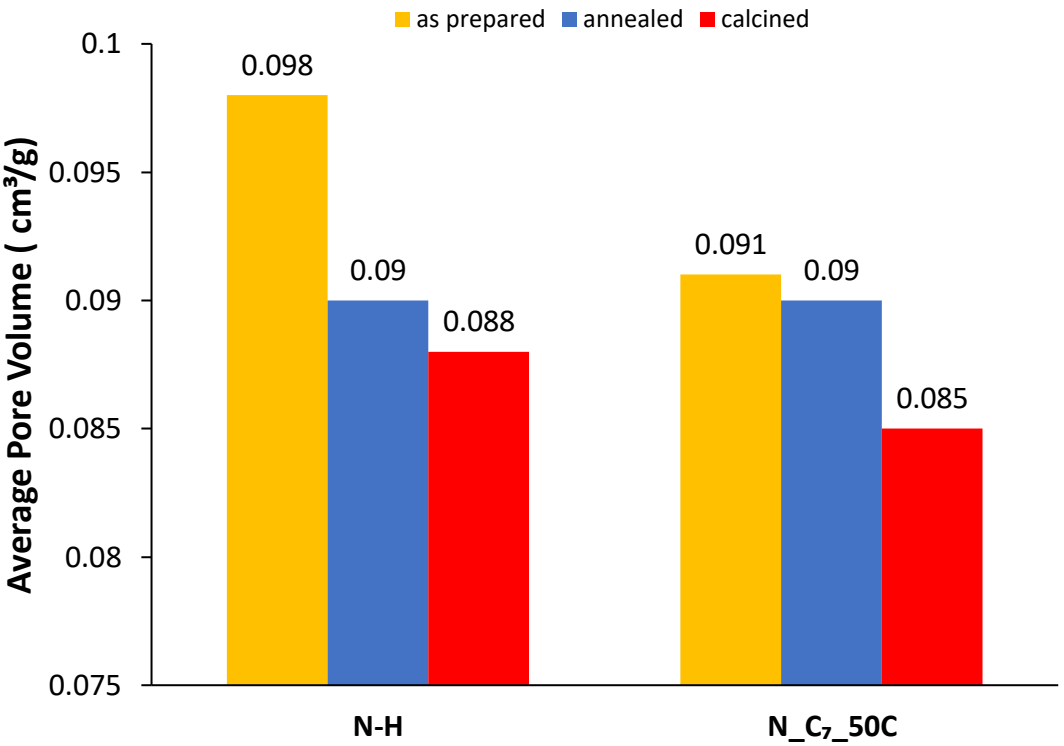

Figure C-4. Average pore volume of N(II)-H and N_C_7_50C: as prepared (yellow), annealed (blue), calcined (red).

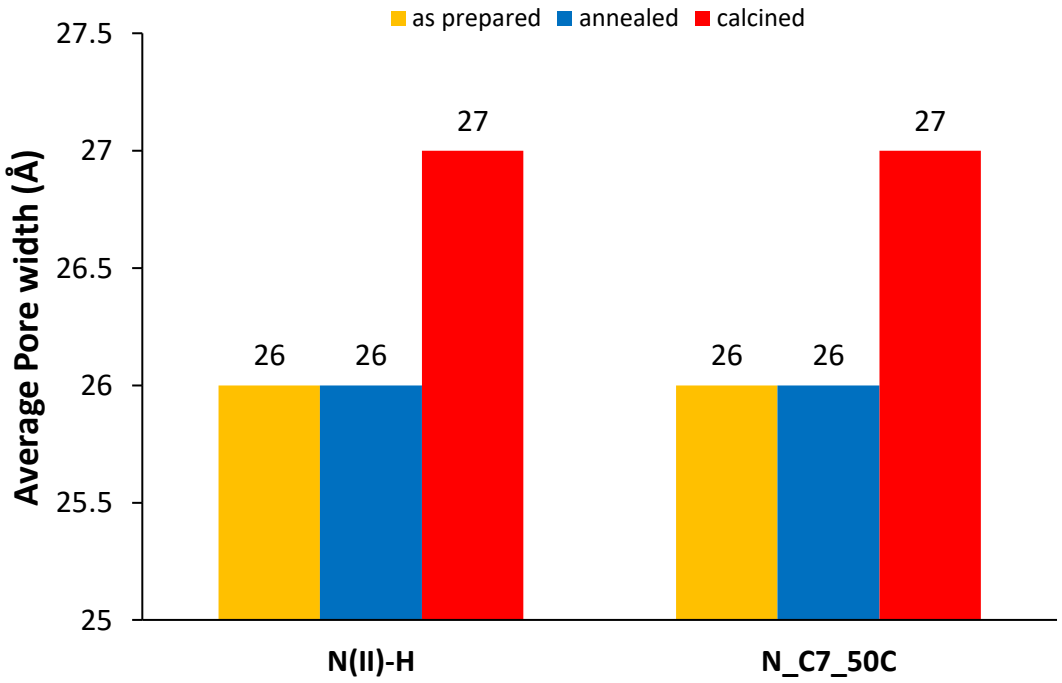

Figure C-5. Average pore width of N(II)-H and N_C_7_50C: as prepared (yellow), annealed (blue), calcined (red).

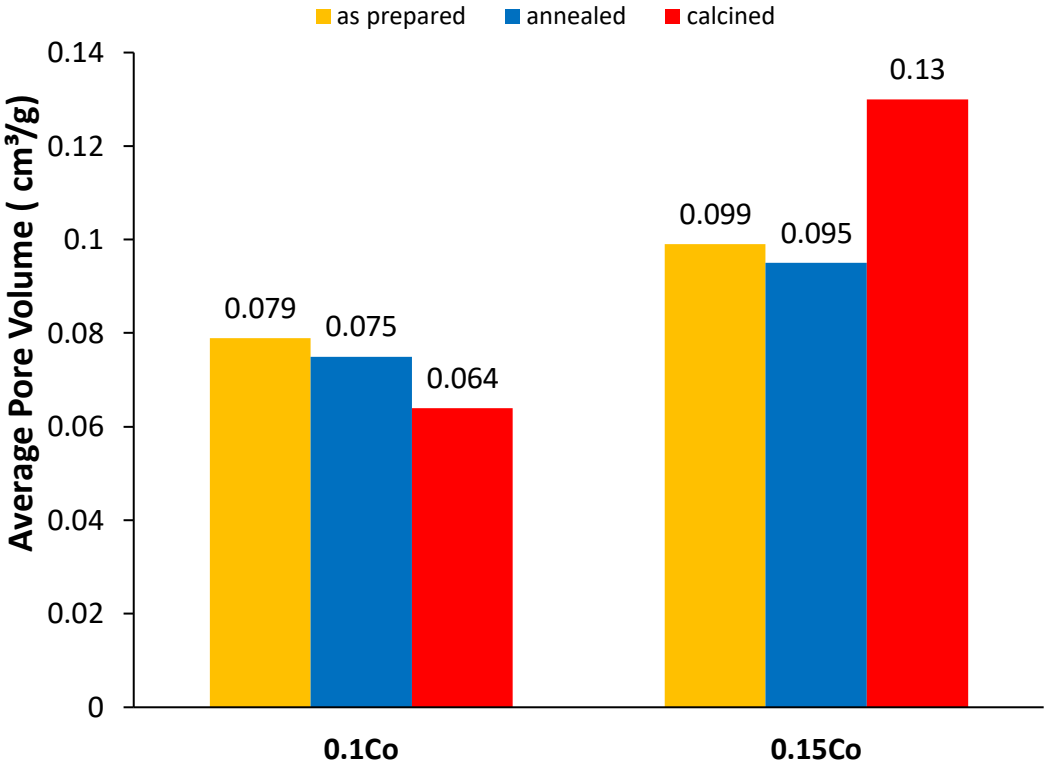

Figure C-6. Average pore volume of 0.1Co and 0.15Co: as prepared (yellow), annealed (blue), calcined (red).

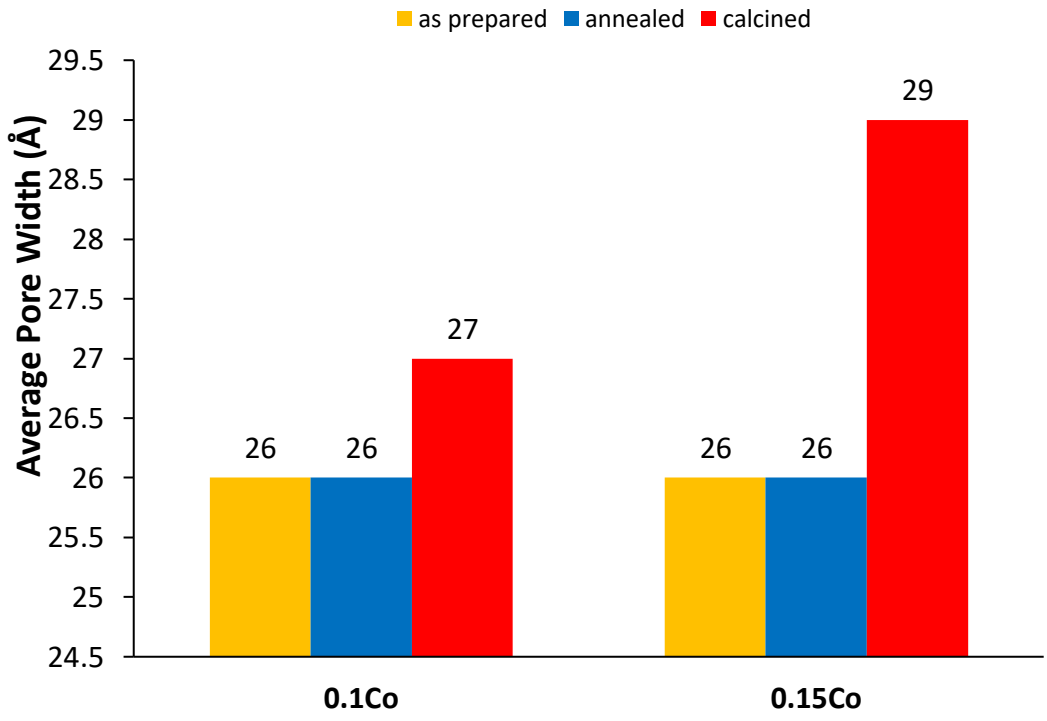

Figure C-7. Average pore width of 0.1Co and 0.15Co: as prepared (yellow), annealed (blue), calcined (red).

APPENDIX D

Additional Spectrum of XAS Analysis

- Normalized XANES and Normalized Derivative XANES

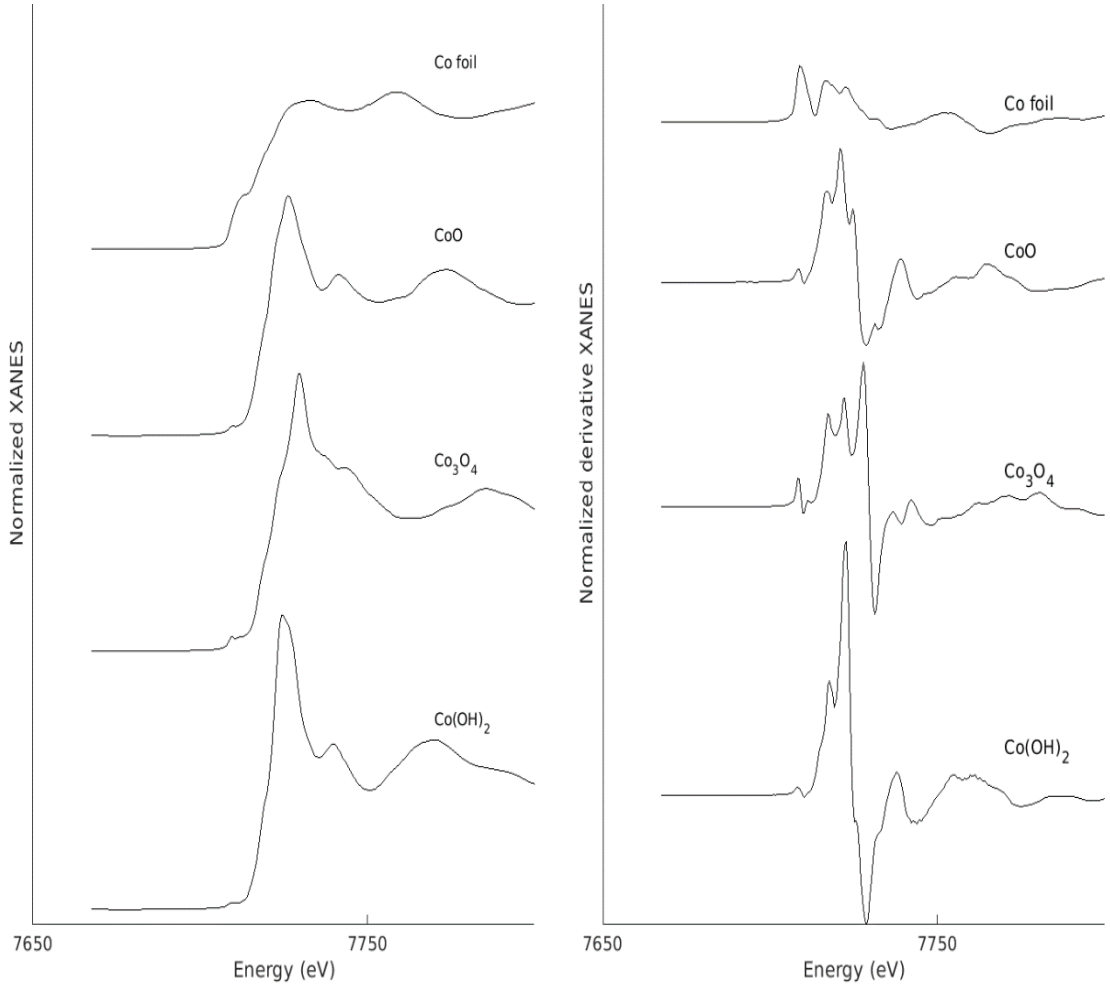

Figure D-1. Normalized XANES (left) and the Normalized Derivative XANES (right) of reference compounds: $Co(OH)_2$,Co_3O_4, CoO and cobalt foil.

- Pre-edge region of the normalized XANES

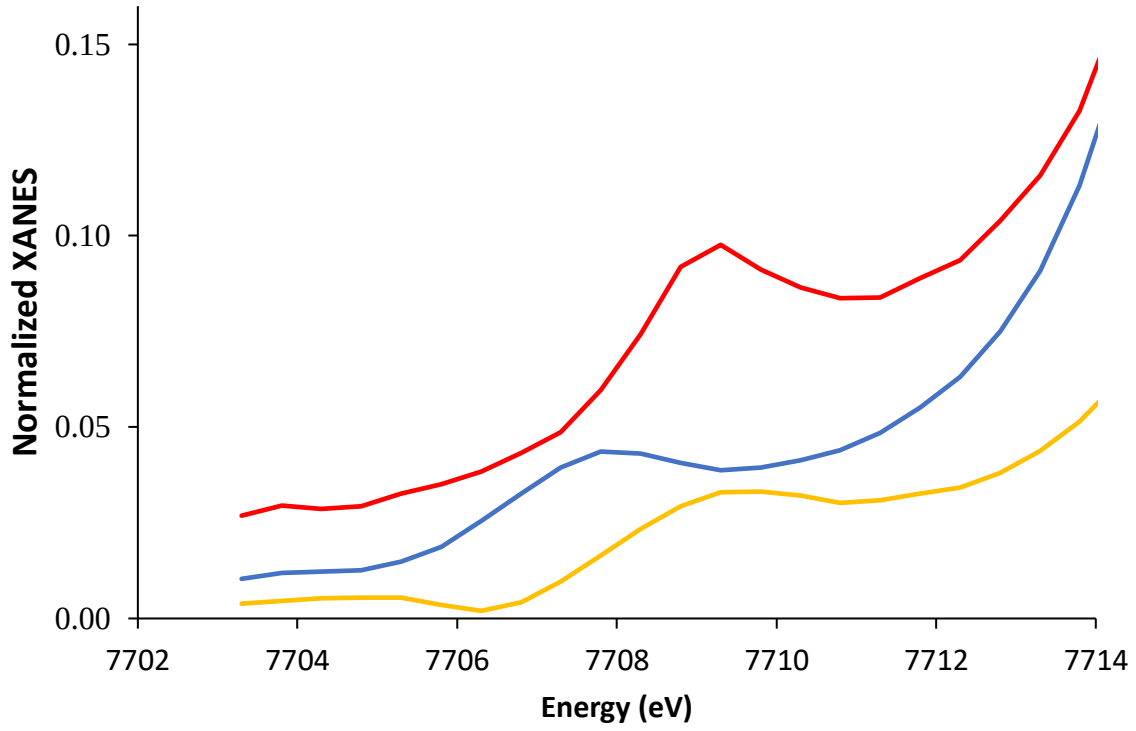

Figure D-3. Pre-edge region of the normalized XANES of 0.1Co: as prepared (yellow), annealed (blue) and calcined (red)

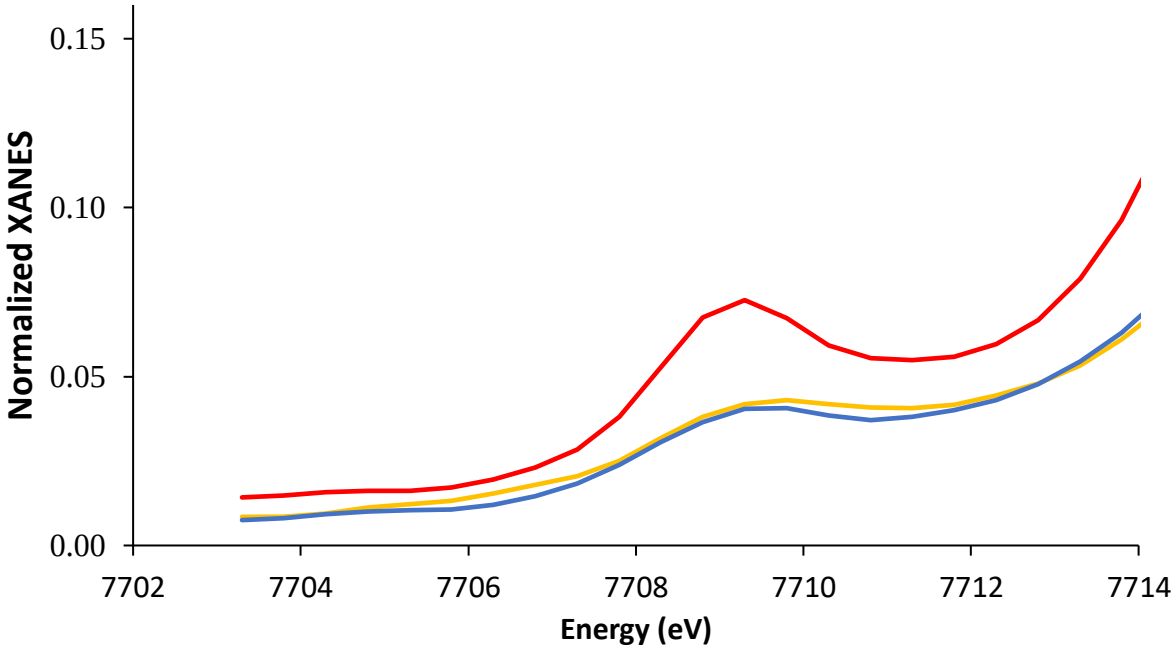

Figure D-4. Pre-edge region of the normalized XANES of 0.15Co: as prepared (yellow), annealed (blue) and calcined (red)

- EXAFS k^3 weighted $\chi(k)$ and Fourier transformed $\chi(r)$

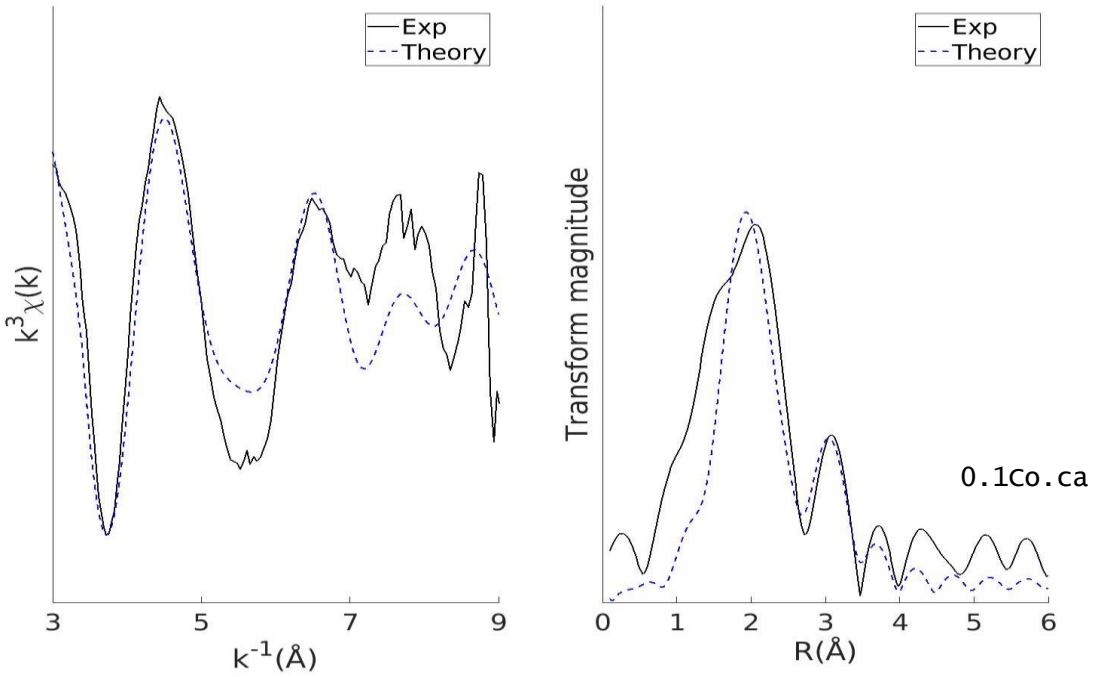

Figure D-5. EXAFS least-square refinements of the first shell and second for 0.1Co calcined sample in k^3-weighting k-space and R-space

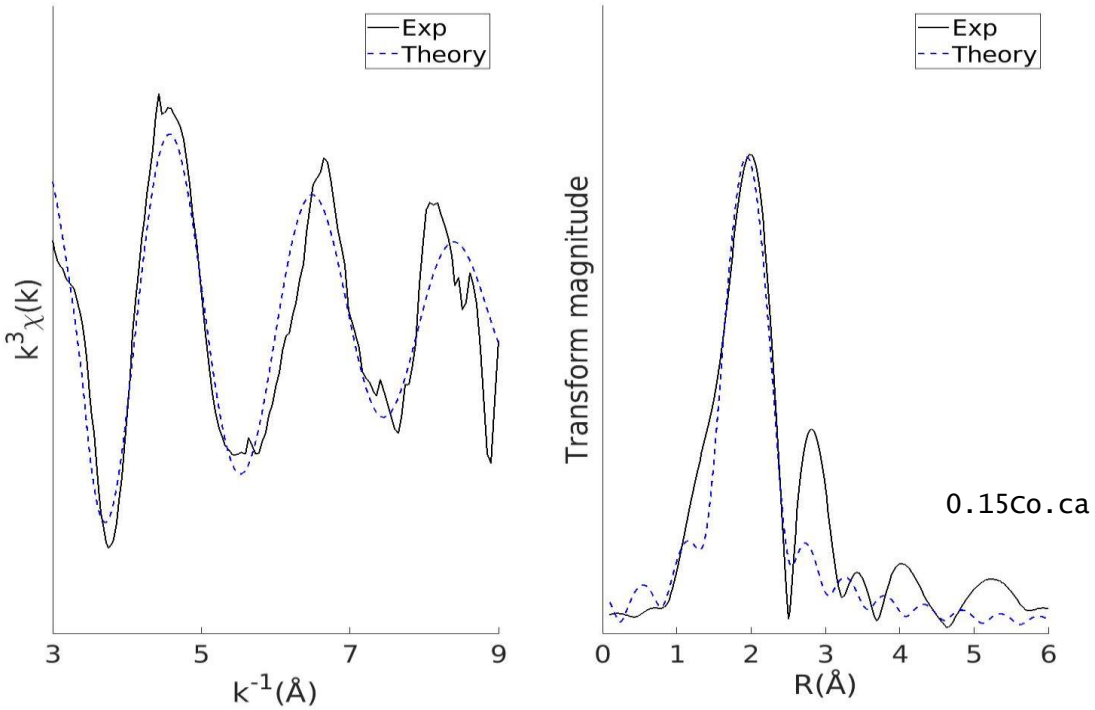

Figure D-6. EXAFS least-square refinements of the first shell for 0.15Co calcined sample in k^3-weighting k-space and R-space.

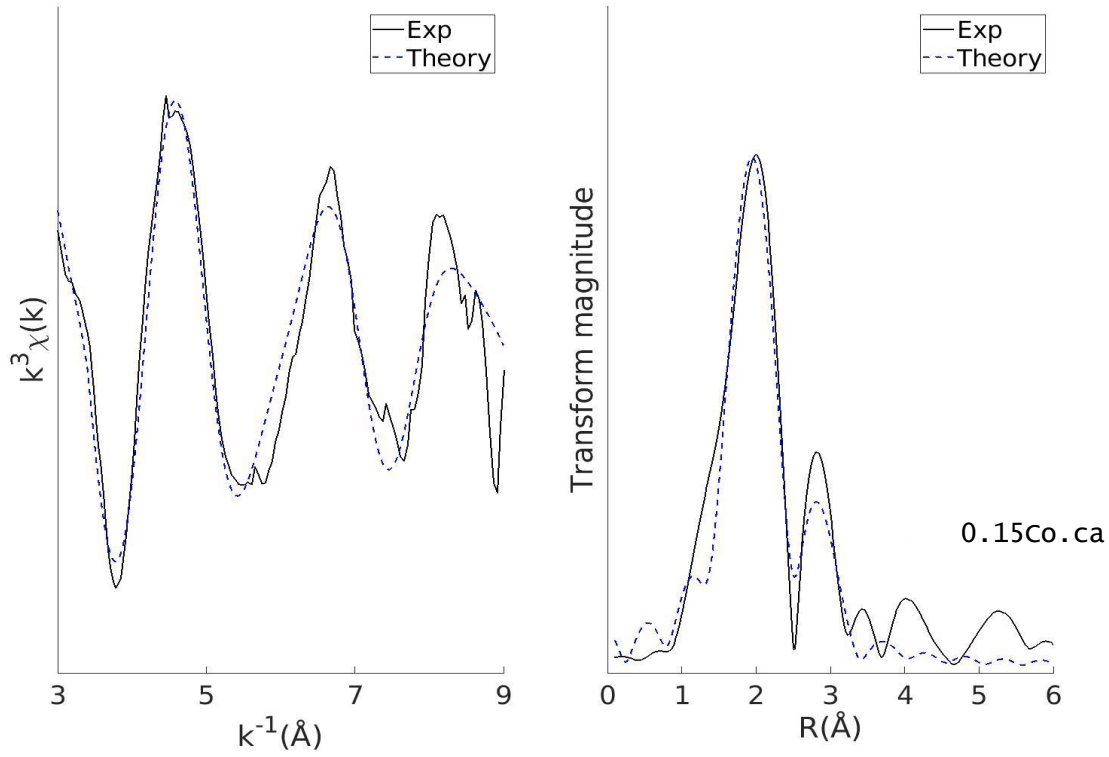

Figure D-7. EXAFS least-square refinements of the first and second shell for 0.1Co calcined sample in k^3-weighting k-space and R-space.

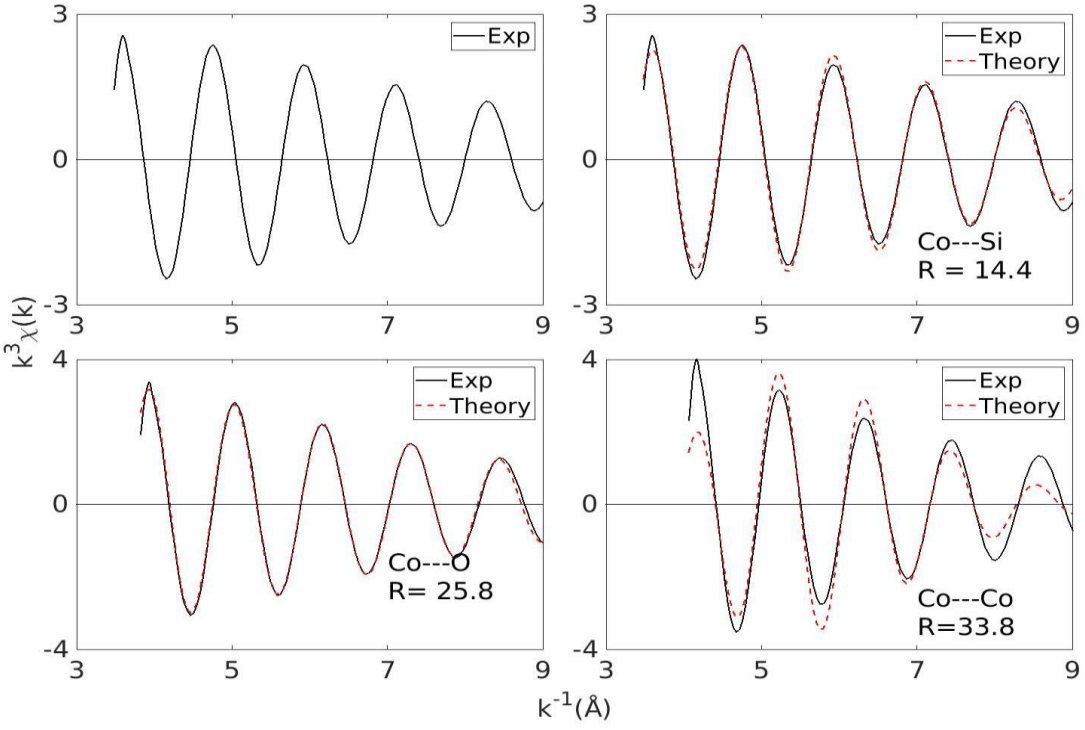

Figure D-8. Fourie filtered to isolate the second shell of calcined 0.15Co sample. R is the goodness of fit.